Study of the electrochemical reaction and bubble dynamics in proton exchange membrane electrolyzer cells

A Dissertation Presented for the

Doctor of Philosophy

Degree

The University of Tennessee, Knoxville

Yifan Li

December 2019

ACKNOWLEDGEMENTS

I would like to express my deepest gratitude to my advisor, Dr. Feng-Yuan Zhang, for taking the time to mentor and he help me. He is my "once in a lifetime" teacher that will stay with me forever, who believed me can overcome the difficulties during my hardest time. I would like to express my sincere gratitude to Dr. Matthew M. Mench, Dr. Reza Abedi, and Dr. Lloyd M. Davis for serving on my dissertation committee. Thanks for the time, talent, insight and expertise they have given to my research.

I would like to thank the members of NanoHELP, Dr. Jingke Mo, Dr. Zhenye Kang, Dr. Gaoqiang Yang, Dr. Kui Li, Dr. Zhiqiang Xie, Shule Yu, Derrick A Talley, Yeshi Dohrmann for their help, support, and friendship, it has been my privilege to work with this group. I would like thank the help from Douglas Warnberg, Alexander Terekhov, Kathleen Lansford, Dr. Lee Leonard, they taught me to learn many new skills and helped me to design and manufacture a lot of research equipment, and to my friends, Hang Wang, and Zefeng Lyu for all the fun we have had.

I thank Dr. G Kane Jennings, and Dr. Xuanli Deng from Vanderbilt University for their advice and help.

I also greatly appreciate the support from U.S. Department of Energy's National Energy Technology Laboratory under Award DE-FE0011585, and National Renewable Energy Laboratory under Award DE-AC36-08GO28308.

Finally, I would like to express my sincere gratitude to my parents for their love and support. Without them, this day would not have been.

ABSTRACT

Hydrogen is a key zero-emission energy storage medium in energy industry of the world. The electrolysis of water with proton exchange membrane electrolyzer cells (PEMECs) has been considered as a promising technology for producing hydrogen and oxygen. The understanding of the electrochemical reactions and two-phase flow phenomena occur in PEMECs is a very important part in promoting energy efficiency of both engineering and sciences. Effective two-phase flow transport is key factor for PEMECs to achieve high performance, since the accumulation of bubble blocks the active areas, and leads to mass transport losses. The objective of the research is to investigate the oxygen evolution reaction (OER), hydrogen evolution reaction (HER), and temperature distribution variance, in order to better understand the mechanism of electrochemical reactions and bubble dynamics, and how their impact on the cell performance. The main task of this thesis includes: (a) *in-situ* visualize and investigate the OER for better understanding the bubble growth process; (b) *in-situ* and *ex*-situ investigate the impact of wettability on the bubble dynamics and cell performance in a PEMEC with Ti thin film LGDL; (c) *in-situ* visualize and investigate the OER and HER in PEMECs for better understanding the bubble detachment process. (d) *in-situ* visualize and investigate the temperature variance and hydrogen bubble dynamics for better understanding the mechanism of HER; (e) *in-situ* visualize and investigate the bubble dynamics and two-phase flow in PEMECs with Ti felt LGDL.

TABLE OF CONTENTS

LIST OF FIGURES

CHAPTER I

INTRODUCTION

1.1 Overview

Today, greenhouse gases driven by the human activities are the most significant factor that impact the global environment. In recent years, more than a half of the US global warming emissions were caused by burning of fossil fuels. In contrast, clean renewable energy sources produce no global warming emissions, development of clean renewable energy resources is necessary for the world.

Today, greenhouse gases driven by the human activities are the most significant factor that impact the global environment. In recent years, more than a half of the US global warming emissions were caused by burning of fossil fuels. In contrast, clean renewable energy sources produce no global warming emissions, development of clean renewable energy resources is necessary for the world.

Hydrogen is a clean energy carrier has attracted a worldwide attention. World consumption of both captive and merchant hydrogen were increased rapidly in the past few decades. About 10 million metric tons of hydrogen are produced in the US every year, and this number is expected to continue increasing. This increase can be attributed to the increase of car ownership rate and the development of energy industry. However, most hydrogen used today is produced from fossil fuels, such as oil or natural gas. Fossil fuel create air pollution and has a negative effect on the sustainable society.

Among the various methods for producing hydrogen and oxygen, the proton exchange membrane electrolyzer cells (PEMECs) is one of the most convenient method without pollution, and has attracted an ever-increasing attention among researchers. The main advantages of PEMECs are as follows:

- The produced hydrogen gas has a very high purity (99.995%).
- The PEMECs can operate at a very high current density (>2 A/cm^2) and pressure (up to 35000 kPa).
- The PEMECs have a fast response, and have a good durability (usually longer than 1000 hours).

Typically, the transparent PEMECs consist of two end plates, catalyst coated membrane (CCM), bipolar plate (BP), two liquid/gas diffusion layers (LGDLs), two gaskets, transparent plate and two current distributors, as illustrated in Figure 1. Nafion membrane coated with catalyst layer is generally used as the CCM. The anode LGDL is usually Ti felt, Ti foam, or Ti thin film, and thecathode LGDL is typically carbon paper. DI water is introduced into the flow channels. In the anode, the water is split into oxygen, protons and electrons, and the protons combine with the electrons to form hydrogen at the cathode, as described as follows:

Anode reaction:

$$2H_2O \xrightarrow{Catalyst} 4H^+ + O_2 + 4e^- \quad (1)$$

Cathode reaction:

$$4H^+ + 4e^- \xrightarrow{Catalyst} 2H_2 \quad (2)$$

In the PEMECs, bubbles are generated and detached from the active areas to the flow channels. The bubbles must be effectively generated and removed from the active areas, an ineffective bubble generation and removal could hinder the transport of reactant from the flow channel to the active areas. In addition, the long stay of bubbles could cause a degradation on the catalyst layer and the LGDL. The performance and the durability of the PEMECs will also be degraded. Thus, studying bubble formation, growth, and detachment during water electrolysis is crucial for optimizing the PEMECs.

1.2 Background and literature review

In this chapter, the general requirements for the electrochemical reaction are described, the methodology and tools used in this project are provided. An introduction of the background and previous research on electrochemical reaction and two-phase flow in porous transport layer are provided. In addition, previous research on bubble evolution in PEMECs are summarized. Finally, a variety of imaging techniques on fuel cell and electrolyzer visualization are introduced.

1.2.1 Electrochemical reaction in PEMECs

During the operation of PEMECs, water circulated on the anode side, and when the water comes to the interface between the LGDL and the catalyst layer, it will be split into protons, oxygen and electrons. Oxygen transport out of the PEMEC with the incoming water flow.

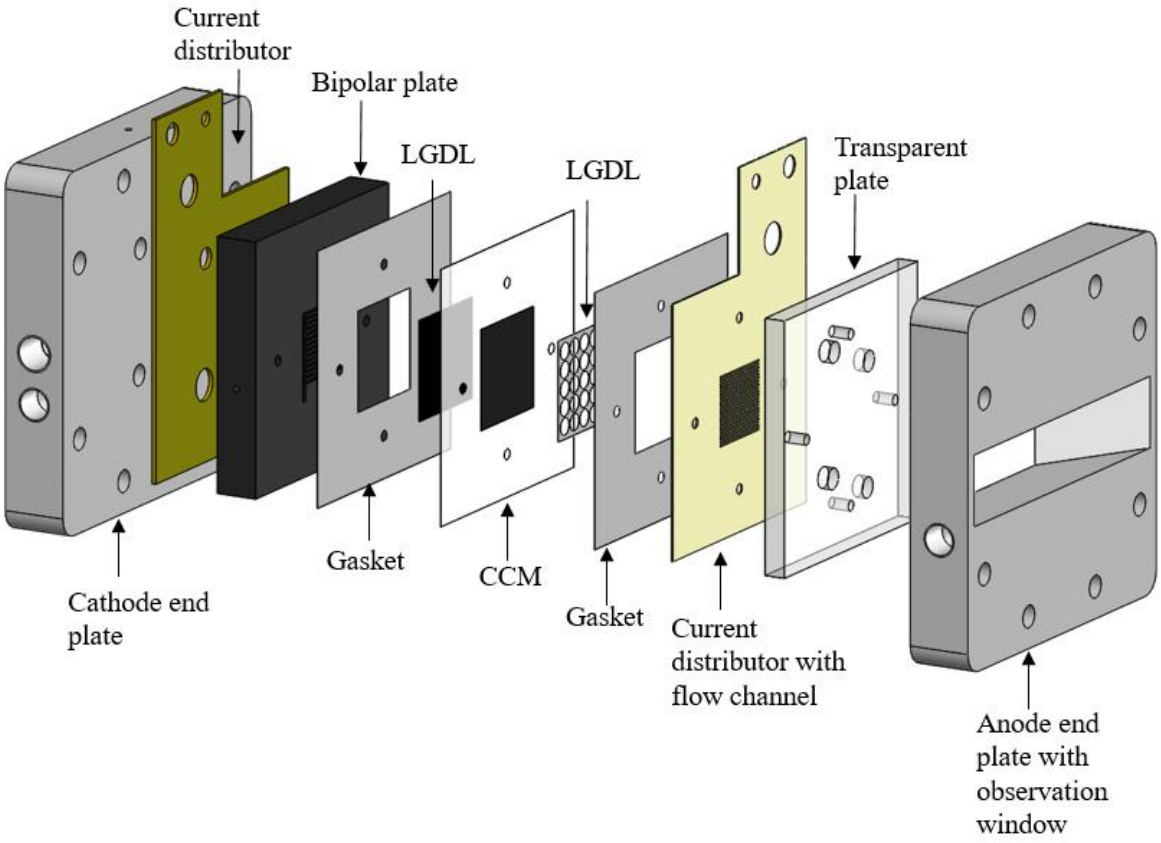

Figure 1. Schematic of a transparent PEMEC.

Protons transport from the anode side to the cathode side through the membrane in the middle. At the cathode side, protons combine with the electrons to form hydrogen. The electrochemical reactions occurred in the PEMECs are ultrafast and in micro scale [1]. Also, the electrochemical reaction occurs in the middle of the PEMECs, a place covered by the current distributor, transparent plate and end plate. It is impossible to use microscope to do the visualization research. Thus, more related studies on hydrogen and oxygen evolution reaction by using more advanced visualization system is necessary for enhancing the PEMECs performance, and increase the amount of products (oxygen and hydrogen) at low cost [2].

1.2.2 Triple-phase boundary

In PEMECs, "triple-phase boundary" is a very important concept during the water electrolysis, because the electrochemical reaction can only occurs at this place [3, 4]. It is a place with electron conductors, catalysts, proton carriers, and pathways for reactants/products. However, the triple-phase boundary has some requirements: it requires an easy pathway for reactant and products; it requires to transfer the electrons; and it requires catalyst to occur the reactions. For a traditional PEMEC, the reaction sites are in the middle of the PEMECs and are covered by the other plates with complicated structure, and it is impossible to capture and investigate the electrochemical reaction with traditional PEMECs. A transparent PEMECs can provide an observation window to directly visualize

the electrochemical reaction in the middle, and challenges the previous assumption that the electrochemical reaction are occurred on the whole catalyst layer surface.

1.2.3 Characteristics of two-phase Flow in PEMECs

There are generally 3 different kinds of two-phase flow phenomena commonly occurred in the flow channels of a PEMEC, namely, bubbly flow, slug flow, and annular flow. At the large flow rate and low operating current density, gas bubbles are in small size and bubble merge behavior are not common, only bubbly flow can be observed at this condition. When the flow velocity gradually decreased and the current density increased, the bubble generation and merge behavior become more common, large bubbly flow and slug flow can be observed at this condition [5, 6].

When the flow velocity becomes minimum and the operating current density becomes very large, the bubble generation sites also greatly increased, the channels are full of large slug and even annular flow. The flow channels are blocked by the annular flow and may cause an impact to the operating performance.

1.2.4 Contact angle

The contact angle is the angle used to measure through the liquid to display the wettability of the contact surface between the gas and the liquid. As shown in the Fig.2, the first bubble on the left shows a small contact angle ($\theta < 90°$).

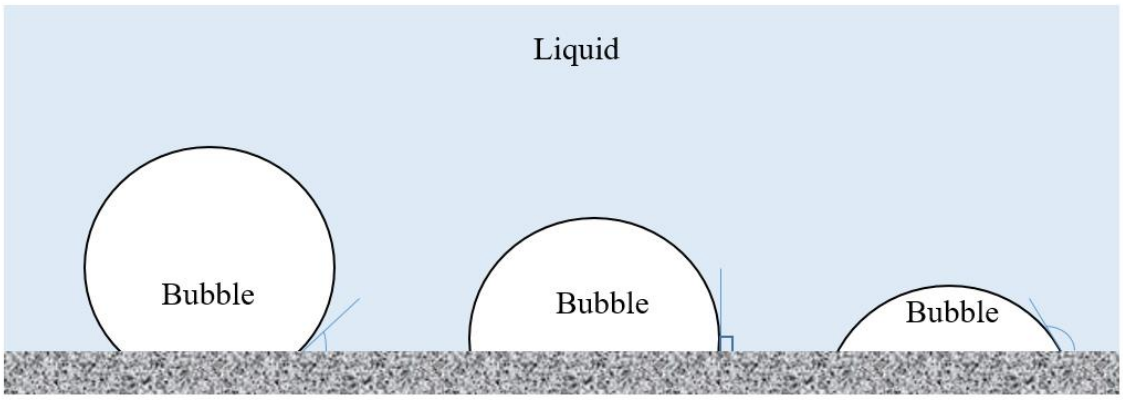

Figure 2. Schematic of contact angles formed by bubble.

More specifically, a contact angle smaller than 90° indicates that the surface is a hydrophilic, which tends to attract water. On the other hand, the bubble on the right, shows a large contact angle contact angle ($\theta > 90°$). A contact angle larger than 90° indicates that the surface is a hydrophobic surface, tends to repel the water. A hydrophilic surface is preferred for enhancing the cell performance, because it can accelerate the bubble detachment speed [7, 8].

1.2.5 Visualization of bubble dynamics in fuel cell and electrolyzer

A lot of researches have been done to thoroughly investigate the bubble dynamics and two-phase flow phenomena in different systems, including boiling system, simulator, fuel cell, and electrolyzer cell, to better understanding the bubble behavior in the systems. Selamet et al. visualized and investigated the bubble dynamics and two-phase flow phenomena in

PEMECs [9, 10]. They investigated the impact of different operating conditions (flow rate, temperature) on the oxygen bubble. They found that the oxygen bubbles are more easily removed with an increase of the flow rate. They also found that the cell performance could get greatly influenced with an increase of temperature. Mo et al. discovered the inside fluid phenomena by using a high-speed visualization system together with a specifically designed transparent PEMEC that allowed them to gather almost all the information they needed in the micro-channels. They observed a very interesting phenomenon that the bubble only generated at the rim of the pores, and that almost no bubble generated in the center [11-13]. Chandran et al. observed constant increases in the size of hydrogen bubbles when they were generated at different locations. Bubble sizes varied from 40 to 100 μm at the surface of an electrode. When the bubble was generated at a position of 2 mm away from electrode, it would change from 100 to 130 μm. Bubble growth velocity also varied from 0.3 cm/s to 0.76 cm/s [14]. Yang et al. used a microscope and a high-speed camera to track the lifetime and size of single hydrogen bubbles on a platinum microelectrode. It is found that the bubble increased from 50 to 250 μm within 1 second [15]. Panchenko et al. used neutron radiography technique to visualize the two-phase flow phenomena in a PEMEC. They found the mass transport loss may increase due to an insufficient moistening of the membrane. Especially at high current density, the large amount of gas may form a gas barrier, which prevent the water supply of the catalyst layer [16]. Lafmejani et al. studied the gas-liquid flow in a PEMEC by using the computational fluid dynamics simulation method and in-situ experimental research, which employed 4 mm width channel,

0.968 m/s inlet liquid velocity and 6.38×10^{-4} m/s inlet gas velocity. Both the experimental and simulation results showed that there were some small bubbles between the long taylor bubbles, and it was also found that the shape of the micro-channel could affect the behavior of taylor bubbles [17]. Dedigama et al. measured and visualized the two-phase flow phenomena relating to the operation potential of a transparent single channel PEMEC (3 mm × 85 mm) with different water flow rates (1, 3, 5 ml/min). They found bubble diameter was changed from 0.87 mm at low potential with a flow rate of 5 ml/min to 2.93 mm at high potential with a flow rate of 1 ml/min , which meant the oxygen bubble size could increase with increasing in potential and decrease with increasing in water flow rate [18]. Zhang et al. took advantage of micro visualization system and designed transparent PEM fuel cells. They successfully *in-situ* revealed the micro drop dynamics on the GDL surface and two-phase flow in micro channels [19, 20]. For further *in-situ* investigation of the dynamics of microdroplets and electrochemical reactions on the CL surface, including micro drop formation, growth, coalescence, and removal, Zhang et al. developed metallic gas diffusion layer with straight pores and catalyst-visible operational fuel cells. They showed reducing the GDL pore size and increasing catalyst layer hydrophobic property would retain liquid water in the gas phase [21-23]. Liao used a transparent direct methanol fuel cell to visualize the flow of CO_2 gas bubbles in the anode channels, and found that increasing flow rate from 2 ml/min to 10 ml/min could accelerate the removal of the discrete CO_2 gas bubbles and improve the cell performance [24]. Ito et al. investigated the impact of porosity and pore diameter of LGDL on the PEMEC performance. They found

that the performance can greatly increase with a decrease of pore size. Large bubbles are more easily form in a large pore with large pore size, and may block the pathway of reactants, finally leading to a decrease of cell performance. Finally, they found a uniform contact pressure between the LGDL and the catalyst layer could reduce the contact resistance and activation overpotential [25].

There are also a lot of researchers focused on the investigation of the wettability impact on the electrochemical reaction and operating performance. Kumbur et al. and LaManna et al. investigated multiphase capillary transport through the thin diffusion media, microporous layer, catalyst layer and their interfaces, and proposed a new correlations between capillary pressure–liquid saturation. They also found that any hydrophobicity increase in the DM led to higher capillary pressures and less flooding [26-28]. LaManna et al. further studied interfacial effects for DM|MPL and MPL|CL the diffusion thoroughly Cubaud et al. investigated different types of liquid/gas flow patterns in square microchannels and observed five primary types of flow regimes in hydrophilic channels: bubbly, wedging, slug, annular, and dry flow. Three different flow regimes were also seen in hydrophobic channels: isolated asymmetric bubble flow, wavy bubble flow, and scattered droplet flow [29]. Li et al. investigated the impact of wettability on the bubble dynamics and cell performance. They found the bubbles in PEMECs with hydrophilic LGDL are more easily to detach, and the large bubbly and slug flow are much smaller than that with hydrophobic LGDL [30]. Sakuma et al. observed single and multiple oxygen low-speed bubbles evolution phenomena, with the bubble diameter increasing from about 0.02 mm to 0.6 mm

within 4.6 s. They found the surface wettability played a major role in bubble growth behaviors. Nucleation sites decreased and bubble sizes became large with increasing surface hydrophobicity. Bubbles were also difficult to detach from hydrophobic electrode. The result was discovered by using the current interrupter method, which could measure the ohmic resistance corresponding to the surface coverage [31].

Finally, there are many researchers studied the electrochemical reaction by using mathematic model. Han et al. built a two-phase transport model for PEMECs. This model can provide a detailed understanding of the impact of contact angle, porosity, and membrane thickness on the polarization curve and cell performance. A comprehensive investigation of the ohmic loss, activation loss, and mass transport loss change with different membrane thickness has been provided [32]. By simulating liquid water dynamics and two-phase transport in fuel cells, Meng et al. performed the theoretical studies and investigated interfacial liquid saturation between the flow channel and the GDL on the PEMFC performance [33, 34]. Wang et al. developed a three-dimensional two-phase model to electrochemical processes and multiphase flows in fuel cells. They found that multiphase flows emerged near the channel outlet with co-flow configuration[35, 36]. Jouhara et al. developed a 3-dimensional CFD model to simulate the two-phase flow dynamics in a pipe and was found able to reproduce the multiphase flow phenomena for different kinds of working fluids (water and R134a) [37].

1.3 Motivation and objectives

The electrochemical reactions occurred in the PEMECs are expressed by the bubble evolution. A better understanding of the bubble dynamics and two-phase flow phenomena helps to better optimize the hydrogen and oxygen production and enhance the cell performance. The primary motivation for this thesis is to understand the effect of different operating factors (specifically, temperature, current density, flow rate, and surface wettability) on the bubble dynamics in the PEMECs. The cost reduction of the PEMECs can be achieved by understanding the bubble behaviors at different working conditions and improving the performance.

The main objective of this research is to develop experimental and mathematical method to visualize and investigate the bubble dynamics and two-phase flow phenomena in PEMECs in order to characterize the impact of properties (different temperatures, current densities, flow rates, wettability) on the bubble evolution process, to have a better understanding of the true electrochemical reaction inside the PEMECs, and finally find the best working conditions to improve the efficiency. To accomplish this goal, both hydrogen and oxygen bubble behavior were visualized using transparent PEMECs and high-speed and microscale visualization system. Moreover, a mathematic model for the bubble evolution was developed and is in a good agreement with the experimental data. Chapter 2 applied both experimental and modeling methods in order to gain insight on the impact of different operating conditions on the bubble growth in PEMECs. In chapter 3, an experimental study was done to investigate the impact of LGDL wettability on the

performance and bubble dynamics of PEMECs. In chapter 4, a correlation between the electrochemical reaction on the cathode and the temperature distribution change has been built for a better understanding the hydrogen evolution reaction. In chapter 5, both hydrogen and oxygen bubble growth and detachment process were in-situ visualized, a mathematic model for bubble detachment diameter at different working conditions was built and validated using the experimental results. The modeling results can be applied in different working conditions and different applications. In chapter 6, bubble dynamics and two-phase flow phenomena in PEMECs with Ti felt LGDL has been visualized and investigated at different working conditions.

References

1. Kang, Z., et al., *Performance improvement of proton exchange membrane electrolyzer cells by introducing in-plane transport enhancement layers.* Electrochimica Acta, 2019. **316**: p. 43-51.
2. Li, Y., et al., *Direct thermal visualization of micro-scale hydrogen evolution reactions in proton exchange membrane electrolyzer cells.* Energy Conversion and Management, 2019. **199**: p. 111935.
3. Fogel, S., H. Kryk, and U. Hampel, *Simulation of the transient behavior of tubular solid oxide electrolyzer cells under fast load variations.* International Journal of Hydrogen Energy, 2019. **44**(18): p. 9188-9202.
4. Park, T., et al., *Effect of nano-pinholes within ceramic electrolytes of thin-film solid oxide fuel cells.* Journal of Industrial and Engineering Chemistry, 2019. **75**: p. 108-114.
5. Maier, M., et al., *Operando flow regime diagnosis using acoustic emission in a polymer electrolyte membrane water electrolyser.* Journal of Power Sources, 2019. **424**: p. 138-149.
6. Olesen, A.C., S.H. Frensch, and S.K. Kær, *Towards uniformly distributed heat, mass and charge: A flow field design study for high pressure and high current density operation of PEM electrolysis cells.* Electrochimica Acta, 2019. **293**: p. 476-495.

7. Garcia-Navarro, J., M. Schulze, and K. Friedrich, *Detecting and modeling oxygen bubble evolution and detachment in proton exchange membrane water electrolyzers.* International Journal of Hydrogen Energy, 2019.

8. Leonard, M.E., L. Clarke, and F.R. Brushett. *Wettability of Gas Diffusion Electrode Materials for CO2 Reduction*. in *Meeting Abstracts*. 2019. The Electrochemical Society.

9. Selamet, O.F., et al., *In Situ Two-Phase Flow Investigation of Proton Exchange Membrane (PEM) Electrolyzer by Simultaneous Optical and Neutron Imaging.* ECS Transactions, 2011. **41**(1): p. 349-362.

10. Selamet, O., et al., *Two-phase flow in a proton exchange membrane electrolyzer visualized in situ by simultaneous neutron radiography and optical imaging.* international journal of hydrogen energy, 2013. **38**(14): p. 5823-5835.

11. Mo, J.K., et al., *Discovery of true electrochemical reactions for ultrahigh catalyst mass activity in water splitting.* Science Advances, 2016. **2**(11).

12. Kang, Z., et al., *Novel thin/tunable gas diffusion electrodes with ultra-low catalyst loading for hydrogen evolution reactions in proton exchange membrane electrolyzer cells.* Nano energy, 2018. **47**: p. 434-441.

13. Mo, J., et al., *In situ investigation on ultrafast oxygen evolution reactions of water splitting in proton exchange membrane electrolyzer cells.* Journal of Materials Chemistry A, 2017. **5**(35): p. 18469-18475.

14. Chandran, P., S. Bakshi, and D. Chatterjee, *Study on the characteristics of hydrogen bubble formation and its transport during electrolysis of water.* Chemical Engineering Science, 2015. **138**: p. 99-109.

15. Yang, X.G., et al., *Dynamics of Single Hydrogen Bubbles at a Platinum Microelectrode.* Langmuir, 2015. **31**(29): p. 8184-8193.

16. Panchenko, O., et al., *In-situ two-phase flow investigation of different porous transport layer for a polymer electrolyte membrane (PEM) electrolyzer with neutron spectroscopy.* Journal of Power Sources, 2018. **390**: p. 108-115.

17. Lafmejani, S.S., A.C. Olesen, and S.K. Kær, *VOF modelling of gas–liquid flow in PEM water electrolysis cell micro-channels.* International Journal of Hydrogen Energy, 2017.

18. Dedigama, I., et al., *Current density mapping and optical flow visualisation of a polymer electrolyte membrane water electrolyser.* Journal of Power Sources, 2014. **265**: p. 97-103.

19. Zhang, F.Y., X.G. Yang, and C.Y. Wang, *Liquid water removal from a polymer electrolyte fuel cell.* Journal of the Electrochemical Society, 2006. **153**(2): p. A225-A232.

20. Yang, X.G., et al., *Visualization of liquid water transport in a PEFC.* Electrochemical and Solid State Letters, 2004. **7**(11): p. A408-A411.

21. Zhang, F.Y., S.G. Advani, and A.K. Prasad, *Performance of a metallic gas diffusion layer for PEM fuel cells.* Journal of Power Sources, 2008. **176**(1): p. 293-298.

22. Zhang, F.Y., A.K. Prasad, and S. Advani, *Nano-based gas diffusion media*. 2010, US7785748

23. Zhang, F.-Y., S.G. Advani, and A.K. Prasad, *Performance of a metallic gas diffusion layer for PEM fuel cells.* Journal of power sources, 2008. **176**(1): p. 293-298.

24. Liao, Q., et al., *Visualization study on the dynamics of CO 2 bubbles in anode channels and performance of a DMFC.* Journal of Power Sources, 2007. **171**(2): p. 644-651.

25. Ito, H., et al., *Experimental study on porous current collectors of PEM electrolyzers.* International journal of hydrogen energy, 2012. **37**(9): p. 7418-7428.

26. Kumbur, E., K. Sharp, and M. Mench, *A design tool for predicting the capillary transport characteristics of fuel cell diffusion media using an artificial neural network.* Journal of Power Sources, 2008. **176**(1): p. 191-199.

27. Kumbur, E., K. Sharp, and M. Mench, *On the effectiveness of Leverett approach for describing the water transport in fuel cell diffusion media.* Journal of Power Sources, 2007. **168**(2): p. 356-368.

28. LaManna, J.M., et al., *Measurement of capillary pressure in fuel cell diffusion media, micro-porous layers, catalyst layers, and interfaces.* Journal of Power Sources, 2014. **271**: p. 180-186.

29. Cubaud, T., U. Ulmanella, and C.-M. Ho, *Two-phase flow in microchannels with surface modifications.* Fluid Dynamics Research, 2006. **38**(11): p. 772-786.

30. Li, Y., et al., *Wettability effects of thin titanium liquid/gas diffusion layers in proton exchange membrane electrolyzer cells.* Electrochimica Acta, 2019. **298**: p. 704-708.

31. Sakuma, G., Y. Fukunaka, and H. Matsushima, *Nucleation and growth of electrolytic gas bubbles under microgravity.* International Journal of Hydrogen Energy, 2014. **39**(15): p. 7638-7645.

32. Han, B., et al., *Electrochemical performance modeling of a proton exchange membrane electrolyzer cell for hydrogen energy.* International Journal of Hydrogen Energy, 2015. **40**(22): p. 7006-7016.

33. Meng, H. and C.-Y. Wang, *Model of two-phase flow and flooding dynamics in polymer electrolyte fuel cells.* Journal of the Electrochemical Society, 2005. **152**(9): p. A1733-A1741.

34. Meng, H., *Numerical studies of liquid water behaviors in PEM fuel cell cathode considering transport across different porous layers.* international journal of hydrogen energy, 2010. **35**(11): p. 5569-5579.

35. Wang, Y., *Modeling of two-phase transport in the diffusion media of polymer electrolyte fuel cells.* Journal of Power Sources, 2008. **185**(1): p. 261-271.

36. Wang, Y., et al., *Stochastic modeling and direct simulation of the diffusion media for polymer electrolyte fuel cells.* International journal of heat and mass transfer, 2010. **53**(5-6): p. 1128-1138.

37. Jouhara, H., B. Fadhl, and L.C. Wrobel, *Three-dimensional CFD simulation of geyser boiling in a two-phase closed thermosyphon.* International Journal of Hydrogen Energy, 2016. **41**(37): p. 16463-16476.

CHAPTER II

IN-SITU INVESTIGATION OF BUBBLE DYNAMICS AND TWO-PHASE FLOW IN PROTON EXCHANGE MEMBRANE ELECTROLYZER CELLS

A version of this chapter was originally published by Yifan Li:

Yifan Li, Zhenye Kang, Jingke Mo, Gaoqiang Yang, Shule Yu, Derrick A. Talley, Bo Han, and Feng-Yuan Zhang. " *In-situ* investigation of bubble dynamics and two-phase flow in proton exchange membrane electrolyzer cells." *International Journal of Hydrogen Energy* 43, no. 24 (2018): 11223-11233.

I am fully responsible for the work submitted in these publications.

2.1 Abstract

Gas bubble dynamics and two-phase flow have a significant impact on the performance and efficiency of proton exchange membrane electrolyzer cells (PEMECs). It has been strongly desired to develop an effective experimental method for *in-situ* observing the high-speed/micro-scale oxygen bubble dynamics and two-phase flow in an operating PEMEC. In this study, the micro oxygen bubble dynamic behavior and two-phase flow are *in-situ* visualized through a high-speed camera coupled with a specific designed transparent PEMEC, which uses a novel thin liquid/gas diffusion layer (LGDL) with straight-through pores. The effects of different operating conditions on oxygen bubble dynamics, including nucleation, growth, and detachment, and two-phase flow have been comprehensively investigated. The results show that temperature and current density have great effects on bubble growth rate and reaction sites while the influence of flow rate is very limited. The number, growth rate, nucleation site, and slug flow regime of oxygen gas bubbles increase as temperature and/or current density increases, which indicates that an

increase in temperature and/or current density can enhance the oxygen production efficiency. Further, a mathematical model for the bubble growth is developed to evaluate the effects of temperature and current density on the bubble dynamics. A mathematical model has been established and shows a good correlation with the experimental results. The studies on two-phase flow and high-speed micro bubble dynamics in the microchannel will help to discover the true electrochemical reaction at micro-scale in an operating PEMEC.

2.2 Highlights

- Rapid micro oxygen bubble generation and growth are *in-situ* visualized.
- Bubble growth rate and reaction sites are increased with the current density.
- A model shows a good agreement with the experiment results.
- Annular flow is more easily to form under high current densities.

2.3 Introduction

With the growing development of various energy production and use industries, such as aerospace, public transportation and domestic use, the traditional energy production and storage methods can no longer meet the public demands because of its global-warming potential, low energy density, risk of explosion, continuous growing price, and carbon monoxide inhalation [1, 2]. With this background, water electrolysis, for example, uses

electricity to split water into its constituent oxygen and hydrogen atoms, offering the most promising method currently known for oxygen and hydrogen production [3]. Electrolysis can take place quickly at different scales ranging from micro to macro. The advanced proton exchange membrane electrolyzer cells (PEMECs) used for this purpose are widely considered to offer an efficient way of producing oxygen and hydrogen from renewable energy. What's more, PEMECs offer a range of benefits, including heightened effectiveness, quick response times, higher levels of gas purity, and ease of handling [4-9]. However, they present certain challenges of cost, durability, and efficiency [10-13].

In an operating PEMEC, the oxygen evolution reaction (OER) occurs at anode side and must meet the triple-phase boundary requirements involving electrons, catalysts (IrRuOx), proton carriers, and pathways for water and oxygen. Water is circulated during the operation at the anode side of the PEMECs to the interface between the catalyst layer and the liquid/gas diffusion layer (LGDL) where it reacts with the catalyst to be split into oxygen, protons, and electrons. The oxygen is carried with the incoming water flow to the outlet at the anode. The protons are transferred from the anode side to the cathode side through the membrane in the middle of the cell and then react with the electrons from outside to form hydrogen gas.

The electrochemical reactions at the anode and cathode of a PEMEC can be given as Equations (1) and (2).

$$\text{Anode: } 2\text{H}_2\text{O} \xrightarrow{Catalyst} 4\text{H}^+ + O_2 + 4e^- \quad (1)$$

$$\text{Cathode: } 4\text{H}^+ + 4\text{e}^- \xrightarrow{\text{Catalyst}} 2\text{H}_2 \quad (2)$$

Some experimental and modeling studies have been already conducted to the bubble and two-phase transport dynamics inside a water electrolyzer under various conditions. Mo et al. discovered the inside fluid phenomena by using a high-speed visualization system together with a specifically designed transparent PEMEC that allowed them to gather almost all the information they needed in the micro-channels. They observed a very interesting phenomenon that the bubble only generated at the rim of the pores, and that almost no bubble generated in the center [14-16]. Sakuma et al. observed single and multiple oxygen low-speed bubbles evolution phenomena, with the bubble diameter increasing from about 0.02 mm to 0.6 mm within 4.6 s. They found the surface wettability played a major role in bubble growth behaviors. Nucleation sites decreased and bubble sizes became large with increasing surface hydrophobicity. Bubbles were also difficult to detach from hydrophobic electrode. The result was discovered by using the current interrupter method, which could measure the ohmic resistance corresponding to the surface coverage [17]. Lafmejani et al. studied the gas-liquid flow in a PEMEC by using the computational fluid dynamics simulation method and in-situ experimental research, which employed 4 mm width channel, 0.968 m/s inlet liquid velocity and 6.38×10^{-4} m/s inlet gas velocity. Both the experimental and simulation results showed that there were some small bubbles between the long taylor bubbles, and it was also found that the shape of the micro-channel could affect the behavior of taylor bubbles [18]. Ito et al. investigated the influence of water flow in a channel on the gas production efficiency of an operating solid polymer water electrolyzer and the detachment phenomena of hydrogen gas bubbles in a 1000 μm

width channel. The study found that production efficiency increased with water flow rate and bubbles were more easily to detach at 120 cc/min and 0.3 MPaG [19]. Dedigama et al. measured and visualized the two-phase flow phenomena relating to the operation potential of a transparent single channel PEMEC (3 mm × 85 mm) with different water flow rates (1, 3, 5 ml/min). They found bubble diameter was changed from 0.87 mm at low potential with a flow rate of 5 ml/min to 2.93 mm at high potential with a flow rate of 1 ml/min , which meant the oxygen bubble size could increase with increasing in potential and decrease with increasing in water flow rate [20]. Chandran et al. observed constant increases in the size of hydrogen bubbles when they were generated at different locations. Bubble sizes varied from 40 to 100 μm at the surface of an electrode. When the bubble was generated at a position of 2mm away from electrode, it would change from 100 to 130 μm. Bubble growth velocity also varied from 0.3 cm/s to 0.76 cm/s [21]. Bo et al. established a mathematical model to simulate the two-phase flow behaviors in a PEMEC and did a comprehensively investigation of different factors including contact angle, porosity, and pore size, on the capillary flow and the distribution of liquid water in microchannel. The results showed that an increasing in contact angle will raise the cell voltage and decrease cell performance, the increased LGDL porosity will enhance the cell performance. The other factors like the membrane thickness, current density also have a significant influence on the cell performance [22-25].

Many researchers have studied on the dynamics of bubble evolution and two-phase flow in different systems, including a boiling system, a simulator, a fuel cell, and a water

electrolyzer cell. Yang et al. used a microscope and a high-speed camera to track the lifetime and size of single hydrogen bubbles on a platinum microelectrode. It is found that the bubble increased from 50 to 250 μm within 1 second [26]. Zhang et al. took advantage of micro visualization system and designed transparent PEM fuel cells. They successfully *in-situ* revealed the micro drop dynamics on the GDL surface and two-phase flow in micro channels [27, 28]. For further *in-situ* investigation of the dynamics of microdroplets and electrochemical reactions on the CL surface, including micro drop formation, growth, coalescence, and removal, Zhang et al. developed metallic gas diffusion layer with straight pores and catalyst-visible operational fuel cells. They showed reducing the GDL pore size and increasing catalyst layer hydrophobic property would retain liquid water in the gas phase [29-31]. Kumbur et al. and LaManna et al. investigated multiphase capillary transport through the thin diffusion media, microporous layer, catalyst layer and their interfaces, and proposed a new correlation between capillary pressure–liquid saturation. They also found that any hydrophobicity increase in the DM led to higher capillary pressures and less flooding [32-34]. LaManna et al. further studied interfacial effects for DM|MPL and MPL|CL the diffusion thoroughly Cubaud et al. investigated different types of liquid/gas flow patterns in square microchannels and observed five primary types of flow regimes in hydrophilic channels: bubbly, wedging, slug, annular, and dry flow. Three different flow regimes were also seen in hydrophobic channels: isolated asymmetric bubble flow, wavy bubble flow, and scattered droplet flow [35]. By simulating liquid water dynamics and two-phase transport in fuel cells, Meng et al. performed the theoretical

studies and investigated interfacial liquid saturation between the flow channel and the GDL on the PEMFC performance [36, 37]. Wang et al. developed a three-dimensional two-phase model to electrochemical processes and multiphase flows in fuel cells. They found that multiphase flows emerged near the channel outlet with co-flow configuration[38, 39]. Liao used a transparent direct methanol fuel cell to visualize the flow of CO_2 gas bubbles in the anode channels, and found that increasing flow rate from 2 ml/min to 10 ml/min could accelerate the removal of the discrete CO_2 gas bubbles and improve the cell performance [40]. Jouhara et al. developed a 3-dimensional CFD model to simulate the two-phase flow dynamics in a pipe and was found able to reproduce the multiphase flow phenomena for different kinds of working fluids (water and R134a) [41].

Other investigators [42-49] also analyzed the bubble formation and evolution mechanisms during different conditions and other applications. However, understanding the true two-phase transport inside the PEMEC has been of great challenges. In this study, by using the thin well-tuned LGDL and the microscale high-speed visualization system, the visualization experiments were conducted to observe the two-phase flow phenomena within a microchannel. Oxygen bubbles' generation and growth behavior in microchannels were measured with different temperatures, current densities, and fluid rates. Bubbly flow, slug flow, annular flow, and other typical flow patterns were found to occur in the microchannels during two-phase flow periods. Notably, several factors affect bubble formation in specific pores, including reaction rates and reaction sites as well as temperature, and current density have been discussed for thoroughly understanding of two-

phase flow phenomena. This research is expected to lead to complete understanding of the bubble-producing and evolution mechanisms in the PEMEC, which can provide insights for improving the cell performance and efficiency.

2.4 Experimental details

A schematic of the transparent PEMEC is shown in Figure 3. Some changes are made from a conventional PEMEC to allow visualization of cellular reactions and improve the operation efficiency. The two end plates are made of stainless steel. A rectangle hole measuring 20 mm by 33 mm is created in the end plate at the anode side as an observation window, which is used to observe the two-phase flow phenomena inside the cell. The anode current distributor is divided into two parts: a gold-coated titanium plate of 0.60 mm thick, which is used to improve the electrolysis efficiency, and a transparent plastic plate with flow channels. Also, a 1 cm^2 novel thin-film circular pore-shaped LGDL is developed with a thickness of 25 μm. The specifically designed well-tunable LGDL is the key component of the PEMEC in the present experiment, because it could greatly decrease the ohmic loss and enable a direct capture of electrochemical reactions in an operating PEMEC.

The structure at the cathode side is the same as that of our previous design [50, 51]. The cathode side current distributor is made of copper. The cathode LGDL is Toray 090 carbon paper treated with 5% PTFE.

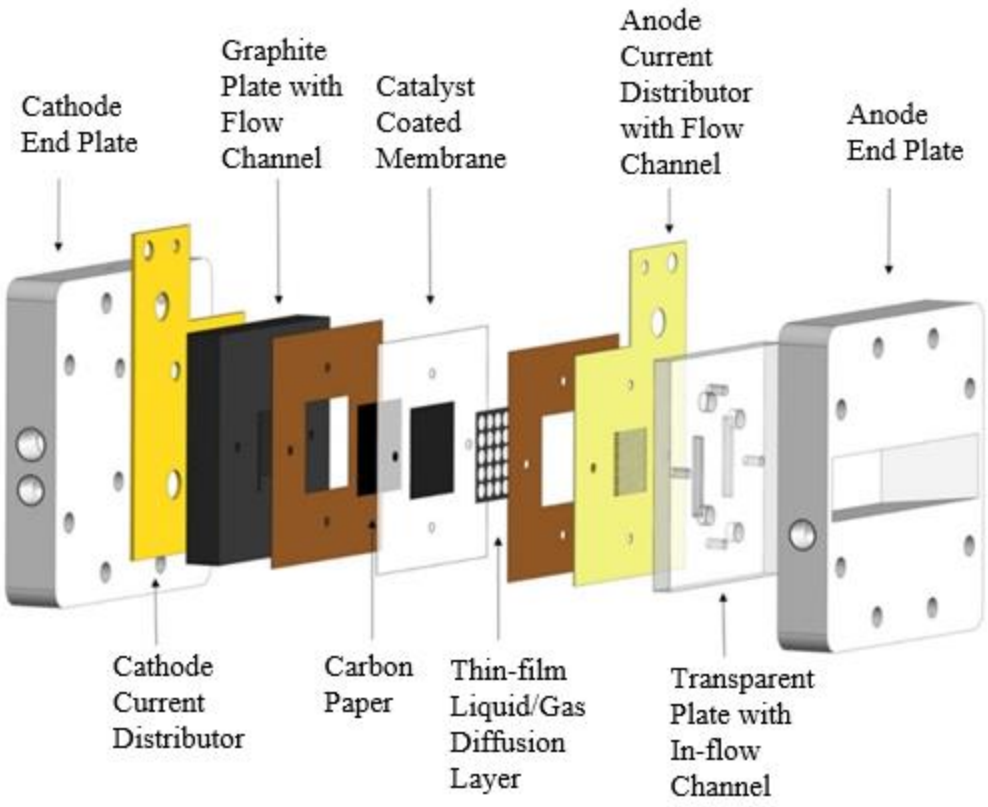

Figure 3. Schematic of the transparent PEMEC

The cell is assembled using eight evenly distributed bolts with 40 in-lb of torque. The specific designed transparent PEMEC is operated at different temperatures and flow rates, with an electrolyzer test station to control and monitor flow rate, current densities, temperature, and voltage.

The potentiostat system controls the PEMEC with an around 100 A current and a 5 V voltage. The framework is linked to an EC-Lab, which is the electrochemical analysis program produced by Bio-Logic. The program has been previously utilized in the assessment of electrochemical impedance spectroscopy (EIS) and cell performance. Deionized water is supplied with a liquid pump system from KNF Neuberger at a constant volumetric flow rate of 40 ml/min. As regards performance assessment, the application of cumulative current density to the PEMEC is applied across a specific time frame. There is also an increase in current density from 0 A/cm^2 to 2.0 A/cm^2 across three varying temperatures. (40 °C, 60 °C, and 80 °C).

By taking advantage of the high-speed visualization system and specifically designed PEMEC, a sequence of close-up images and videos of pore-scale electrochemical reactions can be captured with different current densities, temperatures, and flow rates. Images can be captured at the right side of the micro-channels via a see-through plate and a high-speed visualization system with a frame rate of 7500 fps.

2.5 Bubble Growth Model

Some models and empirical relationships have been proposed to investigate the bubble dynamic behavior [52-56]. The model is based on the following assumptions: (A) The gas in the microchannel is assumed to be ideal gas; (B) The bubble growth is only due to direct diffusion of the oxygen produced by water electrolysis; (C) The bubble growth rate for all the bubbles at different sites are same under a certain working condition. In the present study, a model for growing bubbles has been developed to analyze oxygen bubbles' behavior on the substrate surface. Based on the contact angle and bubble size, the bubble volume before detaching can be calculated as follows [57],

$$V = \frac{1}{3}\pi r^3[2 + 3\,cos\,\theta - (cos\theta)^3] \quad (3)$$

Where r is the radius of bubble, θ is the contact angle and has a value of $45°$ [13].

The ideal gas law allows derivation of equation

$$P_bV = nR_gT \quad (4)$$

Where P_b is the pressure of the bubble, n is mole number and is given by $n = \dot{n}t$, t is the time, R_g is the gas constant of 8.314 J/mol K, and T denotes the operating temperature in the unit of K.

According to the balanced electrochemical reaction equation, the rate of gas generation is given by $\dot{n} = \frac{iA}{nF}$, (5)

Where i is the current density (A/ cm^2), A is the area of LGDL (1.0 cm^2), F is the faraday constant (96485 C/mol).

Combining Equations (3) and (4) gives

$$P_b \frac{1}{3}\pi r^3(2 + 3\,cos\,\theta - (cos\theta)^3) = \dot{n}tR_gT \quad (6)$$

The generation rate for one bubble can be expressed as:

$$n' = \frac{\dot{n}}{N_*} \quad (7)$$

Where N_* is the total number of bubbles for each test case, giving value of 3386 for 0.5 A/cm^2, 4320 for 1.0 A/cm^2 and 6656 for 4.0 A/cm^2, the details to calculate number of bubbles will be introduced later.

Then the bubble radius for one bubble can be produced as,

$$r = [\frac{3kn'^{R_g T}}{\pi P_b(2+3\,cos\,\theta - cos^3\theta)}\,t]^{\frac{1}{3}} \quad (8)$$

Where *k* is the correction factor. Because bubble growth rates maybe affected by contact pressure, temperature gradient, and so forth, it is necessary to include a correction factor, *k*. Bubble growth rates for all pores are assumed to be the same, *k* can be calculated by matching the modeling results with the experimental results and has an average value of 1.11.

Once a bubble is generated on the nucleation site, the growth rate, ideally, can be described as

$$\frac{dr}{dt} = \frac{1}{3}[\frac{3k\,n'R_gT}{\pi P_b(2+3\,cos\,\theta - cos^3\theta)}]^{\frac{1}{3}}(t)^{-\frac{2}{3}} \quad (9)$$

And the change rate of bubble velocity is,

$$\frac{d^2r}{dt^2} = -\frac{2}{9}[\frac{3k\,n'R_gT}{\pi P_b(2+3\,cos\,\theta - cos^3\theta)}]^{\frac{1}{3}}(t)^{-\frac{5}{3}} \quad (10)$$

2.6 Results and Discussion

2.6.1 PEMEC performance

In PEMECs, temperature can greatly influence the cell performance and efficiency. Research confirms that the increased temperatures will decrease the total cell voltage. An observation window has been built into the cell features a transparent plastic plate, which will generate a nonuniform pressure distribution along the whole surface and produce more resistance in the transparent cell than in the conventional cell. An IR-free method is introduced into the present study and then ohmic loss will be negligible, which means that the pressure distribution effect on the PEMEC can be neglected for both transparent and conventional cell. For comparison, the test is made at different temperatures with a constant flow rate of 40 ml/min. The final performances at three different temperatures are shown in Figure 4. The cell voltage increases with an increase in current density. The cell temperature is in the unit of °C and varies from 40 °C to 80 °C at a step of 20 °C. Lower voltage at a given current density indicates better PEMEC performance. The best performance (lowest voltage) is obtained when the temperature is 80 °C, whereas the lowest temperature of 40 °C results in the worst performance. The operating voltage reduces from 1.69 V to 1.54 V at 2 A/cm^2, conforming to over 8.8 % of an effective advancement of the temperature increase. Higher temperature in PEMECs exhibits a lower interfacial resistance by enhancing the interfacial contact, improving the proton conductivity within the cell, as well as improving the reactants' diffusion capabilities [58-60].

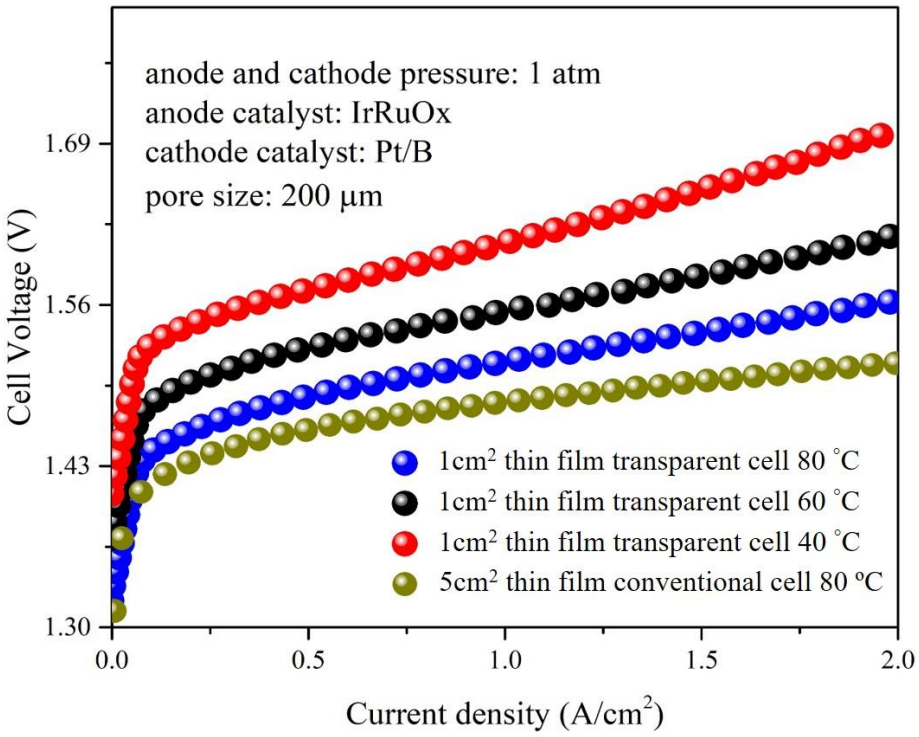

Figure 4. The performance curves under different temperatures, 40 °C, 60 °C, and 80 °C with IR-free method

It should also be noticed that the performance difference between transparent cell and conventional cell is very small, as shown in Figure 4, which provides strong support for the assertion that actual two-phase flow phenomena can be observed in transparent cell.

2.6.2 Two-phase transport in microchannel

In PEMEC microchannels, there are usually four types of two-phase flow regimes, including bubbly, plug, slug, and annular [61]. The most common phenomena, according to the visualization results, are bubbly, annular and slug. Figure 5 chiefly shows the three most common phenomena in the test, with flow direction from left to right. Figure 5A shows the bubbly, Figure 5B is the slug, and Figure 5C is the annular. The black areas within the channel represent the catalyst layer, whereas the grey parts represent the LGDL.

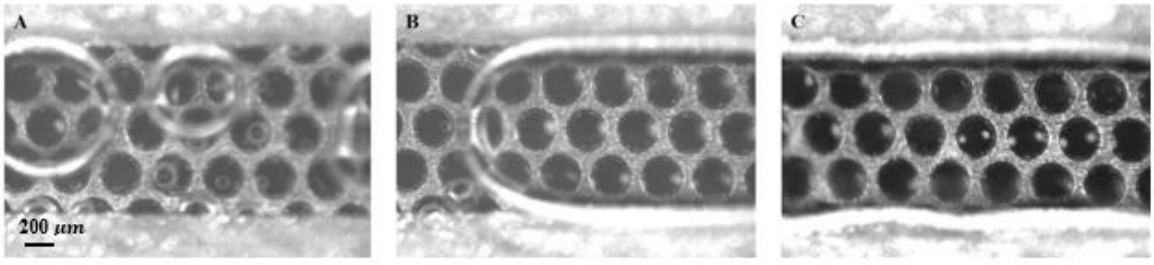

Figure 5. Two-phase flow regime in the microchannel: (A) bubbly, (B) slug and (C) annular.

The transition from bubbly flow to annular flow can be described as follows. Isolated bubbles can be observed in the microchannel, after some large bubbles are formed as a result of bubble coalescence. The larger bubbles are formed through a coalescence process, capturing other single bubbles to rapidly increase in volume. As a result, the increase in the bubble area increases the drag force [62], which moves the mass of bubbles toward the channel outlet to coalesce with many other big bubbles before forming a huge slug. Annular flow occurs as gas generation rate is high, most of gas flows occupied the center of the channel (core area), and water flows near the wall as a thin film. Void fraction in gas liquid flow can be used to define the proportion of gas and liquid rates in the microchannel and can be expressed as $\boldsymbol{\alpha_g = Q_g/(Q_g + Q_l)}$, where $\boldsymbol{Q_g}$ and $\boldsymbol{Q_l}$ are the gas and liquid flow rates [63]. Current density appears to have significant influence on annular flow formation. At low current density, gas generation rate is low, $\boldsymbol{Q_l}$ is dominant over $\boldsymbol{Q_g}$, only bubbly flow can be captured in the microchannel. It has been observed that more gas will be generated in pores as current density increases. Bubbles are more easily to merge together and the annular flow phenomena appears to be more common.

2.6.2.1 Current density effect

Figure 6 shows a sequence of images of pore-scale bubble generation, movement, and reactions. Figure 4A to 4D show bubbles generating at 0.5 A/cm^2, 1.0 A/cm^2, 2.0 A/cm^2 and 4.0 A/cm^2 at 80 °C. Clearly, the reaction sites and bubble diameter vary with current densities.

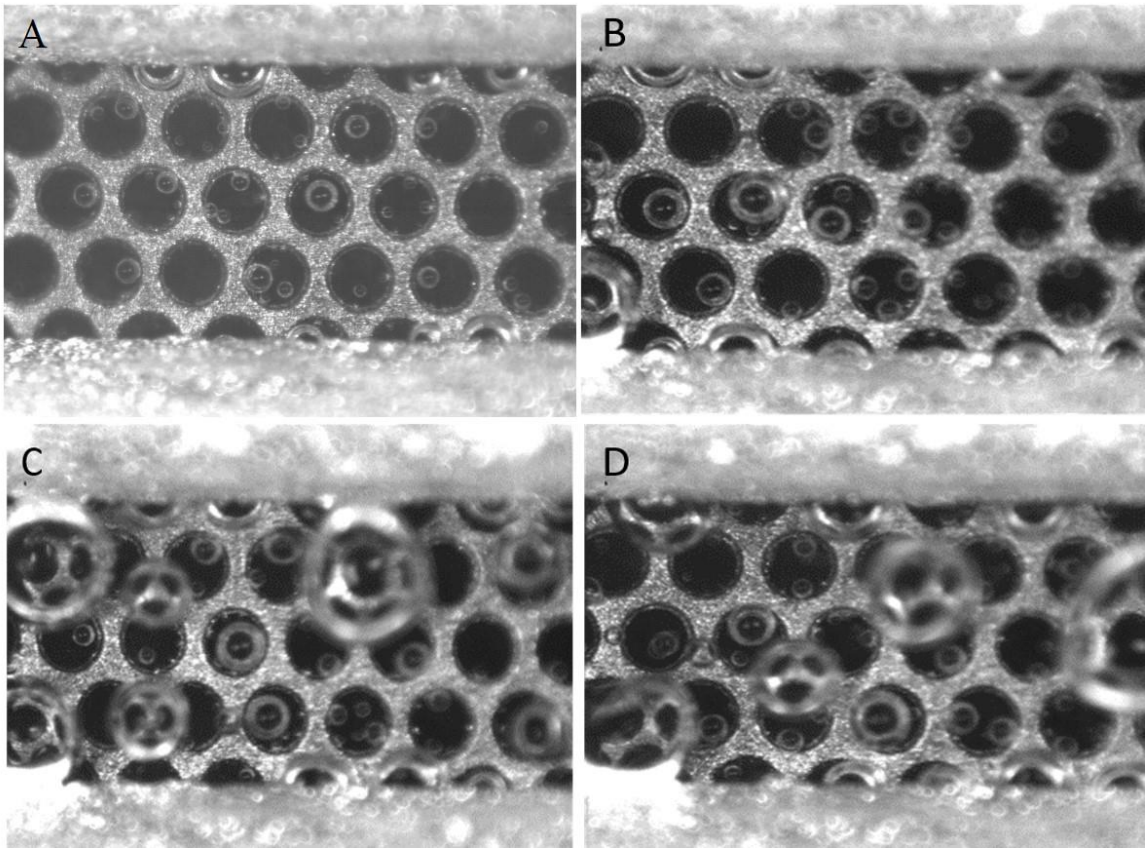

Figure 6. The different bubble evolution phenomena at channel scale under same temperature and flow rate, 80°C and 40ml/min and different current densities. (A) 0.5 A/cm^2, (B) 1.0 A/cm^2, (C) 2.0 A/cm^2, and (D) 4.0 A/cm^2.

Almost no bubbles are generated in several pores when the current density is 0.5 A/cm^2, but bubbles generation can be clearly observed when the current density increases, with bubble diameter and reaction sites significantly increasing as well. This is because bubble generation rates increase underneath the anode surface at higher current densities. At low current density of 0.5 A/cm^2, bubble radius is relatively small and are captured to generate and appear on the rim of pores. The electrochemical reaction is relatively slow and only bubbly flow can exist. With the current density increases, the electrochemical reaction in the catalyst layer will be accelerated. As a result, the number of bubble nucleation site and gas bubble size will both increase [64].

2.6.2.2 Temperature effect

Figure 7 shows the effect of the cell operating temperature on the bubble growth rate at 40 °C, 60 °C, and 80 °C. By comparing bubble growth rate and reaction sites at different temperatures, the bubble radius at 80 °C increases to almost 112.5% of bubble radius at 40 °C. A similar trend can be obtained as the temperature gradually increases. As the temperature is up to 80 °C, the bubble number in the microchannel will also increase to about 1.173 time of the bubble number at 40 °C. These outcomes demonstrate that operating temperature has a degree of influence over oxygen bubble growth. According to the previous electrochemical performance analysis of a PEMEC [65], activation, open circuit voltage, diffusion over-potential, and ohmic loss are definitively linked to the total

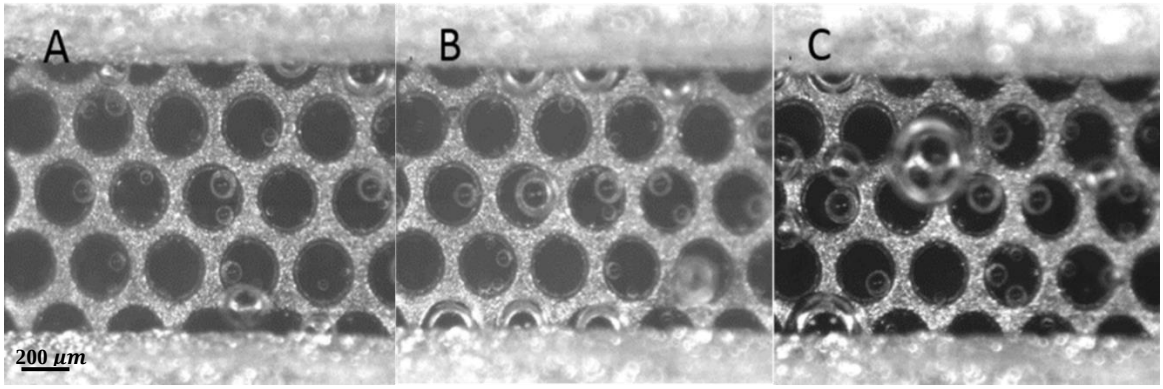

Figure 7. Bubble evolution phenomena in the microchannel under the current density of 0.5 A/cm^2 and flow rate of 40ml/min, and temperatures of (A) 40 °C, (B) 60 °C, and (C) 80 °C.

cell voltage while improving PEMEC performance at the same time. Further analysis shows that the activation over-potential decreases as the operating temperature increases, possibly related to gas/liquid two-phase transport dynamics. In the existing model, bubble growth rate is closely linked to the operating temperature, according to equation (8), and influences the surface tension coefficient which results in a change of the surface tension force. These results indicate that temperature can influence bubble dynamics in the microchannel, and offer a path for future research. In this study, the gas in the channel is assumed to be an ideal gas, so the ideal gas law is applied to derive the growth rate equation to calculate the temperature effect. With the increase in temperature, both bubble volume and growth rate rise, and bubbles are more easily to merge before out of the cell.

2.6.2.3 Flow rate effect

Flow rate appears to have no effect on bubble reaction sites in the microchannel. As depicted in Figure 8, some visualization pictures are captured to show bubble dynamics under 3 different flow rates (A: 10 ml/min, B: 30 ml/min, C: 50 ml/min) when the temperature is 80 °C and the current density is 0.5 A/cm^2. The total number of bubbles under each condition is 34, and the average number of bubbles in a single pore at various flow rate is 1.6. Thus the reaction sites are the same with different flow rates.

2.6.3 Two-phase transport in micro-scale pores

Visualization results are captured in the microchannel with these specifications: 1) height: 1000 μm, 2) width: 500 μm, 3) frame rate: 7500 fps, 4) LGDL thickness: 50 μm thin Ti

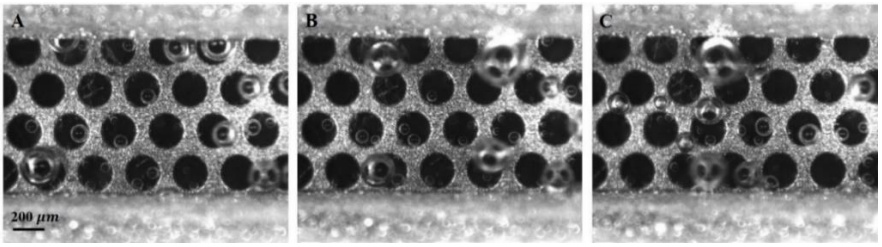

Figure 8. Bubble evolution phenomena in the microchannel under the temperature of 80°C and current density of 0.5 A/cm^2, and different flow rates, (A) 10 ml/min, (B) 30 ml/min, and (C) 50 ml/min.

foil with circle pores all over. The microchannel of PEMEC is entirely full of DI water with a 40 ml/min flow rate and the direction of water flow is from left to right.

2.6.3.1 Current density effect

Images of a sequence of pore-scale gas bubble evolution reactions are displayed in Figure 9. Figures 9A to 9E mainly reflect bubble generation and growth from the surface at 0.5 A/cm^2 and 40 °C. Figures 9F to 9J primarily show bubble generation and growth at 1.0 A/cm^2 and 40 °C. Figures 9K to 9O focus on bubble generation and growth at 4.0 A/cm^2 and 40 °C. A micro gas bubble appears at the rim of the pore and becomes bigger and bigger over the time lapse of the video, and it is confirmed from the movies that there is no bubble coalescence during the bubble growth. Once the bubble detaches, it will flow away within a very short time with the liquid water. In this study, we mainly focused on bubble growth. Since the bubble detachment are affected by many more factors, the detached bubble diameters will be varied at different sites, which can be observed in the flow channel. In Figure 9B, multiple oxygen bubbles with different sizes can clearly be observed along the rim of the pore. In Figure 9C and 9D, the bubble size continues to increase. In Figure 7E, bubbles are in the process of detaching from the surface. Similar reactions are observed when the current density is increased to 1.0 A/cm^2 and 4.0 A/cm^2 at the same temperature. However, both the growth rate and the reaction sites have been increased greatly. A local increase in supersaturating ratio in the pores can be heightened with an

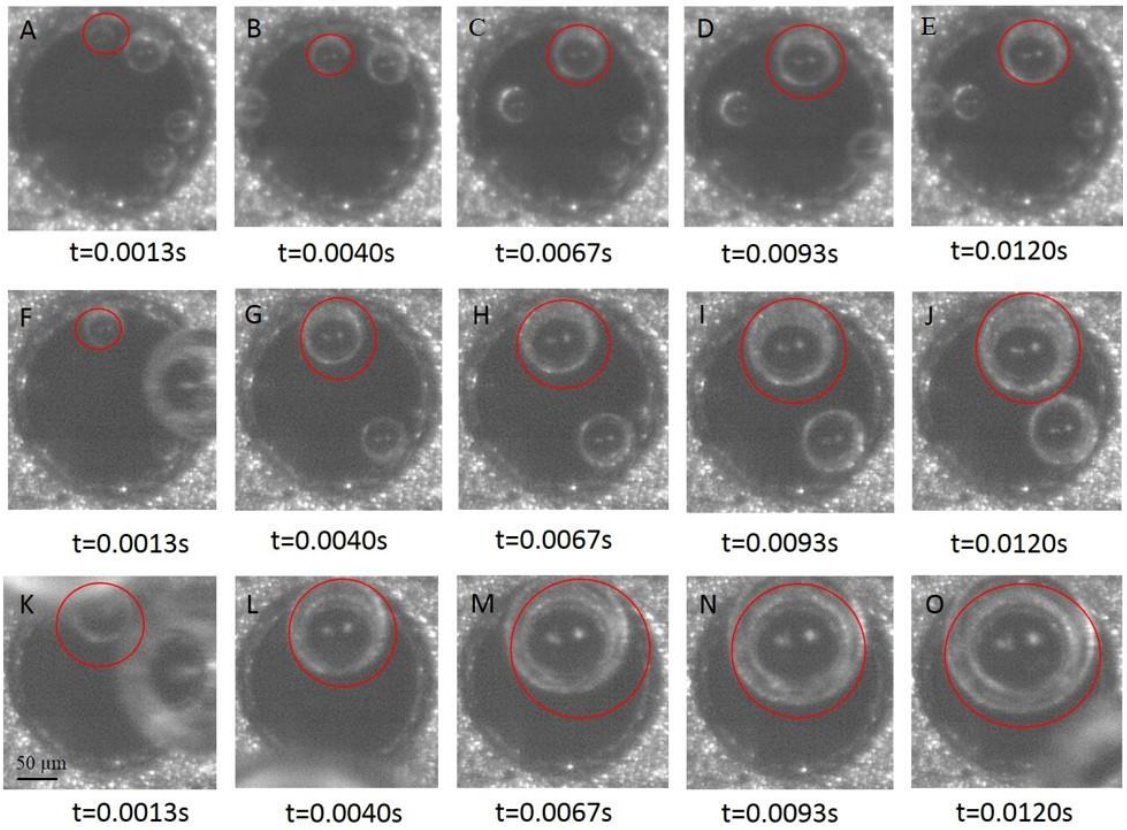

Figure 9. Sequence of photographs showing the bubble evolution at pore scale under different current densities, (A) to (E) bubbles growth at 0.5 A/cm^2, (F) to (J) bubbles growth at 1.0 A/cm^2, (K) to (O) bubbles growth at 4.0 A/cm^2.

increase in current density. This condition also enhances the bubble nucleation process on the surface [66].

The process for calculating the total number of bubbles at 0.5 A/cm^2 can be summarized as follows:

As shown in Figure 10, the total number of bubbles in a section of the microchannel are 29 at 0.5 A/cm^2, and the number of bubbles in one pore is 1.93. The area of the LGDL is 1 cm^2, and the porosity is 0.55, which is also the total area of the pores in the channel. Fig. 8 was captured from a high-speed visualization movie. Some detached bubbles in the field were flowed from the upstream, and were not counted in the calculation. They were not highlighted in red circle in Fig. 10.

The total number of bubbles in the channel at 0.5 A/cm^2 can be calculated as,

$$N_* = \frac{A}{A_{one\ pore}} \times N_{one\ pore} \tag{11}$$

Where A is the total area of the pores on LGDL and has a value of 0.55 cm^2, $A_{one\ pore}$ is the area of one pore and has a value of 0.000314 cm^2

Similar process can be used to get the total number of bubbles at 1.0 A/cm^2 and 4.0 A/cm^2. It should be noticed that the total bubble number, N, was estimated based on the local field of vision from the visualization movie. Some bubbles in the field were not counted in the calculation because they were flowed from the upstream.

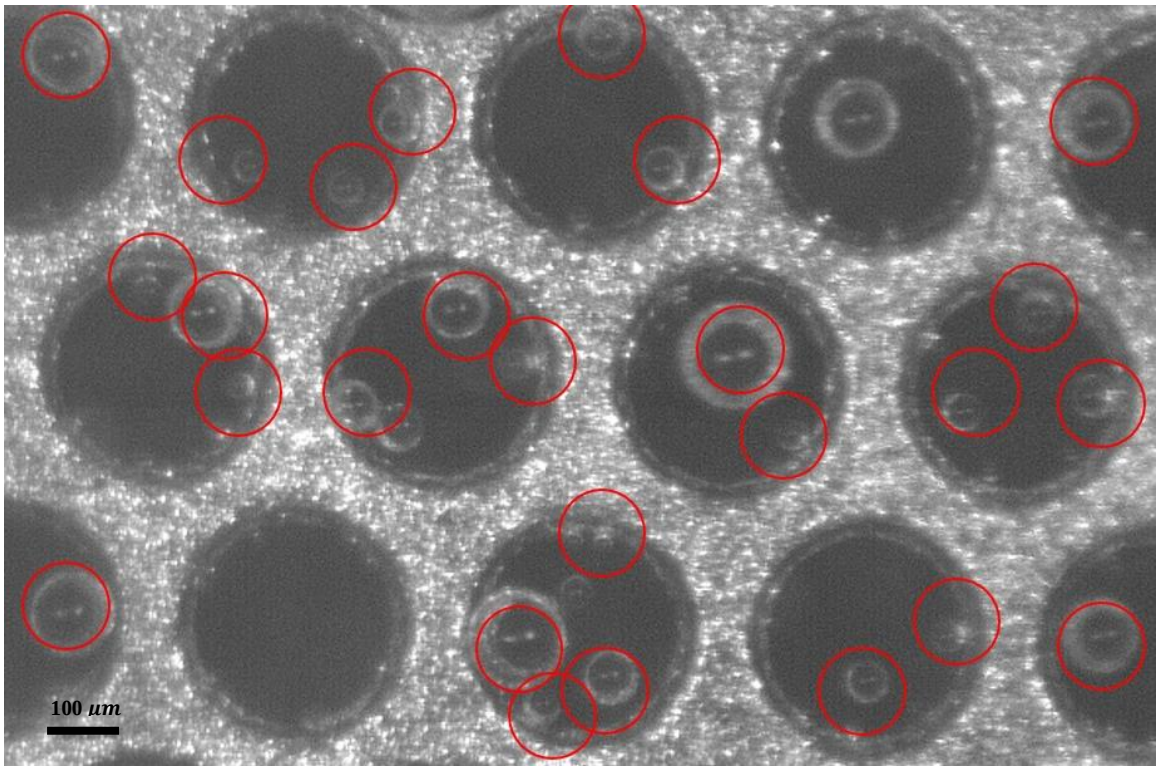

Figure 10. Number of bubbles in 15 pores

Figure 11 presents the time evolution of bubble growth diameter at three different current densities including 0.5 A/cm^2, 1.0 A/cm^2, and 4.0 A/cm^2. It is evident that current density has a considerable influence on oxygen bubble growth rate. At the low current density of 0.5 A/cm^2, the bubble diameter is small directly as a result of the slow process of electrochemical reaction. As the current density increases, the electrochemical reaction in a CL will become faster. More gas will be generated from a nucleation site, and thus gas bubble diameter increases. Before using a mathematical model in the forecasting of bubble growth trend, the model is calculated and authenticated using our previous visualization assessment data. Figure 11 presents the evaluation of model data with assessment data derived from oxygen bubble growth inside a PEMEC, under the same operational parameters. The result obtained from the figure shows an excellent agreement between the simulation and experiment when the total number of bubbles in the channel for 0.5 A/cm^2, 1.0 A/cm^2 and 4.0 A/cm^2 are 29, 37 and 56, respectively.

2.6.3.2 Temperature effect

According to the present growth model, the bubble size is strongly related to the operating temperature. Temperature will have a significant influence on the bubble dynamics and two-phase flow behavior inside a PEMEC. The effect of temperature on bubble growth within a single pore is demonstrated in Figure 12. The generation and growth dynamics of bubbles are shown at 0.5 A/cm^2 for two temperatures, 40 °C for Figures A to E and 80 °C for Figures F to J. As shown in Figures, for a given initial bubble diameter, the diameter

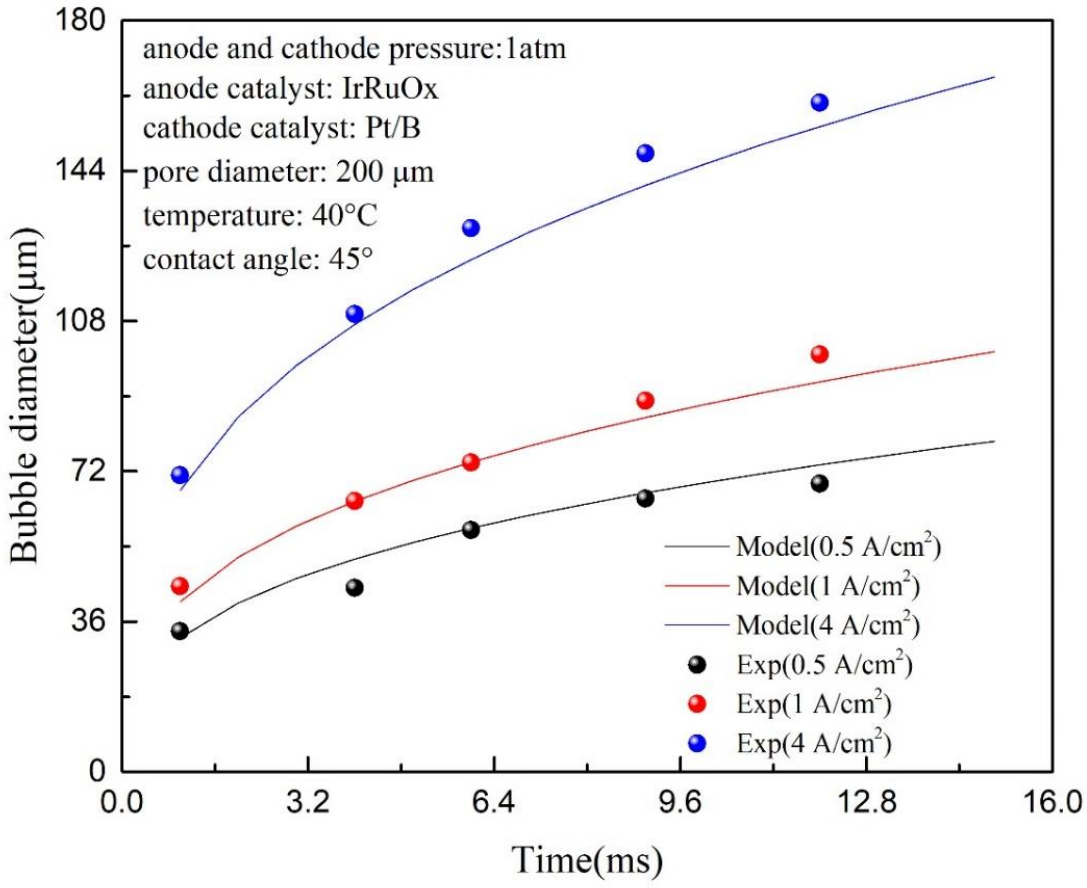

Figure 11. Comparison of the modeling data and experimental data for oxygen bubble growth in PEMECs at 0.5 A/cm^2, 1.0 A/cm^2, and 4.0 A/cm^2.

tends to increase with the lapse of time for the higher temperature. Equation (8) has been used to elucidate the effects of temperatures on bubble growth, showing that bubble growth velocity increases with heightened temperatures by approximately 3% for every 10 K. The effect of the surrounding temperature on bubble growth rate is called the thermal effect, and it can cause quite a dramatic difference on resulting bubble dynamics. At a higher temperature, more bubbles are generated from the site of nucleation, and some small bubbles tend to combine to produce a large bubble. As the bubbles size increases, this phenomena become more and more significant.

Figure 13 presents the experimental versus modeling data for oxygen bubble growth inside a PEMEC under the same operating conditions. Modeling results show a strong correlation with the experimental results. The total number of bubbles in the channel for 40°C and 80 °C are 29 and 30 respectively. The modeling results in Figure 13 indicate that the bubble diameter increases from about 36 to 88 μm at 80 °C and rises up from about 33 μm to 68 μm at 40 °C. When the time is equal to 9.9 ms, comparing the bubble diameter at a temperature of 40 °C and at a temperature of 80 °C, the bubble radius at 80 °C is a relatively larger than one at 40 °C. A similar trend can be obtained as time gradually increases. Equation (6) indicates that bubble diameter has an important correlation to the temperature. Bubble diameter increases along with the temperature.

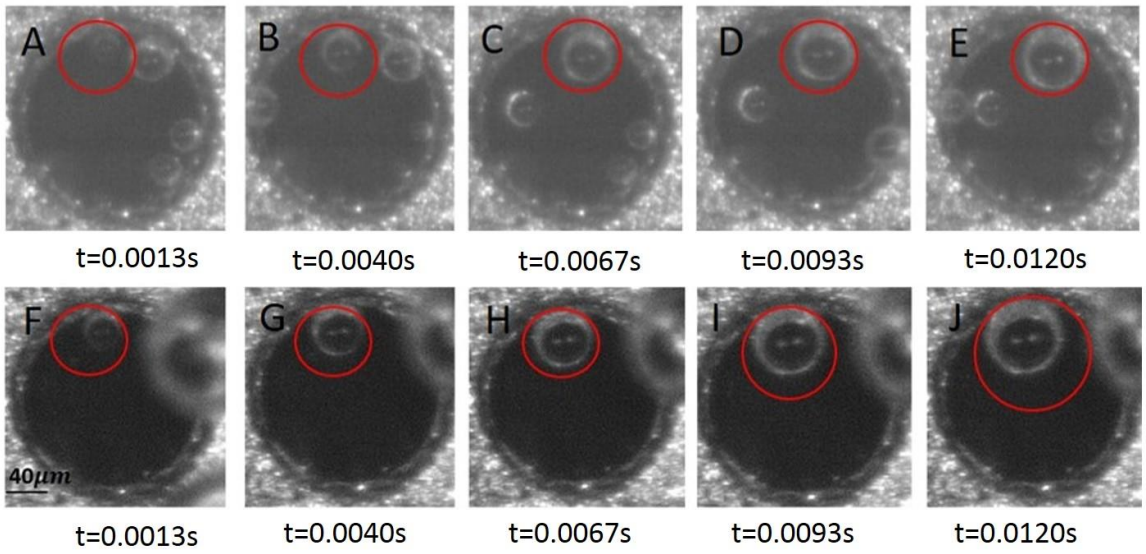

Figure 12. Sequence of photographs showing the bubble evolution at pore scale under different temperatures. (A) to (E) bubbles growth at 40 °C, (F) to (J) bubbles growth at 80 °C.

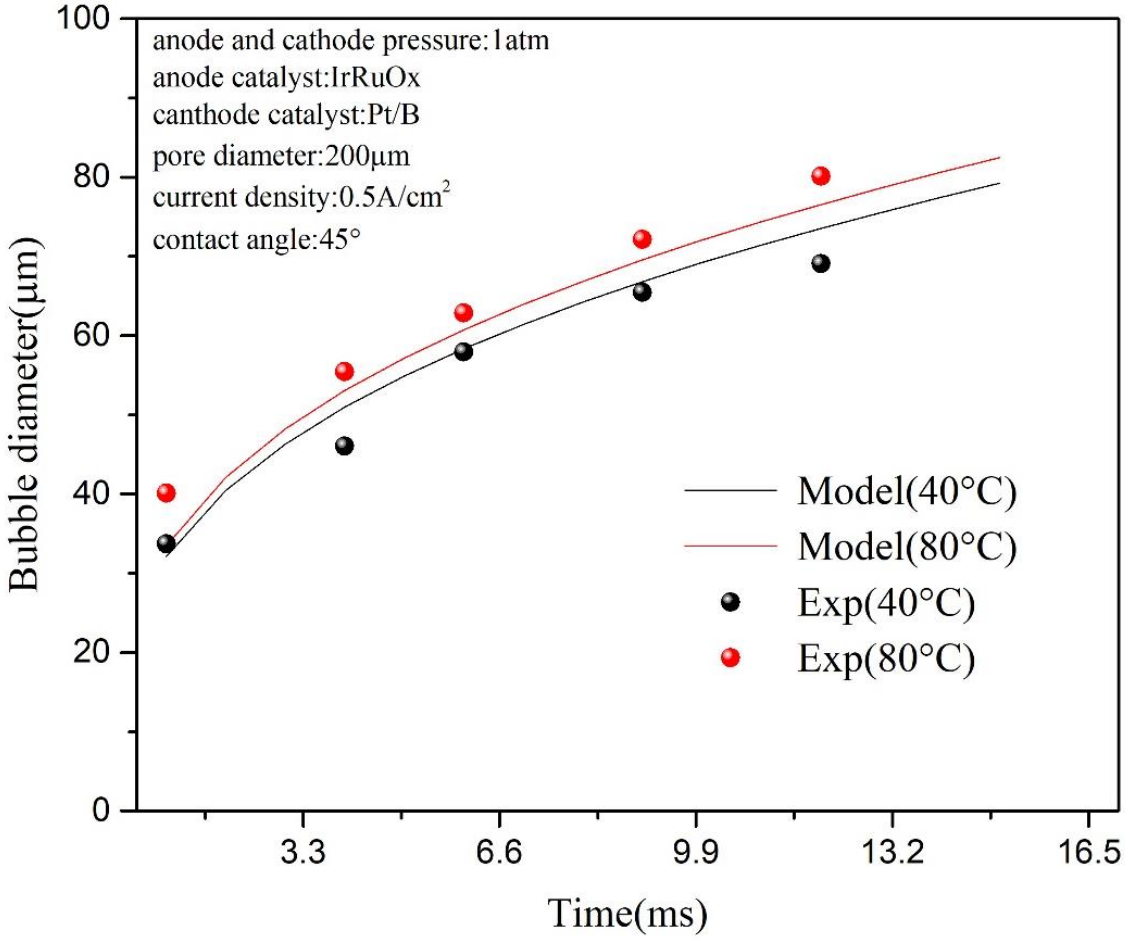

Figure 13. Comparison of the modeling data and experimental data for oxygen bubble growth in PEMECs for different temperatures, 40 °C and 80 °C.

2.6.3.3 Flow rate effect

Figure 14 depicts the bubble growth behaviors at the flow rates of 10 ml/min and 30 ml/min under the same temperature of 80 °C and the same current density of 1.0 A/cm^2. The flow rate is found to have no influence on the bubble generation rate in either microchannel or micropore, with the bubble diameters of 63 μm at 0.001 s, 71 μm at 0.004 s, 85 μm at 0.006 s, and 101 μm at 0.009 s.

2.7 Summary

In this study, the rapid and micro-scale oxygen bubble dynamics and two-phase flow at the anode side of PEMECs are visualized in-situ in a specific designed transparent PEMEC coupled with a high-speed and micro-scale visualization system. The similar performance between the transparent and conventional cells provides strong support for the assertion that actual two-phase flow phenomena can be observed in the transparent cell. At channel scales, several two-phase flow phenomena in microchannels, including bubbly, slug and annular flow, have been observed. At pore scales, oxygen gas bubbles are emerged at the rim of the LGDL pores and rapidly grow until detaching from the reaction sites. And then, they coalesce with other micro bubbles or flow with liquid water in the microchannel. It is found that the PEMEC temperature and current density enhance bubble growth rates and increase the number of reaction sites, while its flow rate has limited effects. In addition, a mathematical model has been developed to investigate the bubble growth behavior under different operating conditions, and the modeling results are in good agreement with the

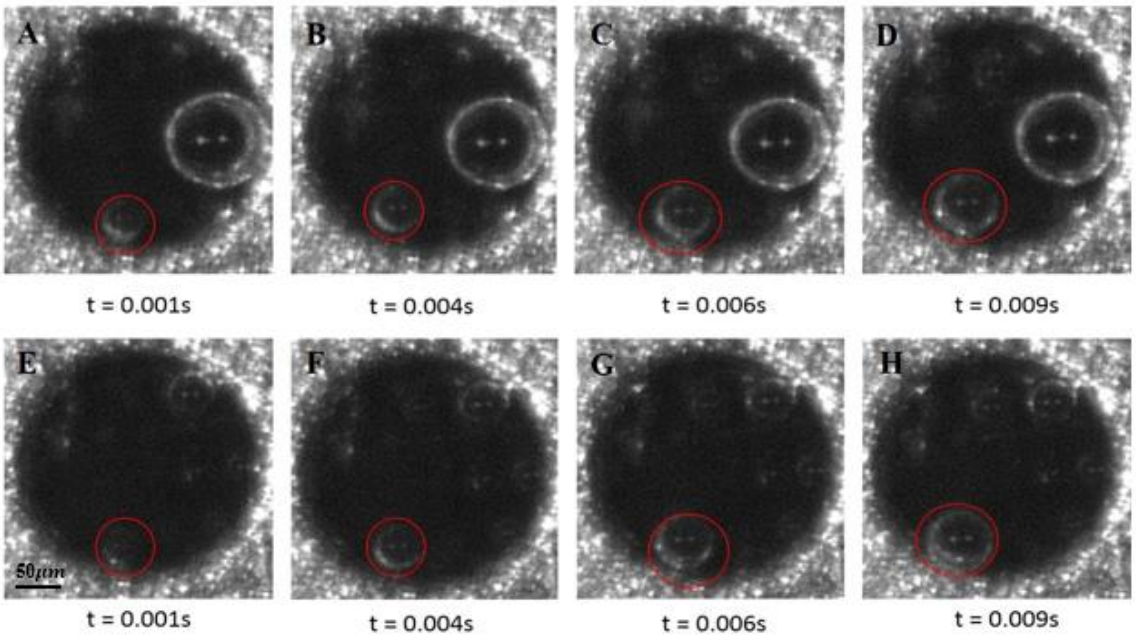

Figure 14. Sequence of photographs showing the bubble evolution at pore scale under different flow rates: (A) to (D) 10 ml/min, (E) to (H) 30 ml/min, with the temperature of 80 °C and the current density of 1.0 A/cm^2.

experimental data. This research opens a new pathway for further study of the general working mechanism and two-phase flow in PEMECs, thereby allows the creation of new advanced designs and research methods.

References

1. Zhang, F., et al., The survey of key technologies in hydrogen energy storage. International Journal of Hydrogen Energy, 2016. 41(33): p. 14535-14552.
2. Kang, Z., et al., Novel Thin/Tunable Gas Diffusion Electrodes with Ultra-Low Catalyst Loading for Hydrogen Evolution Reactions in Proton Exchange Membrane Electrolyzer Cells. Nano Energy, 2018.
3. Yang, G., et al., Fully printed and integrated electrolyzer cells with additive manufacturing for high-efficiency water splitting. Applied Energy, 2018. 215: p. 202-210.
4. Carmo, M., et al., A comprehensive review on PEM water electrolysis. International journal of hydrogen energy, 2013. 38(12): p. 4901-4934.
5. Schalenbach, M., et al., Pressurized PEM water electrolysis: Efficiency and gas crossover. International Journal of Hydrogen Energy, 2013. 38(35): p. 14921-14933.
6. Abdin, Z., C.J. Webb, and E.M. Gray, Modelling and simulation of a proton exchange membrane (PEM) electrolyser cell. International Journal of Hydrogen Energy, 2015. 40(39): p. 13243-13257.
7. Marangio, F., M. Santarelli, and M. Cali, Theoretical model and experimental analysis of a high pressure PEM water electrolyser for hydrogen production. International Journal of Hydrogen Energy, 2009. 34(3): p. 1143-1158.

8. Awasthi, A., K. Scott, and S. Basu, Dynamic modeling and simulation of a proton exchange membrane electrolyzer for hydrogen production. International Journal of Hydrogen Energy, 2011. 36(22): p. 14779-14786.
9. Gorgun, H., Dynamic modelling of a proton exchange membrane (PEM) electrolyzer. International Journal of Hydrogen Energy, 2006. 31(1): p. 29-38.
10. Ayers, K.E., et al., Research advances towards low cost, high efficiency PEM electrolysis. ECS Transactions, 2010. 33(1): p. 3-15.
11. Toops, T.J., et al., Evaluation of nitrided titanium separator plates for proton exchange membrane electrolyzer cells. Journal of Power Sources, 2014. 272: p. 954-960.
12. Mo, J.K., et al., Electrochemical investigation of stainless steel corrosion in a proton exchange membrane electrolyzer cell. International Journal of Hydrogen Energy, 2015. 40(36): p. 12506-12511.
13. Kang, Z., et al., Investigation of thin/well-tunable liquid/gas diffusion layers exhibiting superior multifunctional performance in low-temperature electrolytic water splitting Energy & Environmental Science 2017. 10(1): p. 10.
14. Mo, J.K., et al., Discovery of true electrochemical reactions for ultrahigh catalyst mass activity in water splitting. Science Advances, 2016. 2(11).
15. Kang, Z., et al., Novel thin/tunable gas diffusion electrodes with ultra-low catalyst loading for hydrogen evolution reactions in proton exchange membrane electrolyzer cells. Nano Energy, 2018. 47: p. 434-441.

16. Mo, J., et al., In situ investigation on ultrafast oxygen evolution reactions of water splitting in proton exchange membrane electrolyzer cells. Journal of Materials Chemistry A, 2017. 5(35): p. 18469-18475.

17. Sakuma, G., Y. Fukunaka, and H. Matsushima, Nucleation and growth of electrolytic gas bubbles under microgravity. International Journal of Hydrogen Energy, 2014. 39(15): p. 7638-7645.

18. Lafmejani, S.S., A.C. Olesen, and S.K. Kær, VOF modelling of gas–liquid flow in PEM water electrolysis cell micro-channels. International Journal of Hydrogen Energy, 2017.

19. Ito, K., et al., Analysis and visualization of water flow impact on hydrogen production efficiency in solid polymer water electrolyzer under high-pressure condition. International Journal of Hydrogen Energy, 2015. 40(18): p. 5995-6003.

20. Dedigama, I., et al., Current density mapping and optical flow visualisation of a polymer electrolyte membrane water electrolyser. Journal of Power Sources, 2014. 265: p. 97-103.

21. Chandran, P., S. Bakshi, and D. Chatterjee, Study on the characteristics of hydrogen bubble formation and its transport during electrolysis of water. Chemical Engineering Science, 2015. 138: p. 99-109.

22. Han, B., et al., Effects of membrane electrode assembly properties on two-phase transport and performance in proton exchange membrane electrolyzer cells. Electrochimica Acta, 2016. 188: p. 317-326.

23. Han, B., et al., Modeling of two-phase transport in proton exchange membrane electrolyzer cells for hydrogen energy. International Journal of Hydrogen Energy, 2017. 42(7): p. 4478-4489.

24. Thomas, Y.R., et al., New method for super hydrophobic treatment of gas diffusion layers for proton exchange membrane fuel cells using electrochemical reduction of diazonium salts. ACS applied materials & interfaces, 2015. 7(27): p. 15068-15077.

25. Han, B., et al., Electrochemical performance modeling of a proton exchange membrane electrolyzer cell for hydrogen energy. International Journal of Hydrogen Energy, 2015. 40(22): p. 7006-7016.

26. Yang, X.G., et al., Dynamics of Single Hydrogen Bubbles at a Platinum Microelectrode. Langmuir, 2015. 31(29): p. 8184-8193.

27. Zhang, F.Y., X.G. Yang, and C.Y. Wang, Liquid water removal from a polymer electrolyte fuel cell. Journal of the Electrochemical Society, 2006. 153(2): p. A225-A232.

28. Yang, X.G., et al., Visualization of liquid water transport in a PEFC. Electrochemical and Solid State Letters, 2004. 7(11): p. A408-A411.

29. Zhang, F.Y., S.G. Advani, and A.K. Prasad, Performance of a metallic gas diffusion layer for PEM fuel cells. Journal of Power Sources, 2008. 176(1): p. 293-298.

30. Zhang, F.Y., A.K. Prasad, and S. Advani, Nano-based gas diffusion media. 2010, US7785748

31. Zhang, F.-Y., S.G. Advani, and A.K. Prasad, Performance of a metallic gas diffusion layer for PEM fuel cells. Journal of power sources, 2008. 176(1): p. 293-298.

32. Kumbur, E., K. Sharp, and M. Mench, A design tool for predicting the capillary transport characteristics of fuel cell diffusion media using an artificial neural network. Journal of Power Sources, 2008. 176(1): p. 191-199.

33. Kumbur, E., K. Sharp, and M. Mench, On the effectiveness of Leverett approach for describing the water transport in fuel cell diffusion media. Journal of Power Sources, 2007. 168(2): p. 356-368.

34. LaManna, J.M., et al., Measurement of capillary pressure in fuel cell diffusion media, micro-porous layers, catalyst layers, and interfaces. Journal of Power Sources, 2014. 271: p. 180-186.

35. Cubaud, T., U. Ulmanella, and C.-M. Ho, Two-phase flow in microchannels with surface modifications. Fluid Dynamics Research, 2006. 38(11): p. 772-786.

36. Meng, H. and C.-Y. Wang, Model of two-phase flow and flooding dynamics in polymer electrolyte fuel cells. Journal of the Electrochemical Society, 2005. 152(9): p. A1733-A1741.

37. Meng, H., Numerical studies of liquid water behaviors in PEM fuel cell cathode considering transport across different porous layers. international journal of hydrogen energy, 2010. 35(11): p. 5569-5579.

38. Wang, Y., Modeling of two-phase transport in the diffusion media of polymer electrolyte fuel cells. Journal of Power Sources, 2008. 185(1): p. 261-271.

39. Wang, Y., et al., Stochastic modeling and direct simulation of the diffusion media for polymer electrolyte fuel cells. International journal of heat and mass transfer, 2010. 53(5-6): p. 1128-1138.

40. Liao, Q., et al., Visualization study on the dynamics of CO 2 bubbles in anode channels and performance of a DMFC. Journal of Power Sources, 2007. 171(2): p. 644-651.

41. Jouhara, H., B. Fadhl, and L.C. Wrobel, Three-dimensional CFD simulation of geyser boiling in a two-phase closed thermosyphon. International Journal of Hydrogen Energy, 2016. 41(37): p. 16463-16476.

42. Fernandez, D., et al., Bubble Formation at a Gas-Evolving Microelectrode. Langmuir, 2014. 30(43): p. 13065-13074.

43. Matsushima, H., Y. Fukunaka, and K. Kuribayashi, Water electrolysis under microgravity. Part II. Description of gas bubble evolution phenomena. Electrochimica Acta, 2006. 51(20): p. 4190-4198.

44. Matsushima, H., et al., Single bubble growth during water electrolysis under microgravity. Electrochemistry Communications, 2009. 11(8): p. 1721-1723.

45. Selamet, O.F., et al., Investigation of gas generation in regenerative fuel cells by low-energy X-rays. Journal of Power Sources, 2015. 296: p. 133-141.

46. Selamet, O., et al., Two-phase flow in a proton exchange membrane electrolyzer visualized in situ by simultaneous neutron radiography and optical imaging. international journal of hydrogen energy, 2013. 38(14): p. 5823-5835.

47. Bozorgnezhad, A., et al., Two-phase flow and droplet behavior in microchannels of PEM fuel cell. International Journal of Hydrogen Energy, 2016. 41(42): p. 19164-19181.

48. Mei, R., W. Chen, and J.F. Klausner, Vapor bubble growth in heterogeneous boiling—I. Formulation. International Journal of Heat and Mass Transfer, 1995. 38(5): p. 909-919.

49. Mei, R., W. Chen, and J.F. Klausner, Vapor bubble growth in heterogeneous boiling—II. Growth rate and thermal fields. International Journal of Heat and Mass Transfer, 1995. 38(5): p. 921-934.

50. Mo, J., et al., Thin liquid/gas diffusion layers for high-efficiency hydrogen production from water splitting. Applied Energy, 2016. 177: p. 817-822.

51. Yang, G., et al., Additive manufactured bipolar plate for high-efficiency hydrogen production in proton exchange membrane electrolyzer cells. International Journal of Hydrogen Energy, 2017. 42(21): p. 14734-14740.

52. Chen, D.Q., L.M. Pan, and S. Ren, Prediction of bubble detachment diameter in flow boiling based on force analysis. Nuclear Engineering and Design, 2012. 243: p. 263-271.

53. Sillen, C.W.M.P., et al., Gas Bubble Behavior during Water Electrolysis. International Journal of Hydrogen Energy, 1982. 7(7): p. 577-587.

54. Liu, H.B., et al., Hydrogen bubble growth at micro-electrode under magnetic field. Journal of Electroanalytical Chemistry, 2015. 754: p. 22-29.

55. Fu, B.R. and C. Pan, Bubble growth with chemical reactions in microchannels. International Journal of Heat and Mass Transfer, 2009. 52(3-4): p. 767-776.

56. Arbabi, F., et al., Three-Dimensional Computational Fluid Dynamics Modelling of Oxygen Bubble Transport in Polymer Electrolyte Membrane Electrolyzer Porous Transport Layers. Journal of the Electrochemical Society, 2016. 163(11): p. F3062-F3069.

57. Mo, J., Fundamental Studies of Electrochemical Reactions and Microfluidics in Proton Exchange Membrane Electrolyzer Cells. 2016.

58. Han, F.D., et al., Electrochemical Stability of Li10GeP2S12 and Li7La3Zr2O12 Solid Electrolytes. Advanced Energy Materials, 2016. 6(8).

59. Du, C.Y., et al., Effective protonic and electronic conductivity of the catalyst layers in proton exchange membrane fuel cells. Electrochemistry Communications, 2004. 6(5): p. 435-440.

60. Zenyuk, I.V., E.C. Kumbur, and S. Litster, Deterministic contact mechanics model applied to electrode interfaces in polymer electrolyte fuel cells and interfacial water accumulation. Journal of Power Sources, 2013. 241: p. 379-387.

61. Mo, J., et al. Visualization on rapid and micro-scale dynamics of oxygen bubble evolution in PEMECs. in Nano/Micro Engineered and Molecular Systems (NEMS), 2017 IEEE 12th International Conference on. 2017. IEEE.

62. Klausner, J.F., et al., Vapor Bubble Departure in Forced-Convection Boiling. International Journal of Heat and Mass Transfer, 1993. 36(3): p. 651-662.

63. Cubaud, T., et al., Bubble dispenser in microfluidic devices. Physical Review E, 2005. 72(3): p. 037302.

64. Chen, Q.J., L. Luo, and H.S. White, Electrochemical Generation of a Hydrogen Bubble at a Recessed Platinum Nanopore Electrode. Langmuir, 2015. 31(15): p. 4573-4581.

65. Kang, Z., et al., Performance Modeling and Current Mapping of Proton Exchange Membrane Electrolyzer Cells with Novel Thin/Tunable Liquid/Gas Diffusion Layers. Electrochimica Acta, 2017. 255: p. 405-416.

66. Nouri-Khorasani, A., et al., Model of oxygen bubbles and performance impact in the porous transport layer of PEM water electrolysis cells. International Journal of Hydrogen Energy, 2017.

CHAPTER III

WETTABILITY EFFECTS OF THIN TITANIUM LIQUID/GAS DIFFUSION LAYERS IN PROTON EXCHANGE MEMBRANE ELECTROLYZER CELLS

A version of this chapter was originally published by Yifan Li:

Yifan Li, Zhenye Kang, Xuanli Deng, Gaoqiang Yang, Shule Yu, Jingke Mo, Derrick A.Talley, G. Kane Jennings, and Feng-Yuan Zhang. "Wettability effects of thin titanium liquid/gas diffusion layers in proton exchange membrane electrolyzer cells." *Electrochimica Acta* 298 (2019): 704-708.

I am fully responsible for the work submitted in these publications.

3.1 Abstract

Wettability of titanium thin/tunable liquid/gas diffusion layers (TT-LGDLs) may affect the oxygen bubble dynamics and detachment process, and impact the performance (cell voltage) in proton exchange membrane electrolyzer cells (PEMECs). In this study, a silane monolayer is applied to tune the TT-LGDL wettability for the first time. The ultra-fast and micro-scale oxygen gas bubble dynamics and the two-phase flow in the channel are studied in situ for hydrophobically treated and hydrophilic titanium thin/tunable LGDLs (TT-LGDLs) with a high-speed and micro-scale visualization system (HMVS). The HMVS shows that the micro oxygen bubbles occur only along the CL/TT-LGDL interfaces at the rim of pores on TT-LGDLs. Bubbles more easily coalescence to form a large one in hydrophobic TT-LGDLs. Pore-scale analysis on the single bubble evolution process shows that the detachment diameter and frequency of oxygen bubbles in the hydrophobic TT-LGDLs are much larger than those in the hydrophilic TT-LGDLs. The PEMEC performance with the hydrophobic and hydrophilic TT-LGDLs are very close under 2.0

A/cm^2, which means that the wettability has limited effect on TT-LGDLs mainly due to their thin features and unique structures with straight pores.

3.2 Highlights

- Silane monolayers were applied onto TT-LGDLs to alter their wettability.
- The TT-LGDL wettability can be tuned from hydrophilic to hydrophobic.
- Both the two-phase flow and bubble dynamics are *in-situ* visualized.
- The oxygen bubble detachment diameter is increased when the hydrophobic TT-LGDLs are applied.
- The wettability has limited effects on PEMEC performance under 2.0 A/cm^2 and 80 °C.

3.3 Introduction

Efficient production of hydrogen can lead to the development of a "hydrogen society" with close-to-zero emission of pollutants and limited environmental impact [1-6]. Proton exchange membrane electrolyzer cells (PEMEC) have been considered as one of the most promising energy storage/conversion devices for hydrogen production, especially when coupled with intermittent sustainable energy resources, including solar, wind, tides, etc., due to the advantages of high purity products, quick response, high working current density, and compact design [7-10]. Many researchers have focused on developing high-efficiency, low-cost, and durable PEMECs based on the design of novel materials and

structures and the study of two-phase flow and bubble dynamics in PEMECs, and the effect of bubble dynamics on the performance is very attractive [11-16].

The typical PEMEC has a similar configuration of a PEM fuel cell (PEMFC), which consists of a membrane electrode assembly (MEA) sandwiched by liquid/gas diffusion layers (LGDLs), bipolar plates (BPs), and end plates. LGDLs, which are located between the catalyst layers (CLs) and BPs, have a porous structure and must meet certain requirements. During operation, the water transported from the BP flow field to the CLs is split into molecular oxygen, electrons, and protons at the anode side. Then, the produced oxygen gas should be effectively removed from the surface of the CLs to avoid blocking the water pathway. Electrons are transported from the CLs through the LGDLs and BPs to the external circuit [17]. Thus, LGDLs should transport electrons, heat, and reactants/products simultaneously with minimal losses [18-20]. In addition, the structures, materials, and properties of the anode LGDLs have a great impact on PEMEC performance, and efficient mass transport of liquid water and oxygen gas is critical for stable PEMEC operation. Despite its importance, however, correlation between LGDL properties, PEMEC performance, and the oxygen bubble dynamics has not been extensively studied.

Previous researchers have found that an optimum amount of coating by a hydrophobic agent on GDLs, such as polytetrafluoroethylene (PTFE) or fluorinated ethylene propylene (FEP), have important impacts on two-phase transport and PEMFC performance by facilitating liquid water removal [21-30]. Zhang et al. in-situ visualized the liquid water droplet formation, growth, and detachment on GDLs and catalyst layers, and revealed the

liquid water removal mechanism in flow channels of PEMFCs [31-33]. Mortazavi et al. have investigated the effects of PTFE in GDLs on water droplet growth and detachment in the flow channels. They report that the droplet has a smaller detachment size from the GDL surface with the more hydrophobic PTFE coating due to its effect on the capillary pressure and surface roughness [34, 35]. Koresawa et al. developed a desired wettability distribution GDL by applying the hydrophobic coating locally and leaving the other regions unchanged. They found that the oxygen diffusivity with 10-20 wt% PTFE in the hydrophobic region was increased three times compared to the GDLs with a homogeneous wettability [36]. Lim et al. investigated FEP hydrophobic polymer content in a carbon paper GDL on the power performance of H_2/air PEMECs. The contact angle measurements indicate a similar level of hydrophobicity among GDLs impregnated with different amounts of FEP ranging from 10 to 40 wt% [37]. Litster et al. employed fluorescence microscopy with a novel methodology to provide new insight into the dynamic behavior and distribution of liquid water as it is transported through the gas diffusion layers in PEMECs. The experimental observations led to the postulation of the primary mechanism for liquid water transport in hydrophobic GDLs [38]. Pasaogullari et al. examined the governing physics of liquid water transport in hydrophobic GDLs. They observed that capillary transport is the dominant transport process to remove water from flooded GDLs [39]. Very few studies have investigated the effects of GDL wettability in unitized regenerative fuel cells (URFCs) and PEMECs. Ioroi et al. said that PTFE in hydrogen electrode GDLs has nearly no effect on cell performance in both FC and EC modes, but the PTFE in oxygen electrode GDLs had

a negative impact on URFC performance in EC mode and improved performance in FC mode especially under fully wet working conditions [40]. But on the contrary, Hwang et al. found that the PTFE coating has no effect on URFC performance under the EC mode. They also said that the PTFE coating in titanium GDLs can improve the URFC performance under both dry and wet conditions in FC mode, while it will negatively impact the performance under mid-range humidity [41-43]. Kang et al. developed a novel thin/tunable gas diffusion electrode, and achieved a very good performance. More significantly, the Pt mass activity for hydrogen evolution reaction has also been greatly increased [44].

The treatment of GDLs in PEMFCs have been fully investigated; however, research focused on ultrathin LGDL hydrophobic treatment in PEMECs has never been reported. The relations between the GDL wettability, gas bubble dynamics, and PEMEC performance are still unknown. Therefore, thorough analysis is needed for better understanding of how the wettability changes the bubble dynamics and impacts PEMEC performance.

In this study, the Ti based thin/tunable LGDLs (TT-LGDLs) are hydrophobically treated by a monolayer film from n-octadecyltrichlorosilane in one simple step. Both the fresh TT-LGDLs and the hydrophobic TT-LGDLs are characterized both *in-situ* and *ex-situ*. The wettability of the two TT-LGDLs are measured by water contact angle. By taking advantages of the in-house built high-speed and micro-scale visualization system (HMVS), novel TT-LGDLs and the transparent PEMECs, the oxygen bubble dynamics, and the two-

phase flow phenomenon in an operating PEMEC are captured *in-situ*. The PEMEC performance between the two TT-LGDLs is also tested, and the relation between the performance and wettability is analyzed. The results obtained in this study point out the direction for optimized LGDL wettability and the new method for investigation of the bubble dynamics in PEMECs.

3.4 Experimental details

A TT-LGDL was used in this study, and was experimental measured with a microscope, the thickness is 25 μm, the porosity is 55%, a circular pore shape, and a pore diameter of ~300 μm. In our previous studies, the TT-LGDLs achieved excellent PEMEC performance [20, 45-47] and their straight-through pores allow the *in-situ* visualization of oxygen bubble dynamics. In order to hydrophobically treat the TT-LGDLs, the fresh sample was rinsed in ethanol, and thoroughly dried, and then placed in a 1 mM solution of octadecyltrichlorosilane in toluene for 1 h. The reason we selected this molecule is because the trichlorosilane head group reacts well with many oxide surfaces, and the molecule has a long chain for good stability and excellent hydrophobicity. The thickness of this film was estimated to be about 2.5 nm, based on the structure of the monolayer, the number of carbons and associated bond lengths [48, 49]. The surface roughness should be negligible for the film itself, as n-alkyl trichlorosilanes are known to form dense monolayers on titanium [50]. Figure 15 schematically shows the structure of the monolayer as prepared from n-octadecyltrichlorosilane ($CH_3(CH_2)_{17}SiCl_3$; $C_{18}SiCl_3$). As established by Mani et

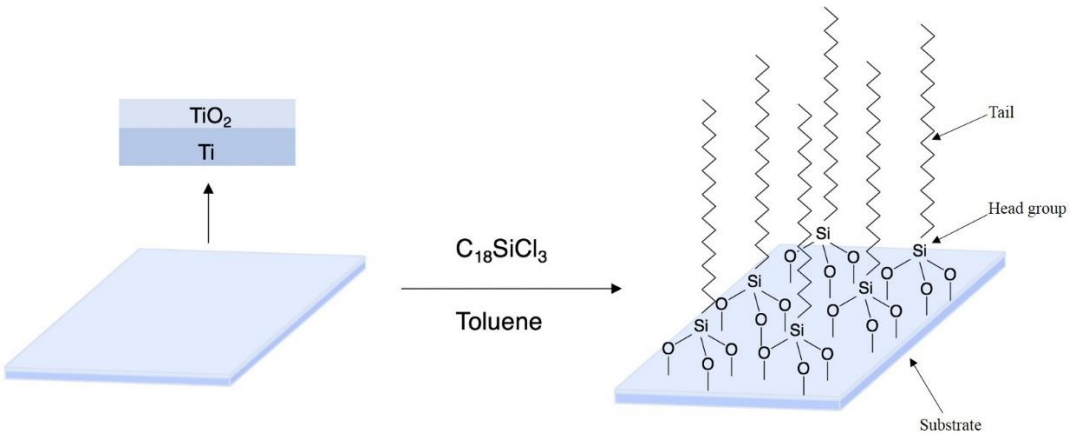

Figure 15. Schematic for the formation of a monolayer film from n-octadecyl trichlorosilane onto titanium.

al., the principal binding of the molecule to the oxide surface of titanium is through Si-O-Ti bonds with minimal Si-O-Si cross-linking, leading to a densely packed hydrocarbon film.

The specific, designed transparent cell, as shown in Figure 16, was used to test the PEMEC performance and to perform visualization of micro bubble dynamics and two-phase transport. Different from the typical PEMECs, the anode transparent PEMEC as shown in the red box, has an end plate with a window on the center, a transparent plate, a current distributor with flow channels, and TT-LGDLs, which help to allow optical access to the CL surface. The transparent plate with flow ports and in-flow channels is used to transport reactants from the cell inlet to the flow channels, and products from the flow

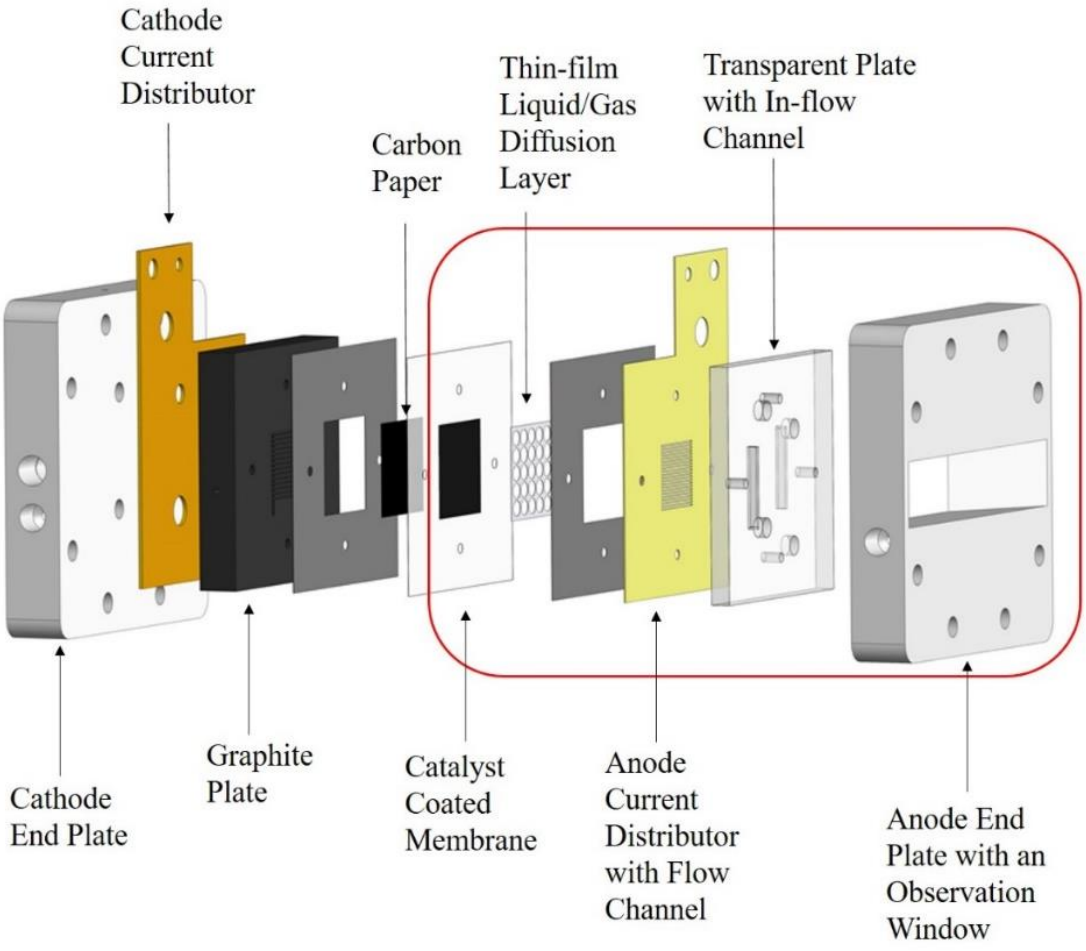

Figure 16. Schematic of the transparent PEMEC

channels to the outlet of the cell. The current distributor is a 500 mm thick titanium plate with chemically etched parallel micro flow channels of 1 mm in channel width that penetrated the entire thickness. TT-LGDLs with a thickness of only 25 μm are used. Since the oxygen bubble dynamics occur at the micro-scale at a super high-speed, the phenomena cannot be effectively captured by the normal microscopes or cameras. Therefore, besides the transparent cell and TT-LGDLs, the HMVS with a long-working distance is another critical part of the whole system. The HMVS consists of a high-speed camera (Phantom V711) coupled with an in-house built optical lens system featured by its long working distance (> 70 mm) and a high resolution (< 5 μm). The movie is captured under a frame rate of 3000 fps (frame per second), and the bubble detachment time within TT-LGDL were calculated based on the frame rate.

Commercial CCM (Nafion 115 Electrolyzer CCM from FuelCellsEtc with 3.0 mg/cm^2 IrRuOx at anode and 3.0 mg/cm^2 PtB at cathode) is employed, and the active area of the CCM is 5 cm^2. Carbon paper (Toray 090 from FuelCellStore) with a 280 μm thickness and 78% porosity is used as a cathode LGDL. Graphite plates with a parallel flow channel are used as cathode BP. The transparent cell is connected to the Potentiostat SP-300 (Bio-Logic) system that was equipped with a 10 A/5 V booster. A liquid pump (KNF Neuberger) is used to circulate deionized water at a flow rate of 20 mL/min to the anode.

The sessile drop method is used to measure the contact angle. The measured TT-LGDLs are placed on the top of a plastic substrate and a 2 μL droplet of distilled water is dropped from the tip to the surface of the TT-LGDLs, including the fresh and hydrophobic TT-

LGDLs. The image of the droplet is collected and the contact angle is measured in this image by the software. Three measurements at different spots are obtained for each sample and an average is calculated and reported as the contact angle.

3.5 Results and discussion

The treated TT-LGDL has a much higher contact angle (127°) than the untreated one (86°) due to the presence of the dense, low-energy methyl-terminated monolayer that effectively screens the interaction between water and titanium, as shown in Figure 17. These results show that the monolayer treatment can significantly change the wettability of the TT-LGDLs. As a control, we also prepared silane monolayers on non-porous titanium foils. As with the LGDLs, the presence of the monolayer increases the water contact angle—in this case, from 68° to 110°. The value of 110° is consistent with that of a smooth and dense methyl surface and is similar to the values reported by Mani et al. for silane monolayers on titanium. The water contact angles on the LGDL are elevated from those on the Ti foil due to the imparted roughness of the LGDL, which may stabilize air under the water drop and at the three-phase contact line.

Both the hydrophobic and hydrophilic TT-LGDLs were evaluated in the transparent PEMEC at 80 $^{\circ}$C. Because the transparent plate is made of plastic and the current distributor is relative thin, which may cause a non-uniform pressure distribution along the surface and thus a larger ohmic loss than that of the conventional PEMECs. The EIS result at 0.1A/cm^2

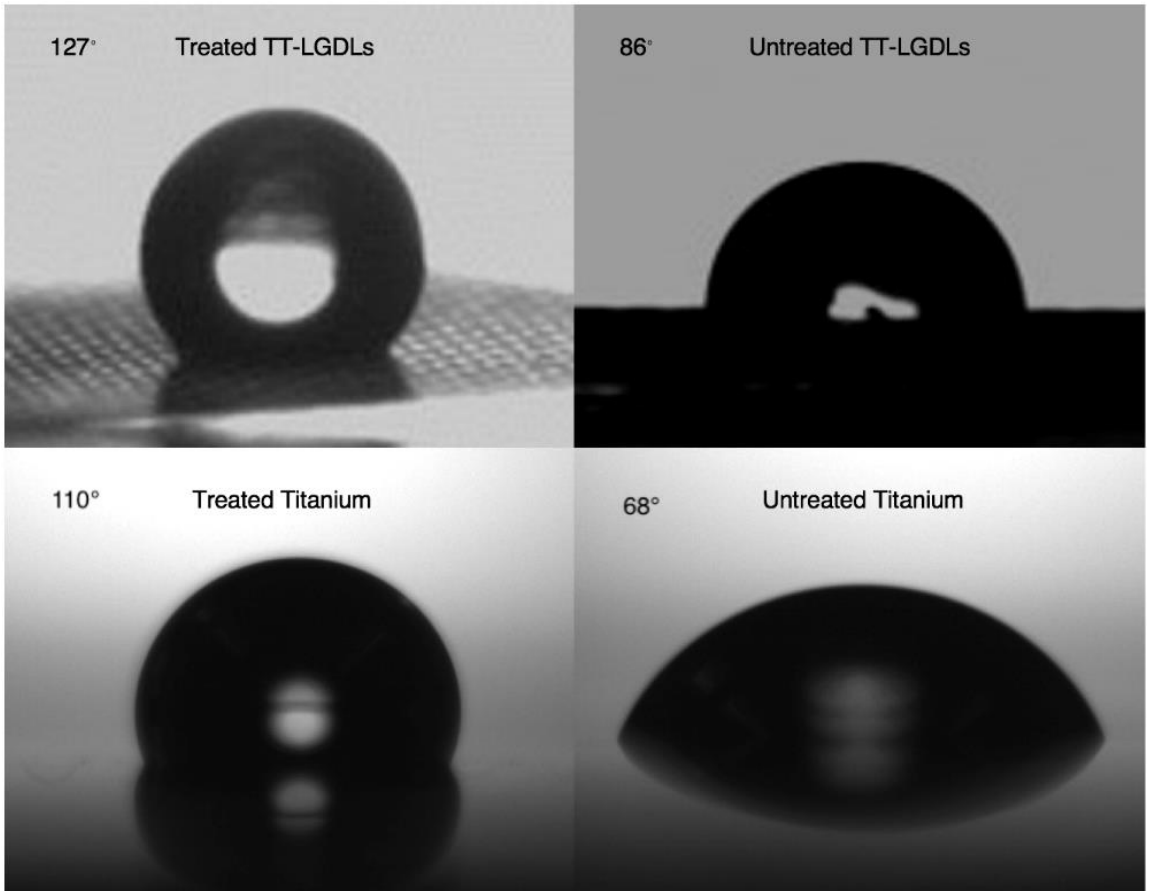

Figure 17. Contact angle measurements for (top) treated and untreated TT LGDLs and (bottom) treated and untreated Ti foil.

give the high frequency resistance (HFR) values for the treated TT-LGDL is 0.24 ohm*cm^2, and 0.22 ohm*cm^2 for the non-treated one. The result shows that the SAM can lead to a slightly increased HFR (the larger ohmic loss). However, the difference is small, and can be neglected. The performance of the PEMECs is characterized by the IR-free voltage, which is derived based on polarization curves and high frequency resistance (HFR), as shown in Figure 18. The lower voltage at a given current density indicates better PEMEC performance. As is shown in Figure 18, the performance of the hydrophobic TT-LGDLs is a little bit worse than the hydrophilic one. At the low current density range (< 0.1 A/cm^2), the polarization curves are mainly due to the open circuit voltage (OCV) and activation overpotential. From Figure 18, the hydrophobic and the hydrophilic TT-LGDLs have a similar voltage, which means the wettability of the TT-LGDLs has no impact on activation loss. At 2.0 A/cm^2, the required cell voltage increased from 1.620 V for the hydrophilic TT-LGDLs to about 1.624 V for the hydrophobic TT-LGDLs which indicates that the wettability of the TT-LGDLs has very limited impact on PEMEC performance. With a 2.5 nm thickness, it can be assumed that the monolayer film will not affect the electrical conductivity of the TT-LGDLs as long as the temperature is in a range from 20 °C to 80 °C, and also the electrical contact resistance between TT-LGDLs/CLs and TT-LGDLs/BPs [18, 51]. In addition, the monolayer does not change the pore morphologies of the TT-LGDLs, which will not influence the activation loss. The monolayer on TT-LGDLs will only change the wettability of the Ti TT-LGDLs from 86 ^{o} to 127 ^{o}, which may have some effects on transport loss in the PEMEC. Therefore, the influence of the

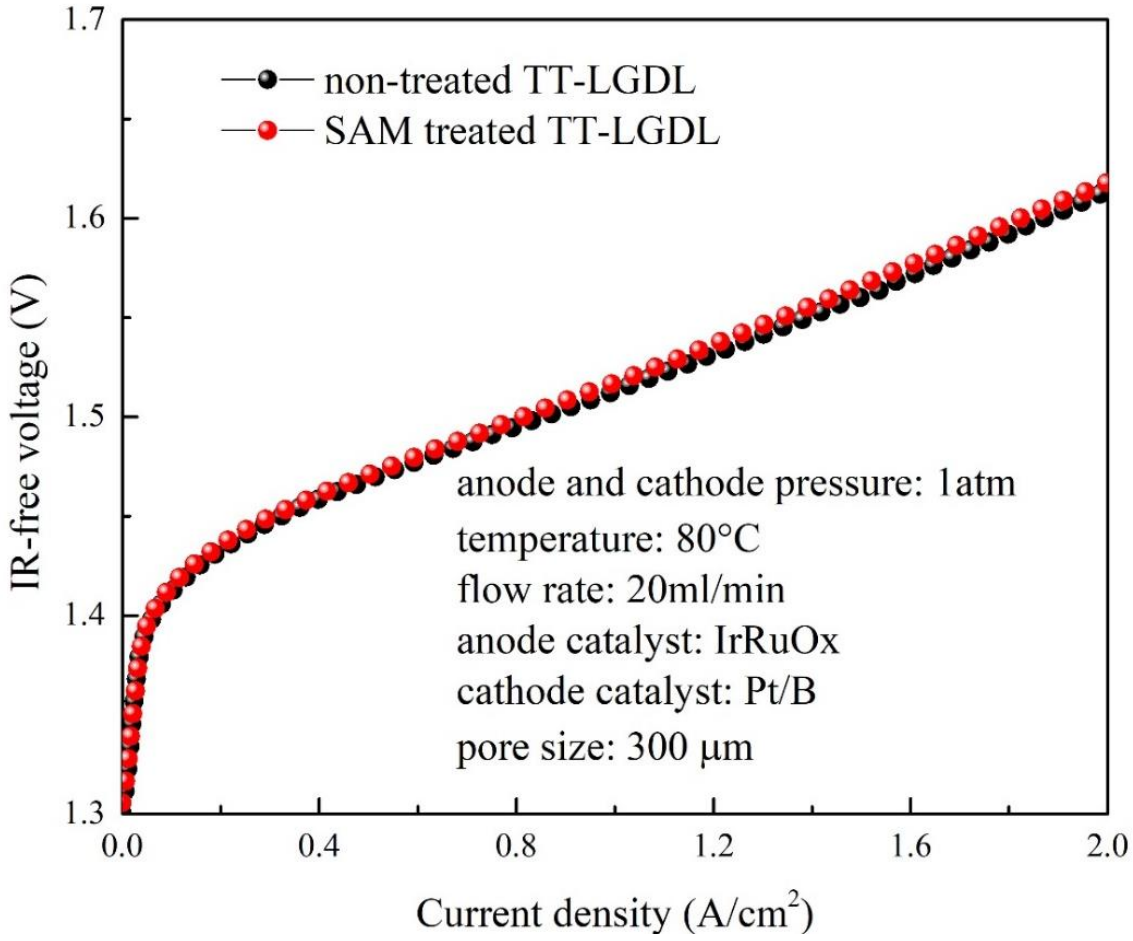

Figure 18. The polarization curves of the hydrophobic and hydrophilic TT-LGDLs.

monolayer on bubble dynamics, and two-phase transport will be investigated.

Figure 19 shows the two-phase flow phenomena comparison at channel-scale, Figures 19(A) and (B) are bubble dynamics at 0.2 A/cm^2, 80ºC, Figures 19(C) and (D) are bubble dynamics at 1.4 A/cm^2, 80ºC. It can be found that the most oxygen bubbles in the channel with the hydrophobic TT-LGDLs are much larger (as shown in Figure 19(A) and 19(C)) than the bubble sizes with the hydrophilic TT-LGDLs (as shown in Figure 19(B) and 19(D)). After the bubble detachment, some bubbles will collide and then merge with each other to form a large bubble. Under the same operating conditions, the larger bubbles with higher surface area and large volume have higher probability to merge with other bubbles; therefore, the hydrophobic TT-LGDLs with larger detached oxygen bubbles can lead to larger bubble sizes within the flow channel than those observed for the hydrophilic TT-LGDLs. These phenomena are very common in the whole channel in the PEMECs.

Figure 20 shows a sequence of images of pore-scale bubble generation and movement, with photographs of an oxygen gas bubble appearance, growth, and finally, detachment. The bubble dynamics are different for different locations, due to the different force balance in the water flow. Therefore, the oxygen bubbles we chose with the two different TT-LGDLs are nearly at the same location in the cell and pore. Figure 20 (A) to (D) and (E) to (H) show the oxygen bubble generation and growth with hydrophilic and hydrophobic TT-LGDLs at 0.2 A/cm^2 and 80°C, respectively. Figure 6 shows that the oxygen bubbles only generate at the rim of the TT-LGDL pores, which is the same phenomena as compared to our previous research and can be attributed to the large in-plane electrical resistance of

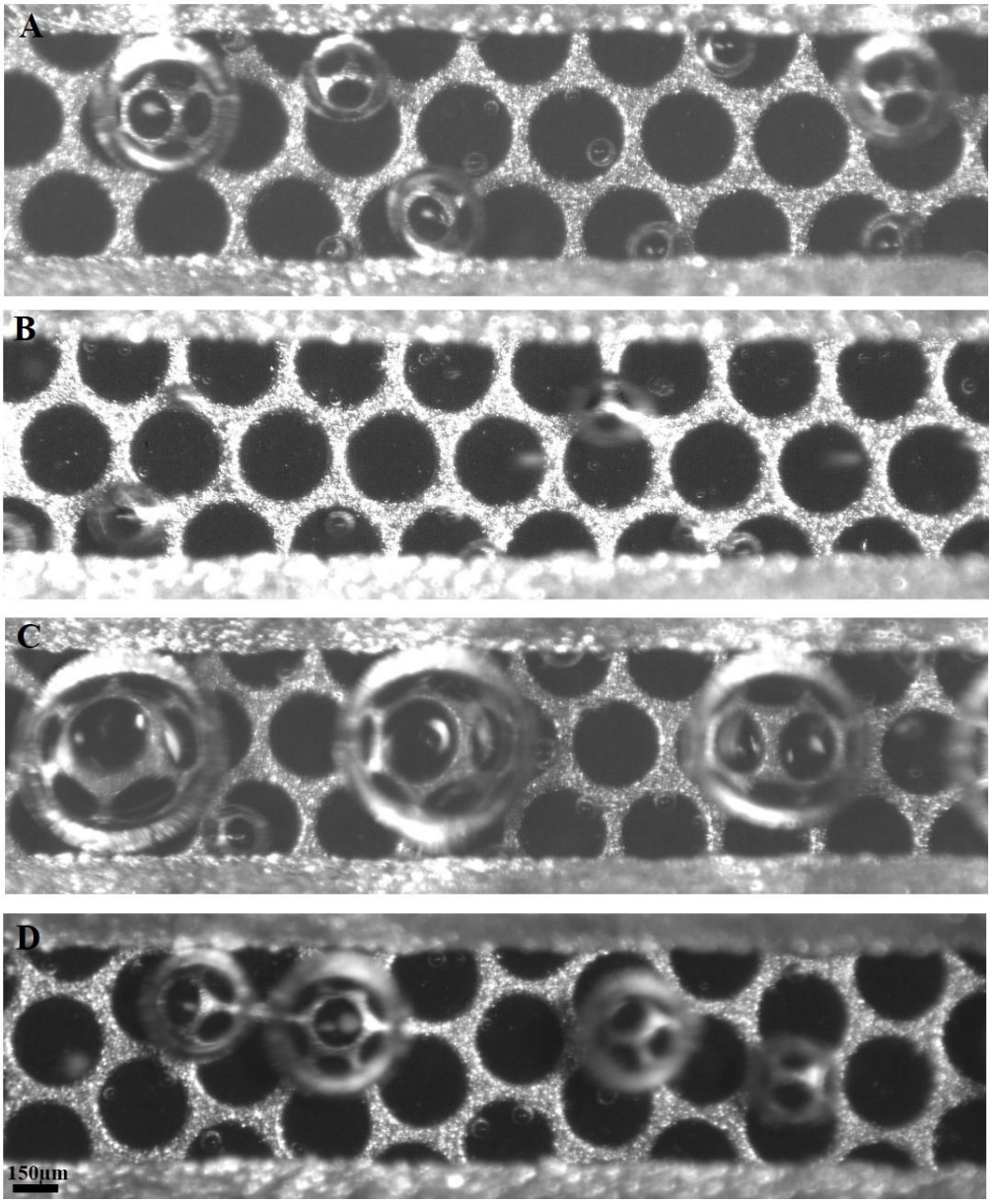

Figure 19. The visualization results at channel scale: (A) hydrophobic TT-LGDLs and (B) hydrophilic TT-LGDLs at 0.2 A/cm^2 and 80°; (C) hydrophobic TT-LGDLs and (D) hydrophilic TT-LGDLs at 1.4 A/cm^2 and 80°C.

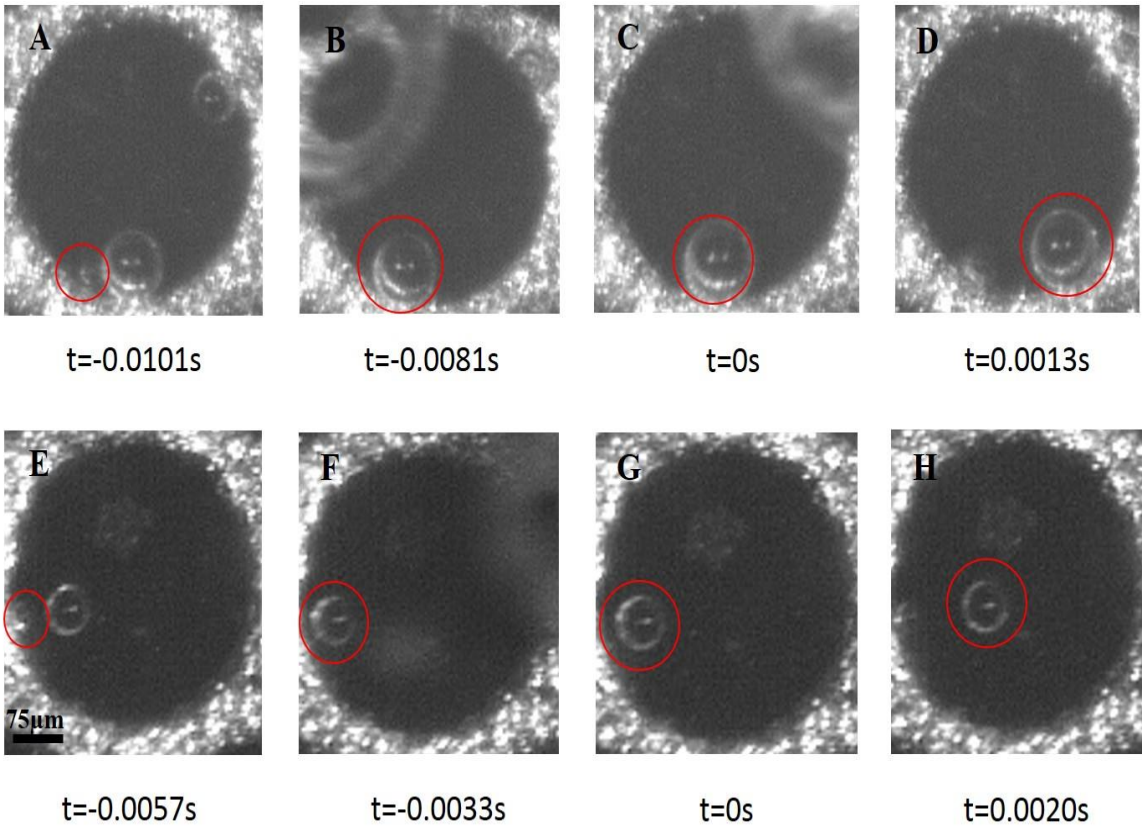

Figure 20. The visualization results of pore scale (A) to (D) hydrophobic TT-LGDLs and (E) to (H) hydrophilic TT-LGDLs at 0.2 A/cm^2 and 80°C.

the CLs [52]. The oxygen bubble will appear at the rim of the pore, then it will grow and detach within a couple of milliseconds. Figure 20 (C) and (G) show the bubble detachment from the surface of the two TT-LGDLs. The bubble detachment diameter for the hydrophilic TT-LGDLs (about 57 μm) is smaller than the hydrophobic one (about 84 μm). Also, the bubble detachment time for the hydrophilic TT-LGDLs (about 0.0057 s) is shorter than the hydrophobic one (about 0.0101 s). The reason is that bubbles are prone to attach on the hydrophobic surface of the treated TT-LGDL (contact angle$>$ 90°), and easily to detach from a hydrophilic TT-LGDL (contact angle$<$ 90°). Moreover, this successive bubble behavior occurs in a repetitive manner at the same points. Considering the PEMEC performance shown in Figure 18, we conclude that the hydrophobic treatment on TT-LGDLs has a negative impact on bubble detachment, which could increase the transport loss in the PEMEC, but this result has limited effect on PEMEC performance under 2.0 A/cm^2. Because the advantages of the TT-LGDLs, such as planar surfaces, straight-through pores, and small thickness, the transport losses will be limited. Although the monolayer film will increase the bubble detachment diameter and bubble size in the channels, the increase of transport loss due to these reasons is very small compared with the total loss in the PEMEC. Considering that the monolayer film has no effect on ohmic and activation losses, it will not have significant influence on PEMEC performance, especially under 2.0 A/cm^2. We expect that the performance of the hydrophobic TT-LGDLs will be degraded under much higher current densities due to the large bubble detachment, which may cause additional two-phase transport losses in a PEMEC.

3.6 Conclusions

In this study, the hydrophilic titanium TT-LGDLs are treated by a silane monolayer to change their wettabilities for the first time. The micro-scale and ultra-fast oxygen bubble dynamics are in-situ visualized in a novel designed transparent PEMEC with a HMVS. The results show that the oxygen bubble detachment diameter and frequency of the hydrophobic TT-LGDLs are much larger than ones with the hydrophilic TT-LGDLs, and the bubble size in the channel scale with the hydrophobic TT-LGDLs is much larger than the one with the hydrophilic TT-LGDLs as well. The PEMEC performance with the hydrophobic and hydrophilic TT-LGDLs are very close. The advantages of the TT-LGDLs, such as planar surface, straight-through pores, and small thickness result in very limited difference of the transport losses between the hydrophobic and hydrophilic TT-LGDLs. The increase of the transport loss due to these reasons is very small compared with the total loss in the PEMEC, especially under 2.0 A/cm^2. We expect that the performance of the hydrophobic TT-LGDLs will be degraded under much higher current densities, due to the large bubble detachment which may cause additional two-phase transport losses in a PEMEC.

References

1. Turner, J.A., Sustainable hydrogen production. Science, 2004. 305(5686): p. 972-974.
2. Ito, H., et al., Experimental study on porous current collectors of PEM electrolyzers. International journal of hydrogen energy, 2012. 37(9): p. 7418-7428.
3. Yoshida, T. and K. Kojima, Toyota MIRAI fuel cell vehicle and progress toward a future hydrogen society. The Electrochemical Society Interface, 2015. 24(2): p. 45-49.
4. Rostrup-Nielsen, J.R., Making fuels from biomass. Science, 2005. 308(5727): p. 1421-1422.
5. Ayers, K.E., et al., Research advances towards low cost, high efficiency PEM electrolysis. ECS Transactions, 2010. 33(1): p. 3-15.
6. Lin, J.H., et al., Effect of various hydrophobic concentrations and base weights of gas diffusion layer for proton exchange membrane fuel cells. Fuel Cells, 2010. 10(1): p. 118-123.
7. Kang, Z., et al., Investigation of thin/well-tunable liquid/gas diffusion layers exhibiting superior multifunctional performance in low-temperature electrolytic water splitting. Energy & Environmental Science, 2017. 10(1): p. 166-175.
8. Yang, G., et al., Additive manufactured bipolar plate for high-efficiency hydrogen production in proton exchange membrane electrolyzer cells. International Journal of Hydrogen Energy, 2017. 42(21): p. 14734-14740.

9. Mo, J., et al., Additive manufacturing of liquid/gas diffusion layers for low-cost and high-efficiency hydrogen production. International Journal of Hydrogen Energy, 2016. 41(4): p. 3128-3135.
10. Mo, J., et al. Visualization on rapid and micro-scale dynamics of oxygen bubble evolution in PEMECs. in Nano/Micro Engineered and Molecular Systems (NEMS), 2017 IEEE 12th International Conference on. 2017. IEEE.
11. Lamy, C., et al., Clean hydrogen generation through the electrocatalytic oxidation of ethanol in a Proton Exchange Membrane Electrolysis Cell (PEMEC): Effect of the nature and structure of the catalytic anode. Journal of Power Sources, 2014. 245: p. 927-936.
12. Lamy, C., et al., Kinetics analysis of the electrocatalytic oxidation of methanol inside a DMFC working as a PEM electrolysis cell (PEMEC) to generate clean hydrogen. Electrochimica Acta, 2015. 177: p. 352-358.
13. Mo, J., et al. Investigation of titanium felt transport parameters for energy storage and hydrogen/oxygen production. in 13th International Energy Conversion Engineering Conference. 2015.
14. Mo, J., S. Steen, and F.-Y. Zhang. High-speed and micro-scale measurements of flow and reaction dynamics for sustainable energy storage. in 13th International Energy Conversion Engineering Conference. 2015.
15. Mo, J., et al., Discovery of true electrochemical reactions for ultrahigh catalyst mass activity in water splitting. Science Advances, 2016. 2(11): p. e1600690.

16. Toops, T.J., et al., Evaluation of Nitrided Titanium separator plates for proton exchange membrane electrolyzer cells. Journal of Power Sources, 2014. 272 (2014) 954-960.

17. Mo, J., et al., Electrochemical investigation of stainless steel corrosion in a proton exchange membrane electrolyzer cell. International Journal of Hydrogen Energy, 2015. 40(36): p. 12506-12511.

18. Han, B., et al., Effects of membrane electrode assembly properties on two-phase transport and performance in proton exchange membrane electrolyzer cells. Electrochimica Acta, 2016. 188: p. 317-326.

19. Han, B., et al., Modeling of two-phase transport in proton exchange membrane electrolyzer cells for hydrogen energy. International Journal of Hydrogen Energy, 2017. 42(7): p. 4478-4489.

20. Kang, Z., et al., Thin film surface modifications of thin/tunable liquid/gas diffusion layers for high-efficiency proton exchange membrane electrolyzer cells. Applied Energy, 2017. 206: p. 983-990.

21. Omrani, R. and B. Shabani, Gas diffusion layer modifications and treatments for improving the performance of proton exchange membrane fuel cells and electrolysers: A review. International Journal of Hydrogen Energy, 2017.

22. Zhang, F.-Y., S.G. Advani, and A.K. Prasad, Performance of a metallic gas diffusion layer for PEM fuel cells. Journal of power sources, 2008. 176(1): p. 293-298.

23. Zhang, F.-Y., A.K. Prasad, and S.G. Advani, Investigation of a copper etching technique to fabricate metallic gas diffusion media. Journal of Micromechanics and Microengineering, 2006. 16(11): p. N23.

24. Matar, S. and H. Liu, Effect of cathode catalyst layer thickness on methanol cross-over in a DMFC. Electrochimica Acta, 2010. 56(1): p. 600-606.

25. You, L. and H. Liu, A parametric study of the cathode catalyst layer of PEM fuel cells using a pseudo-homogeneous model. International Journal of Hydrogen Energy, 2001. 26(9): p. 991-999.

26. Natarajan, D. and T. Van Nguyen, Three-dimensional effects of liquid water flooding in the cathode of a PEM fuel cell. Journal of power sources, 2003. 115(1): p. 66-80.

27. Stampino, P., et al., Effect of different hydrophobic agents onto the surface of gas diffusion layers for PEM-FC. CHEMICAL ENGINEERING, 2013. 32.

28. Thomas, Y.R., et al., New method for super hydrophobic treatment of gas diffusion layers for proton exchange membrane fuel cells using electrochemical reduction of diazonium salts. ACS applied materials & interfaces, 2015. 7(27): p. 15068-15077.

29. Ko, T.-J., et al., High performance gas diffusion layer with hydrophobic nanolayer under a supersaturated operation condition for fuel cells. ACS applied materials & interfaces, 2015. 7(9): p. 5506-5513.

30. Kim, S., et al., Effects of hydrophobic agent content in macro-porous substrates on the fracture behavior of the gas diffusion layer for proton exchange membrane fuel cells. Journal of Power Sources, 2014. 270: p. 342-348.

31. Zhang, F.Y., et al., In situ characterization of the catalyst layer in a polymer electrolyte membrane fuel cell. Journal of the Electrochemical Society, 2007. 154(11): p. B1152-B1157.

32. Zhang, F.Y., X.G. Yang, and C.Y. Wang, Liquid water removal from a polymer electrolyte fuel cell. Journal of the Electrochemical Society, 2006. 153(2): p. A225-A232.

33. Yang, X.G., et al., Visualization of liquid water transport in a PEFC. Electrochemical and Solid State Letters, 2004. 7(11): p. A408-A411.

34. Mortazavi, M. and K. Tajiri, Effect of the PTFE content in the gas diffusion layer on water transport in polymer electrolyte fuel cells (PEFCs). Journal of Power Sources, 2014. 245: p. 236-244.

35. Mortazavi, M. and K. Tajiri, Liquid water breakthrough pressure through gas diffusion layer of proton exchange membrane fuel cell. international journal of hydrogen energy, 2014. 39(17): p. 9409-9419.

36. Koresawa, R. and Y. Utaka, Improvement of oxygen diffusion characteristic in gas diffusion layer with planar-distributed wettability for polymer electrolyte fuel cell. Journal of Power Sources, 2014. 271: p. 16-24.

37. Lim, C. and C. Wang, Effects of hydrophobic polymer content in GDL on power performance of a PEM fuel cell. Electrochimica Acta, 2004. 49(24): p. 4149-4156.

38. Litster, S., D. Sinton, and N. Djilali, Ex situ visualization of liquid water transport in PEM fuel cell gas diffusion layers. Journal of Power Sources, 2006. 154(1): p. 95-105.

39. Pasaogullari, U. and C. Wang, Liquid water transport in gas diffusion layer of polymer electrolyte fuel cells. Journal of the electrochemical society, 2004. 151(3): p. A399-A406.

40. Ioroi, T., et al., Influence of PTFE coating on gas diffusion backing for unitized regenerative polymer electrolyte fuel cells. Journal of power sources, 2003. 124(2): p. 385-389.

41. Hwang, C.-M., et al., Effect of PTFE contents in the gas diffusion layers of polymer electrolyte-based unitized reversible fuel cells. Journal of International Council on Electrical Engineering, 2012. 2(2): p. 171-177.

42. Hwang, C.M., et al., Influence of properties of gas diffusion layers on the performance of polymer electrolyte-based unitized reversible fuel cells. International journal of hydrogen energy, 2011. 36(2): p. 1740-1753.

43. Hwang, C., et al., Effect of through-plane polytetrafluoroethylene distribution in a gas diffusion layer on a polymer electrolyte unitized reversible fuel cell. ECS Transactions, 2013. 58(1): p. 1059-1068.

44. Kang, Z., et al., Novel Thin/Tunable Gas Diffusion Electrodes with Ultra-Low Catalyst Loading for Hydrogen Evolution Reactions in Proton Exchange Membrane Electrolyzer Cells. Nano Energy, 2018.

45. Mo, J., et al., Thin liquid/gas diffusion layers for high-efficiency hydrogen production from water splitting. Applied Energy, 2016. 177: p. 817-822.

46. Kang, Z., et al. Investigation of Novel Thin LGDLs for High-Efficiency Hydrogen/Oxygen Generation and Energy Storage. in 15th International Energy Conversion Engineering Conference. 2017.

47. Li, Y., et al., In-situ investigation of bubble dynamics and two-phase flow in proton exchange membrane electrolyzer cells. International Journal of Hydrogen Energy, 2018.

48. Acton, O., et al., Spin‐Cast and Patterned Organophosphonate Self‐Assembled Monolayer Dielectrics on Metal‐Oxide‐Activated Si. Advanced Materials, 2011. 23(16): p. 1899-1902.

49. Halik, M., et al., Low-voltage organic transistors with an amorphous molecular gate dielectric. Nature, 2004. 431(7011): p. 963.

50. Mani, G., et al., Stability of self-assembled monolayers on titanium and gold. Langmuir, 2008. 24(13): p. 6774-6784.

51. Yang, G., et al., Fully printed and integrated electrolyzer cells with additive manufacturing for high-efficiency water splitting. Applied Energy, 2018. 215: p. 202-210.

52. Kang, Z., et al., Performance Modeling and Current Mapping of Proton Exchange Membrane Electrolyzer Cells with Novel Thin/Tunable Liquid/Gas Diffusion Layers. Electrochimica Acta, 2017. 255: p. 405-416.

CHAPTER IV

DIRECT THERMAL VISUALIZATION OF MICRO-SCALE HYDROGEN EVOLUTION REACTIONS IN PROTON EXCHANGE MEMBRANE ELECTROLYZER CELLS

A version of this chapter was originally published by Yifan Li:

Yifan Li, Gaoqiang Yang, Shule Yu, Zhenye Kang, Derrick A. Talley, Feng-Yuan Zhang. "Direct thermal visualization of micro-scale hydrogen evolution reactions in proton exchange membrane electrolyzer cells." *Journal of energy conversion and management* 396 (2019): 590-598.

I am fully responsible for the work submitted in these publications.

4.1 Abstract

This study investigates the correlation between the temperature variance and hydrogen evolution reaction (HER) on the cathode side of a proton exchange membrane electrolyzer cell (PEMEC). A series of *in-situ* experiments are conducted with the help of a novel PEMEC design, thermal spectroscopy and a high-speed visualization system. At channel-scale, the temperature increases rapidly from room temperature (19 °C) to the equilibrium state (27 °C), with an operating current density of 0.5 A/cm^2. The temperature distribution is non-uniform throughout the process. A series of pore-scale analyses are carried out to clarify the relationship between temperature distribution and electrochemical reaction area. Interestingly, the areas of rapid heat generation are found to be in good agreement with the areas pf electrochemical reaction, which confirms that heat is released during the reaction processe. Finally, the temperature evolution phenomena on the liquid gas diffusion layer (LGDL) surface have also been recorded. These findings can aid understanding of the correlation between cathode side electrochemical reaction and heat generation.

4.2 Highlights

- A novel PEMEC for direct thermal investigation is developed.
- Thermal dynamics of hydrogen evolution reactions are *in-situ* visualized.
- Temperature distribution is not uniform in the cathode side channel.
- Electrochemical reactions are visualized and showed a good coincident with the thermal results.
- Temperature increase phenomena on the LGDL are captured.

4.3 Introduction

Hydrogen is regarded as an environmentally friendly source of energy, and has attracted interest in the search for a sustainable society [1-5]. Water electrolysis is considered a relatively safe method for hydrogen and oxygen production with high purity, and in particular, it has been extensively researched and applied to many areas, including the aerospace sector, the military, and industry [6-9]. Proton Exchange Membrane Electrolyzer Cells (PEMECs) are one of the most effective ways to electrolyze water while minimizing environmental damage [10, 11]. They can also be widely used in large-scale applications. Compared with alkaline electrolyzer cells (AECs), PEMECs have the potential for higher performance and shorter startup time [12]. In general, the working principle of a PEMEC can be regarded as the reverse of that of a fuel cell [13]. When a PEMEC is operating,

deionized water (DI water) continuously transports to the anode side. When the water reaches the interface between the well-tunable liquid/gas diffusion layer (LGDL) and the catalyst layer, it react with the help of the catalyst and is split into oxygen, protons, and electrons. The electrons and oxygen are transferred out of the cell, the protons are transferred from the anode side to the cathode side, and the electrons (from the outside) immediately combine with the protons to form hydrogen, thereby releasing heat [14]. Hydrogen will subsequently transfer out of the cell. Previous research has explored several ways to better understand the mechanism of PEMECs. Those researches are mainly focused on the two-phase flow and bubble dynamics during the electrochemical reaction in order to achieve higher efficiency and lower costs [15-20]. The electrochemical reactions on the cathode side and the thermal effect of PEMECs are the main objectives of this study. The overall reactions with the enthalpies of a PEMEC can be represented by Equation (1) [21]:

$$2H_2O + \overbrace{237.2\ \text{kJ mol}^{-1}}^{\text{Electricity}} + \overbrace{48.6\ \text{kJ mol}^{-1}}^{\text{Heat}} \xrightarrow{\text{Catalyst}} 2H_2 + O_2 \quad (1)$$

The maximum electrical work of the cell is 237.23 kJ/mol. The net heat absorption is 48.6 kJ/mol.

Thermal dynamics are the key issues in PEMEC design, and the underlying heat and mass transport processes are coupled [22, 23]. More importantly, thermal and electrochemical reactions in a PEMEC are closely interlinked, and cell performance cannot be studied without considering heat transfer and bubble dynamics. Thus, many studies have investigated temperature distribution within a proton exchange membrane fuel cell

(PEMFC). For example, Dutta et al. built a mathematical model to simulate heat transfer and water phase change in a PEM fuel cell [24]. The results showed that the temperature rise inside the model could have a great impact on the performance of a fuel cell. Wilkinson et al. found that the local temperature in a PEMFC at certain operating conditions demonstrated good agreement with the values of local current densities [25].

Many researchers have also focused on the temperature distribution on the anode side, bubble generation, and water transport in a PEMEC. For example, Mo et al. investigated bubble generation in a PEMEC and found that bubbles are generated only at the edge of a pore on the titanium thin-LGDL (TT-LGDL) [26, 27]. Bubble generation also occurred exclusively at the triple phase boundary (a place with electrons, catalysts, pathways for products or reactants, and proton carriers). Furthermore, Ito et al. visualized and investigated the bubble detachment diameter and detachment frequency at different working conditions, they found the operating flow rate and pressure could cause a significant impact on the detachment frequency, but a small impact on the detachment diameter [28].

Other studies have examined the heat transfer problem in other applications [29-38]. However, they were mainly focused on the temperature distribution and heat generation in a fuel cell or bubble and flow dynamics in an electrolyzer cell. Thus, the temperature distribution and water accumulation on the cathode side of a PEMEC have not been thoroughly studied and are not fully understood. A comprehensive analysis should be

conducted in order to ascertain the changes in temperature, two-phase flow, and bubble dynamics on the cathode side active area.

In this paper, a new method was proposed to investigate the cathode side of a PEMEC with the support of two different high-speed and micro-scale visualization systems (HMVSs). A comprehensive visualization experiment was conducted by using a thermal imaging camera and a high-speed visualization system. The variations in temperature and the hydrogen gas bubble generation on the cathode side of a PEMEC were captured. It was demonstrated that temperature distribution is not uniform throughout the whole surface of the catalyst layer on the cathode side. Furthermore, the variation in temperature at the pore scale was captured for the first time. A correlation was identified between the electrochemical reaction and the temperature distribution. It was found that the electrochemical reaction occurring at the cathode side causes the temperature to rise in a certain place (this place can be used to distinguish between the reaction and non-reaction areas). Finally, these findings could serve as a foundation for the further examination of the electrochemical reaction, and provide a new method that can be used in future studies.

4.4 Experimental details

For the test cell (Fig. 21), the two end plates were made from commercial aluminum with an observation window opened in the cathode side end plate. The current distributor on the cathode side was made of Titanium (Ti) with 10 parallel flow channels, and worked as a bipolar plate to transfer electrons and heat. The well-tunable LGDL on the cathode side

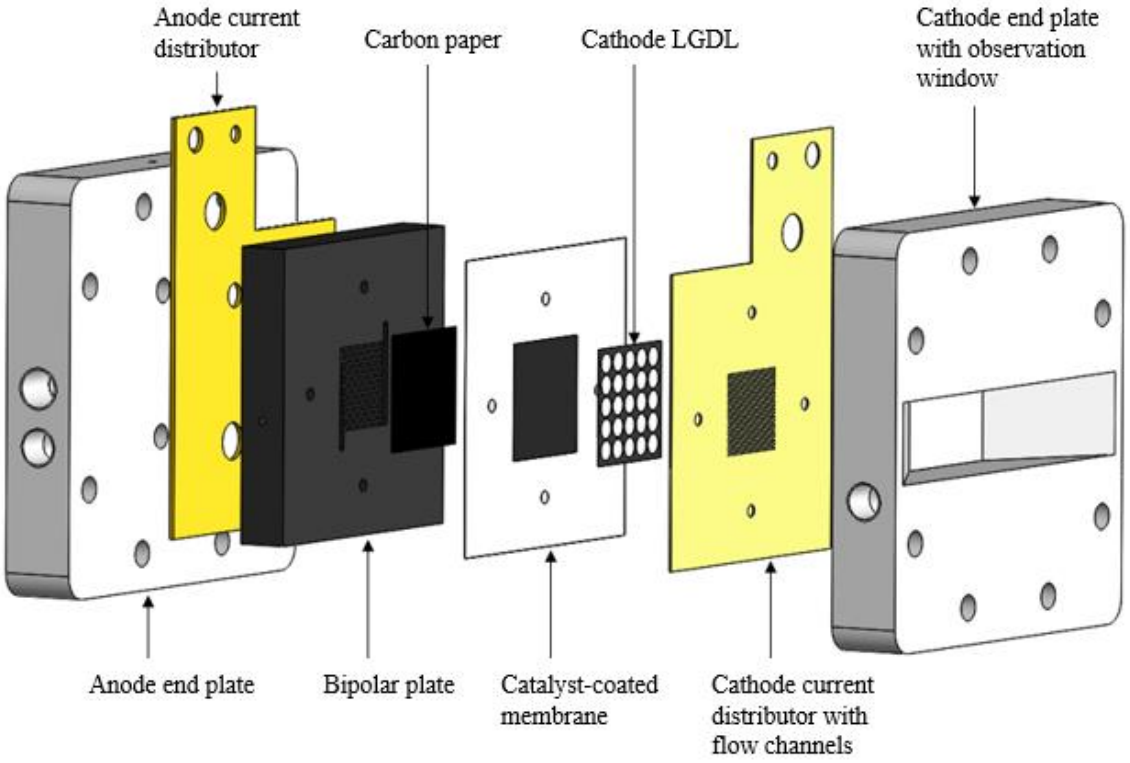

Figure 21. Schematic of the specific PEMEC for cathode side thermal and bubble analysis.

was also made of Ti, which serves as an electron conductor with little resistance. The anode LGDL was Toray 090 carbon paper. A commercial catalystcoated membrane (CCM) was made from Nafion 115 (EZ-CCM; FuelCellsEtc) with a thickness of 125 μm. The catalyst was 3.0 mg/cm^2 $IrRuO_x$ on the anode side, and 3.0 mg/cm^2 Pt black on the cathode side. The active area of the CCM was 5 cm^2. The PEMEC was connected with a Potentiostat station (Biologic SP-300) with electrochemical analysis software from Bio-Logic, which provided a current range of up to 10 A, and a voltage range of up to 5 V, in order to test performance. The input current density was 0.5 A/cm^2 and was controlled by the EC-Lab platform. The diameter of each pore on the LGDL was 300 μm, and the LGDL and catalyst layer were directly visualized by a visualization system. A water pump provided a flow rate of 10 mL/min.

The FLIR SC6700 longwave infrared camera is a high-speed thermal imaging camera that measures the radiant thermal energy distribution (heat) emitted from an object's surface [39, 40]. For the experiment, the distance between the lens and the experimental target was 0.2 m, and the frame rate was 123 fps. The working temperature applied was room temperature (19 °C), the working pressure was atmospheric pressure and the transmissivity of the lens was assumed to be 1.0.

Furthermore, a High-speed, Micro-scale Visualization System (HMVS) was introduced to capture the generation of hydrogen bubbles on the cathode side. This system includes two components: first, a high-speed Phantom v711 camera that can operate at 1,400,000 fps (the fastest speed with a reduced resolution); second, a long-distance microscope

system that includes a micro-scale lens assembly and a zoom lens body that can provide a long working distance (> 70 mm). The recording frame rate in this study was 3000 fps, at a resolution of 1280 × 800, which is sufficient to see the microscale bubbles. Prior to testing, channels on the cathode side were sprayed and filled with DI water, with no water movement. During the test, water was circulated on the anode side, while on the cathode side, the hydrogen bubbles generation phenomena was observed on the CCM, and captured by the HMVS.

4.5 Results and discussion

In this study, thermal and fluid dynamic analyses on the cathode side were conducted in a PEMEC with an active area of 5.0 cm^2. The calibration of the system, including measuring the working temperature and humidity, the reflected temperature, and adjusting the input emissivity was important. The accuracy of the emissivity has been regarded as a very important factor in this study, as emissivity can greatly influence the measured temperature values.

In general, the change in the temperature distribution of a PEMEC depends on the evolution of the hydrogen/oxygen reaction occurring at the cathode/anode, as well as the kinetics during the charge transfer. This study focused on the temperature variance and the hydrogen evolution reaction (HER) on the cathode side. During the operation, heat can be generated due to entropy changes and ohmic resistance, thereby leading to a temperature increase in the cathode [41]. In order to further understand this process, an experiment was

conducted to find the emissivity of the catalyst layer and the well-tunable LGDL. The experimental setup consisted of a Ti thin film LGDL and a CCM. Accurate emissivity values were obtained by performing the following steps: first, a piece of aluminum foil was crumpled, and placed in front of the target. Then, a picture was taken using the thermal camera, and the emissivity was set to 1. The reflected temperature was the temperature of the aluminum foil. Finally, the emissivity was determined using FLIR ResearchIR software so that the target temperature in the camera matched that of the room temperature (19 °C). The emissivity of Ti and Pt black were found to be approximately 0.91 and 0.19, respectively.

The surface of the CCM at pore scale was measured at two different temperatures, in order to evaluate the accuracy of the camera/detector and the calibration. The surface temperature at 19 °C is shown in Fig. 22A, which shows a constant temperature across the whole surface.

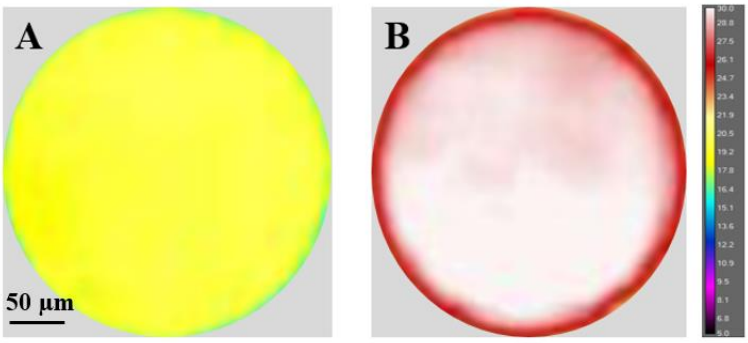

Figure 22. Photographs showing the surface temperature at (A) 19 °C, and (B) 30 °C.

When the cell was heated to 30 °C. As shown in Fig. 22B, the surface temperature captured by the thermal camera was also 30 °C. Therefore, it demonstrates that the thermal camera was able to accurately capture the temperature values and range in the videos and figures.

Preliminary experiments were conducted in the channel scale of a PEMEC to capture the variation in the temperature distribution on the cathode side. Although there were a total of 10 channels in the cell, only five channels were selected for this study due to the resolution limit (640 × 512) of the thermal camera. Figs. 23A-J show a sequence of time-progressing snapshot images of the variation in temperature distribution in the channel

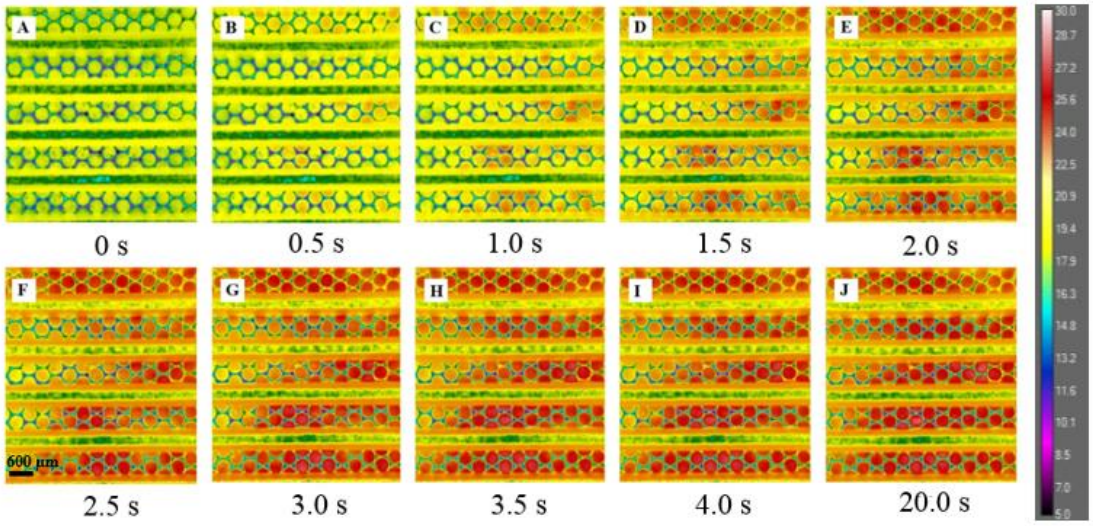

Figure 23. Sequence of photographs showing the evolution of temperature distribution at channel scale.

scale experiments, with an initial surface temperature of 19 °C. The temperature increased rapidly from 19 °C at 0 s to approximately 24.5 °C at 1.5 s for most pores. The rate of the temperature increase diminished after 1.5 s, until the distribution of the surface temperature became stable at 2.5 s, with an overall peak temperature of 27 °C. The net heat transfer rate was equal to 0 after 2.5 s, at which point the temperature distribution in the entire channel reached equilibrium (which is defined as a balanced state between heat generation and heat removal). The color difference between the catalyst layer and the LGDL can be attributed to the difference in emissivity.

An interesting phenomenon occurred during this process: the temperature varied from place to place throughout the channel. As shown in Fig. 23, the pores in channel #1 (at the top of the photograph) demonstrated relatively higher temperatures than other pores in each snapshot. In addition, several pores in the middle of channels #4 and #5 (at the bottom of the photograph) had higher temperatures than the other pores. Previous research has indicated that temperature distribution on the anode side heavily relies on the kinetics of the electrochemical reactions and charge transfer [41]. The bubble generation rate and site are different for different active areas. Some areas have more active electrochemical reactions than others [42]. Thus, the non-uniform temperature distribution in different pores can be attributed to electrochemical reactions.

Moreover, a rapid temperature increase from 22 to 27 °C in the middle of each pore was observed and was replicated in each test. This phenomenon can be attributed to the ohmic loss and electrochemical reaction that occurred on the cathode side, where protons

combined with electrons from the external circuit and catalyst to produce hydrogen gas. The cathode side electrochemical reaction was expected to release heat energy (exothermic process) [43-45]. Thereby causing the temperature to rise on the surface until it reached a certain peak value (27 °C), and finally became stable. Therefore, it was important to monitor multiple pores to investigate the relationship between the electrochemical reaction and the variation in temperature distribution.

In order to further investigate the reasons for the variation in temperature distribution across a channel, a series of pore scale experiments were conducted to visualize the temperature distribution across a single pore. Several pores were selected because the phenomena in those pores most commonly occurred in the channel. Fig. 24 shows the started to gradually increase on the right side of the pore, from about 19 °C at 0 s to 22.5 °C at 1.0 s. The average temperature increase rate was 3.5 °C/s from 0 to 1.0 s. The temperature continued to rise over the pore, and finally reached equilibrium state over the full surface of the catalyst layer at approximately 24 °C (at 2.5 s), with the rate of temperature increase changing from 3.5 to 1.0 °C/s, and then continuously decreasing until reaching the equilibrium state with no more temperature change.

For comparison, experiments were conducted for other pores at the same conditions. Fig. 25 shows the temperature distribution in three different pores at 0.7 s, and it was seen that the temperature profiles on the catalyst layer were different for different cases. The rise in temperature within the two pores shown in Fig. 25A and 25B was small, in the range of

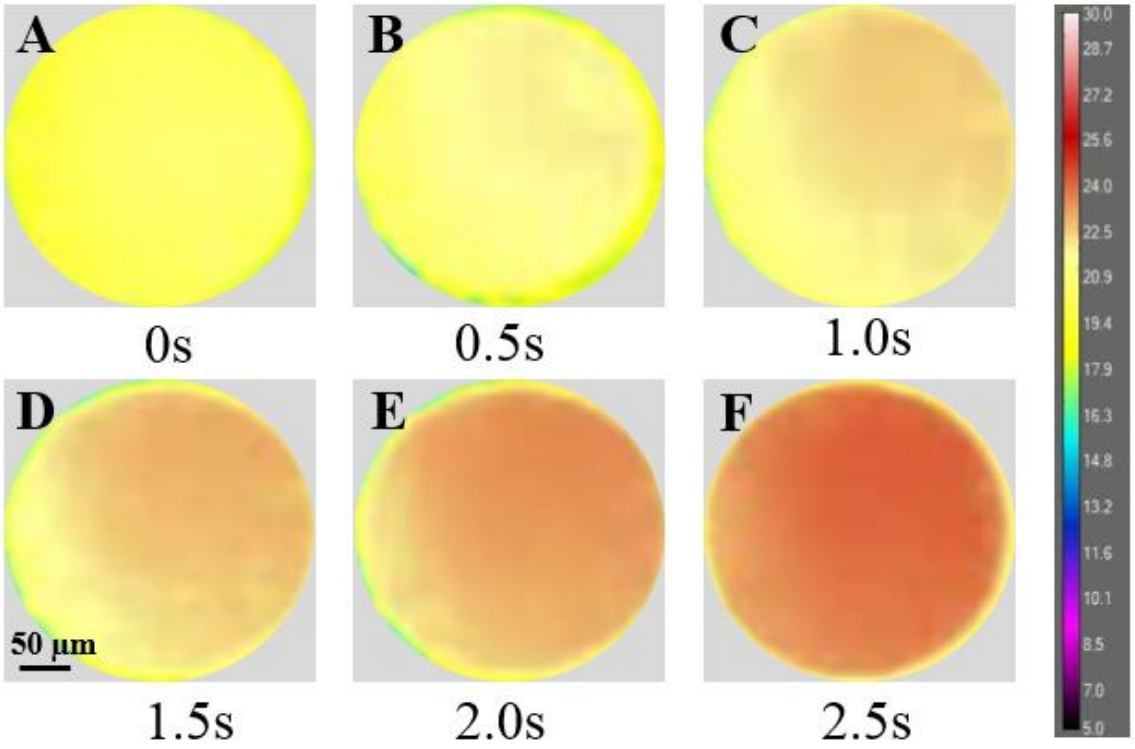

Figure 24. Sequence of photographs showing the evolution of temperature distribution at pore scale.

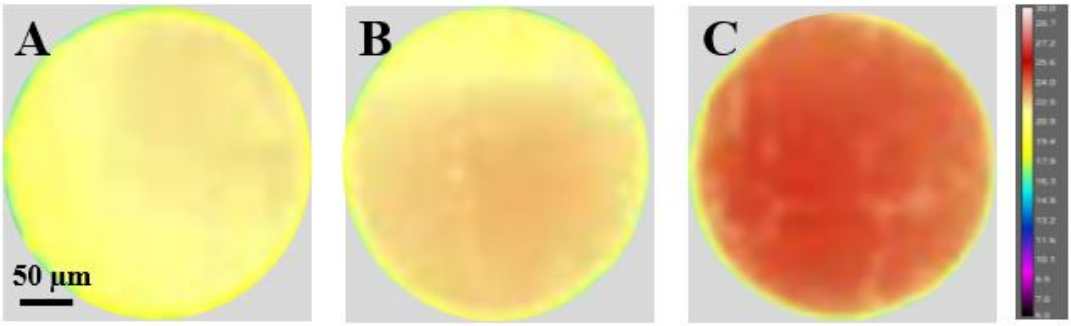

Figure 25. Temperature distribution for three different pores at 0.7 s.

19 to 22 °C. As such, the variation in temperature in a single pore was difficult to distinguish in the channel scale by using the thermal camera. Fig. 25C also shows the temperature distribution at 0.7 s. However, the temperature in this case was found to increase by a slightly higher margin (19 °C to 24 °C), with a more uniform temperature distribution. These findings indicate that the variation in temperature distribution is not uniform, even at the pore scale level.

Four channels (36 pores) were examined more closely to understand the relationship between temperature distribution and hydrogen gas bubble generation. Fig. 26A shows channels #1 and #2, and Fig. 26B shows channels #4 and #5. All images were captured at 2.5 s. As shown within the black ovals, the areas with the highest temperature (26 °C) were situated on the top portion of the channel in Fig. 26A, and on the top right corner of the channel in Fig. 26B. The generation of hydrogen gas bubbles in the four channels was also captured with a high-speed camera (Fig. 26I and 26II). More bubbles were generated on

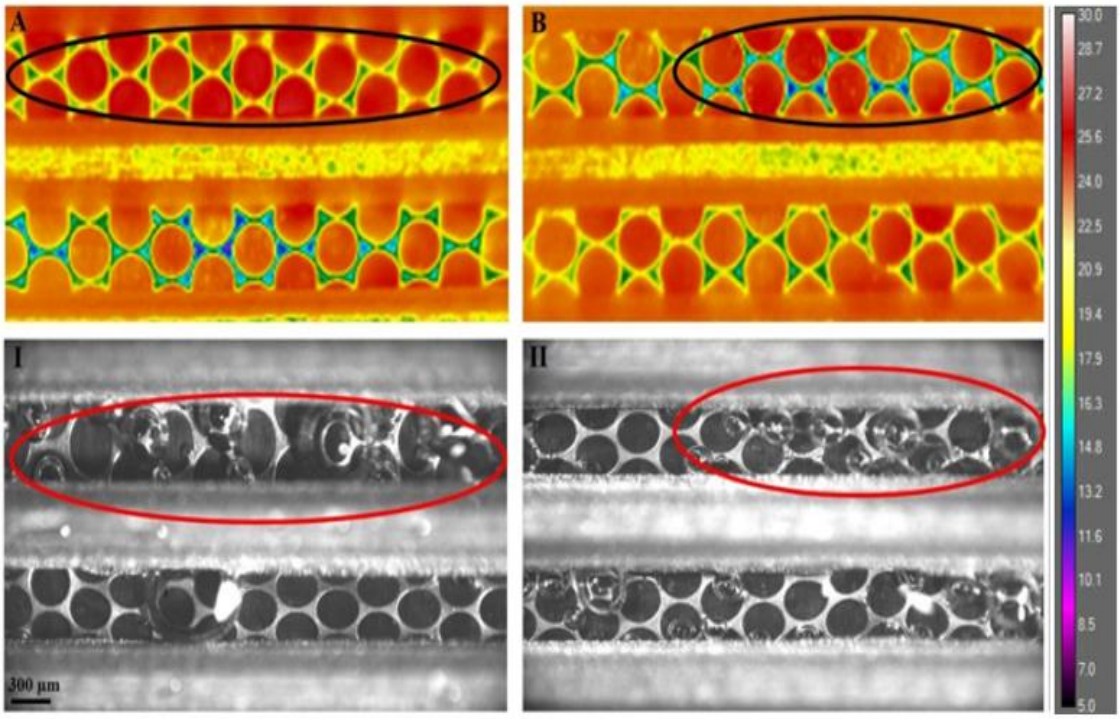

Figure 26. Comparison between heat generation (A) and (B) and hydrogen gas bubble generation (I) and II) in the channel scale experiments. (A) and (I) show channels #1 and #2. (B) and (II) show channels #5 and #6.

the top portion of the channel than on the bottom portion, which indicates a reasonable correlation with temperature distribution. This result suggests a positive correlation between temperature and electrochemical reaction, whereby a higher temperature would indicate a stronger electrochemical reaction.

Subsequently, a series of pore scale analyses of temperature distribution and hydrogen gas production on the cathode side were conducted in order to establish the relationship between the two phenomena. As shown in Figs 27A-27D, the temperature increased rapidly from approximately 19 to 23 °C, with an average rate of temperature increase of 4.4 °C/s on average on the CCM within 0.90 s. The rate of temperature increase was maintained at 10 °C/s from 0.0 s to 0.3 s.

Thereafter, the rate gradually diminished to 3.3 °C/s until reached equilibrium at 0.90 s. Bubble generation reactions are shown in Figs 27I to 27IV. The recording frame rate for the hydrogen bubble generation test was 3,000 fps. Hydrogen gas bubbles were initially generated at the bottom of the pore, and, subsequently, the diameter of the bubbles gradually increased with an average bubble growth rate of 77 μm/s (Figs 27II to 27IV).

The images show that bubble generation sites (active sites) were at the bottom of the pore, which is consistent with the temperature increase area (i.e., the bottom side of the pore). It is assumed that the heat generated at these sites came directly from the electrochemical reaction, and, consequently, the temperature rose on the bottom portion of the pore. The heat generated gradually transferred to other areas on the pore surface, whereas the reaction sites remained in the same places. Finally, this phenomenon has been

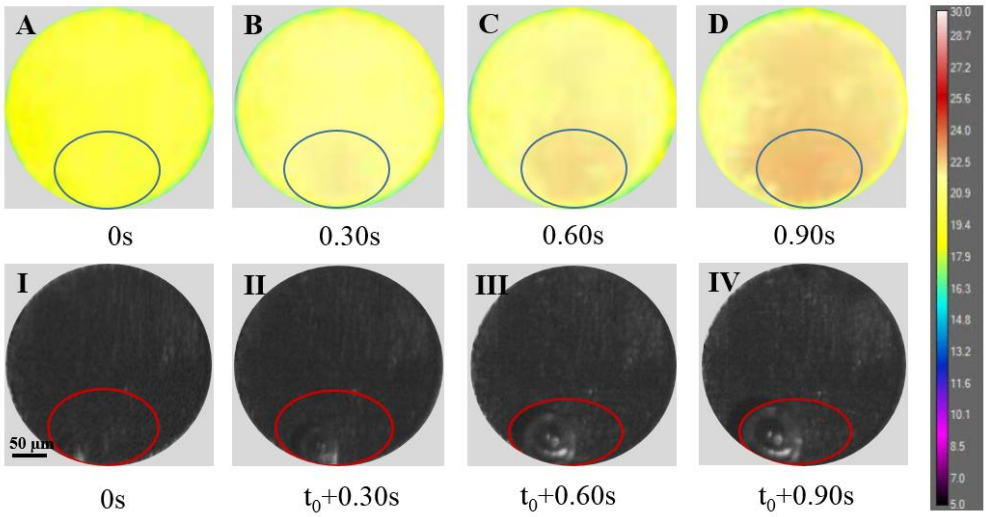

Figure 27. Comparison between heat generation and hydrogen gas bubble generation in the pore scale experiments. (A) to (D) illustrate variation in temperature and (I) to (IV) demonstrate bubble generation.

found to be replicable in most of the pores.

The results shown in Fig. 27 demonstrate that hydrogen gas bubble generation sites (or electrochemical reaction sites) were consistent with heat generation sites for most pores. The electrochemical reaction and heat generation process were observed to occur simultaneously at the same sites with positive correlation. Thus, the slower the electrochemical reaction, the lower the temperature.

In order to further demonstrate and investigate the temperature increase phenomenon at the cathode side, additional investigations of the LGDL were conducted at the same

working conditions, with an input emissivity of 0.19 (based on the calibration method mentioned previously). As shown in Fig. 28, the white areas represent the CCM, and the yellow areas represent the LGDL. A comparison with the true temperature (19 °C) revealed that the temperature at some areas on the LGDL was not captured accurately with an input emissivity of 0.19. The temperature difference on the LGDL can be attributed to the different surface morphologies. However, this investigation was mainly concerned with detecting qualitative changes and the increasing trend in temperature value, and it was possible to accurately identify this trend. The temperature increased rapidly over the whole period, the rate of temperature increase was approximately 3.33 °C/s from 0.0 to 1.5 s. Thereafter, the rate of temperature increase gradually diminished until 2.5 s with a maximum temperature of 27 °C. The temperature reached the equilibrium state after 2.5 s. This phenomenon indicates a close correlation with the temperature increase on the CCM. At first, the CCM and the LGDL were both at the same temperature. However, when the cell began to operate, heat was generated due the electrochemical reaction and ohmic resistance. As such, the heat gradually transferred to the surrounding LGDL. The temperature on the LGDL was observed to increase and eventually reach an equilibrium state. It is believed that the temperature increase on the LGDL is directly related to the ohmic resistance and heat transferred from the CCM.

4.6 Conclusions

In the present study, a specific PEMEC was developed to visualize hydrogen gas bubble generation, and temperature variance in the cathode channels. It was observed that the

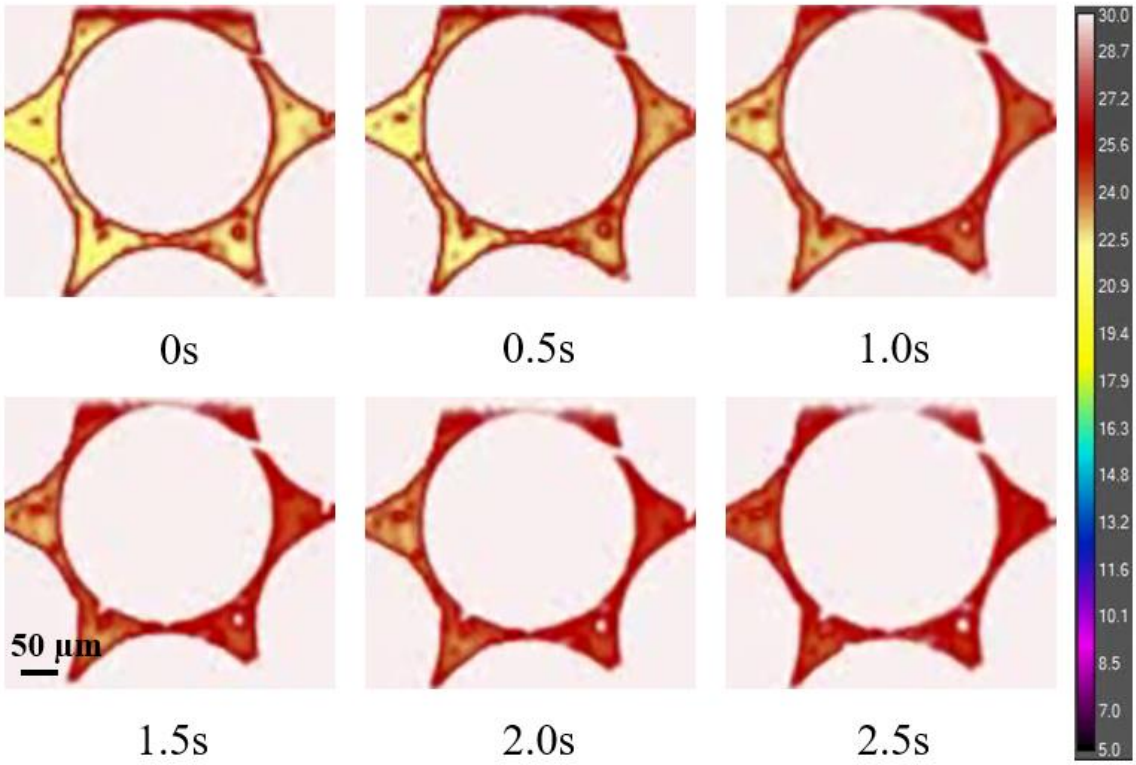

Figure 28. Sequence of photographs showing the evolution of temperature distribution on the LGDL.

temperature field in the entire channel was not uniform; some pores had a relatively higher temperature than the others. The temperature gradually increased until it reached the equilibrium state. During this process, the areas with the highest temperature in the channels were consistent with the highest hydrogen bubble generation rate areas, which means that heat release occurred due to an active electrochemical reaction. A series of pore scale temperature distribution change phenomena have also been visualized; the results show that the temperature change phenomena vary in different pores. The reason can be attributed to the electrochemical reaction occurred in different pores. More importantly, the temperature increase areas are consistent with the bubble generation areas, and this phenomenon has been found to be replicable in other pores.

Finally, investigations on the LGDL surface shown that the temperature on the LGDL also increased rapidly with respect to time. The reason can be attributed to the ohmic loss and heat transferred from the CCM. These findings could help better understand the correlation between the cathode side electrochemical reaction and heat generation, in order to provide a basis for future research, both in terms of modeling and experiment.

References

1. Jafary, T., et al., Clean hydrogen production in a full biological microbial electrolysis cell. International Journal of Hydrogen Energy, 2018.

2. Vidales, A.G. and S. Omanovic, Evaluation of nickel-molybdenum-oxides as cathodes for hydrogen evolution by water electrolysis in acidic, alkaline, and neutral media. Electrochimica Acta, 2018.

3. Pivovar, B., N. Rustagi, and S. Satyapal, Hydrogen at Scale (H2@ Scale): Key to a Clean, Economic, and Sustainable Energy System. The Electrochemical Society Interface, 2018. 27(1): p. 47-52.

4. Burhan, M., et al., A pathway for sustainable conversion of sunlight to hydrogen using proposed compact CPV system. Energy Conversion and Management, 2018. 165: p. 102-112.

5. Wang, J., Y. Gao, and F. Ciucci, Mechanochemical Coupling of MoS2 and Perovskites for Hydrogen Generation. ACS Applied Energy Materials, 2018. 1(11): p. 6409-6416.

6. Schalenbach, M., et al., A Perspective on Low-Temperature Water Electrolysis–Challenges in Alkaline and Acidic Technology. Int. J. Electrochem. Sci, 2018. 13: p. 1173-1226.

7. Patel, C., et al., Enhanced hydrogen generation by water electrolysis employing carbon nano-structure composites. International Journal of Hydrogen Energy, 2018. 43(6): p. 3180-3189.

8. Rivarolo, M., et al., Thermo-economic analysis of a hydrogen production system by sodium borohydride (NaBH 4). International Journal of Hydrogen Energy, 2018. 43(3): p. 1606-1614.

9. Ni, M., M.K. Leung, and D.Y. Leung, Energy and exergy analysis of hydrogen production by a proton exchange membrane (PEM) electrolyzer plant. Energy conversion and management, 2008. 49(10): p. 2748-2756.

10. Wang, J., et al., Water splitting with an enhanced bifunctional double perovskite. ACS Catalysis, 2017. 8(1): p. 364-371.

11. Wang, J., et al., Bimetal-decorated nanocarbon as a superior electrocatalyst for overall water splitting. Journal of Power Sources, 2018. 401: p. 312-321.

12. Millet, P. and S. Grigoriev, Water electrolysis technologies. Renewable Hydrogen Technologies: Production, Purification, Storage, Applications and Safety, 2013: p. 19-41.

13. Nie, J. and Y. Chen, Numerical modeling of three-dimensional two-phase gas–liquid flow in the flow field plate of a PEM electrolysis cell. international journal of hydrogen energy, 2010. 35(8): p. 3183-3197.

14. Martinez, S.S., et al., Coupling a PEM fuel cell and the hydrogen generation from aluminum waste cans. International Journal of Hydrogen Energy, 2007. 32(15): p. 3159-3162.

15. Han, B., et al., Modeling of two-phase transport in proton exchange membrane electrolyzer cells for hydrogen energy. International Journal of Hydrogen Energy, 2017. 42(7): p. 4478-4489.

16. Mo, J., et al., Thin liquid/gas diffusion layers for high-efficiency hydrogen production from water splitting. Applied Energy, 2016. 177: p. 817-822.

17. Kang, Z., et al., Investigation of thin/well-tunable liquid/gas diffusion layers exhibiting superior multifunctional performance in low-temperature electrolytic water splitting. Energy & Environmental Science, 2017. 10(1): p. 166-175.

18. Hu, M., et al., Three dimensional, two phase flow mathematical model for PEM fuel cell: Part I. Model development. Energy Conversion and Management, 2004. 45(11-12): p. 1861-1882.

19. Lee, C., et al., Influence of limiting throat and flow regime on oxygen bubble saturation of polymer electrolyte membrane electrolyzer porous transport layers. International Journal of Hydrogen Energy, 2017. 42(5): p. 2724-2735.

20. Nie, J., Y. Chen, and R.F. Boehm. Numerical modeling of two-phase flow in a bipolar plate of a PEM electrolyzer cell. in ASME 2008 International Mechanical Engineering Congress and Exposition. 2008. American Society of Mechanical Engineers.

21. Andreassen, K., Hydrogen production by electrolysis, in Hydrogen Power: Theoretical and Engineering Solutions. 1998, Springer. p. 91-102.

22. Visitdumrongkul, N., et al., Enhanced performance of solid oxide electrolysis cells by integration with a partial oxidation reactor: Energy and exergy analyses. Energy Conversion and Management, 2016. 129: p. 189-199.

23. Ferrero, D. and M. Santarelli, Investigation of a novel concept for hydrogen production by PEM water electrolysis integrated with multi-junction solar cells. Energy conversion and management, 2017. 148: p. 16-29.

24. Dutta, S.S., S, Numerical prediction of temperature distribution in PEM fuel cells. Numerical Heat Transfer: Part A: Applications, 2000. 38(2): p. 111-128.

25. Wilkinson, M., et al., In situ experimental technique for measurement of temperature and current distribution in proton exchange membrane fuel cells. Electrochemical and Solid-State Letters, 2006. 9(11): p. A507-A511.

26. Mo, J., et al., Discovery of true electrochemical reactions for ultrahigh catalyst mass activity in water splitting. Science Advances, 2016. 2(11): p. e1600690.

27. Mo, J., S. Steen, and F.-Y. Zhang. High-speed and micro-scale measurements of flow and reaction dynamics for sustainable energy storage. in 13th International Energy Conversion Engineering Conference. 2015.

28. Ito, K., et al., Analysis and visualization of water flow impact on hydrogen production efficiency in solid polymer water electrolyzer under high-pressure condition. International Journal of Hydrogen Energy, 2015. 40(18): p. 5995-6003.

29. Huang, P.-H., et al., Evaporation analysis of different fuels in evaporator coil of steam reformer for stationary PEM fuel cell systems. Applied Thermal Engineering, 2018. 128: p. 564-577.

30. Immerz, C., et al., Experimental characterization of inhomogeneity in current density and temperature distribution along a single-channel PEM water electrolysis cell. Electrochimica Acta, 2018. 260: p. 582-588.

31. Movahedi, M., A. Ramiar, and A. Ranjber, 3D numerical investigation of clamping pressure effect on the performance of proton exchange membrane fuel cell with interdigitated flow field. Energy, 2018. 142: p. 617-632.

32. Ju, H., H. Meng, and C.-Y. Wang, A single-phase, non-isothermal model for PEM fuel cells. International Journal of Heat and Mass Transfer, 2005. 48(7): p. 1303-1315.

33. Marangio, F., M. Santarelli, and M. Cali, Theoretical model and experimental analysis of a high pressure PEM water electrolyser for hydrogen production. International Journal of Hydrogen Energy, 2009. 34(3): p. 1143-1158.

34. Shiozawa, S. and T. Shimizu, Fuel cell and method of ameliorating temperature distribution thereof. 1990, Google Patents.

35. Iwata, M., et al., Performance analysis of planar-type unit SOFC considering current and temperature distributions. Solid State Ionics, 2000. 132(3-4): p. 297-308.

36. Kandlikar, S.G. and Z. Lu, Thermal management issues in a PEMFC stack–A brief review of current status. Applied Thermal Engineering, 2009. 29(7): p. 1276-1280.

37. Nagano, S., et al., Heat transfer enhancement in methanol steam reforming for a fuel cell. Energy Conversion and Management, 2001. 42(15-17): p. 1817-1829.

38. Wang, J. and F. Ciucci, In-situ synthesis of bimetallic phosphide with carbon tubes as an active electrocatalyst for oxygen evolution reaction. Applied Catalysis B: Environmental, 2019. 254: p. 292-299.

39. Fokaides, P.A. and S.A. Kalogirou, Application of infrared thermography for the determination of the overall heat transfer coefficient (U-Value) in building envelopes. Applied Energy, 2011. 88(12): p. 4358-4365.

40. Rahkonen, J. and H. Jokela, Infrared radiometry for measuring plant leaf temperature during thermal weed control treatment. Biosystems engineering, 2003. 86(3): p. 257-266.

41. Toghyani, S., et al., Thermal and electrochemical analysis of different flow field patterns in a PEM electrolyzer. Electrochimica Acta, 2018. 267: p. 234-245.

42. Li, Y., et al., In-situ investigation of bubble dynamics and two-phase flow in proton exchange membrane electrolyzer cells. International Journal of Hydrogen Energy, 2018.

43. Kotz, J.C., P.M. Treichel, and J. Townsend, Chemistry and chemical reactivity. 2012: Cengage Learning.

44. Dasent, W.E., Inorganic energetics: an introduction. 1982: CUP Archive.

45. Sanderson, R., Chemical bonds and bonds energy. Vol. 21. 2012: Elsevier.

Supplementary results

The water will diffused from the anode side to the cathode side during the operation. It is necessary for us to investigate the calibration issue with and without water. As shown in

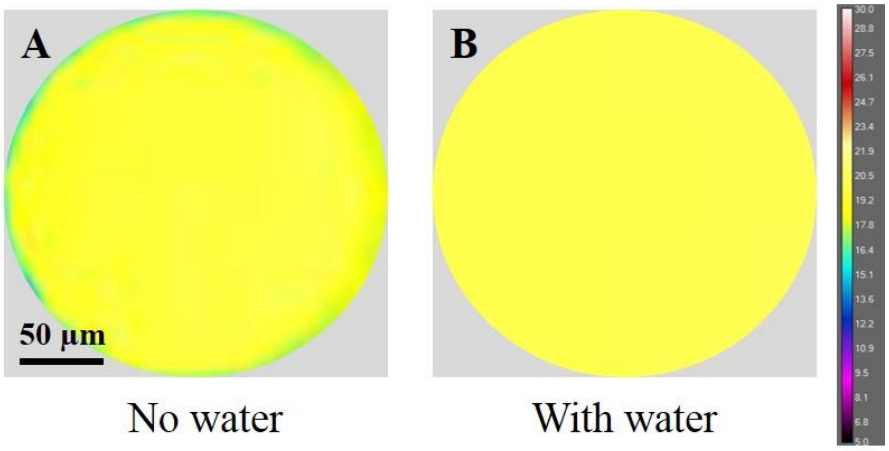

Figure 29. Investigation of the water impact on the surface temperature. (A) no water (B) with water.

Fig. 29, we investigated the impact of water on the thermal images. In Fig. 29A, the surface was maintained at room temperature of 19 °C. Then, we covered the surface with DI water (Fig. 29B), the surface temperature in the image has almost no change. This result suggests the water has only a little impact on the captured thermal images. Thus, the emissivity don't need to further calibrate during the cell operation.

The electrochemical response curve was obtained by applying a constant current density for 570 s. From Figure 30, the curve shows the voltage was maintained at around 1.57 V.

A comparison between heat generation and hydrogen bubble generation was obtained during this measurement.

Fig. 31 shows the change of temperature with respect to time. The results demonstrated that the temperature started to gradually increase from 19 °C to 22.5 °C at 1.0 s. The rate of the temperature decrease after 1.0 s. The temperature rise on the cathode side can be attributed to the interfacial contact resistance and the resistance of protons transporting through the membrane (ohmic loss). It can also be attributed to the cathode electrochemical reaction, where protons combined with electrons from the external circuit and catalyst to produce hydrogen gas. The change in internal energy for the process of uniting protons and electrons (and thereby minimizing repulsions) is negative. The bond formation reaction is also a heat release process. Therefore, the cathode side electrochemical reaction is expected to release heat energy (exothermic process).

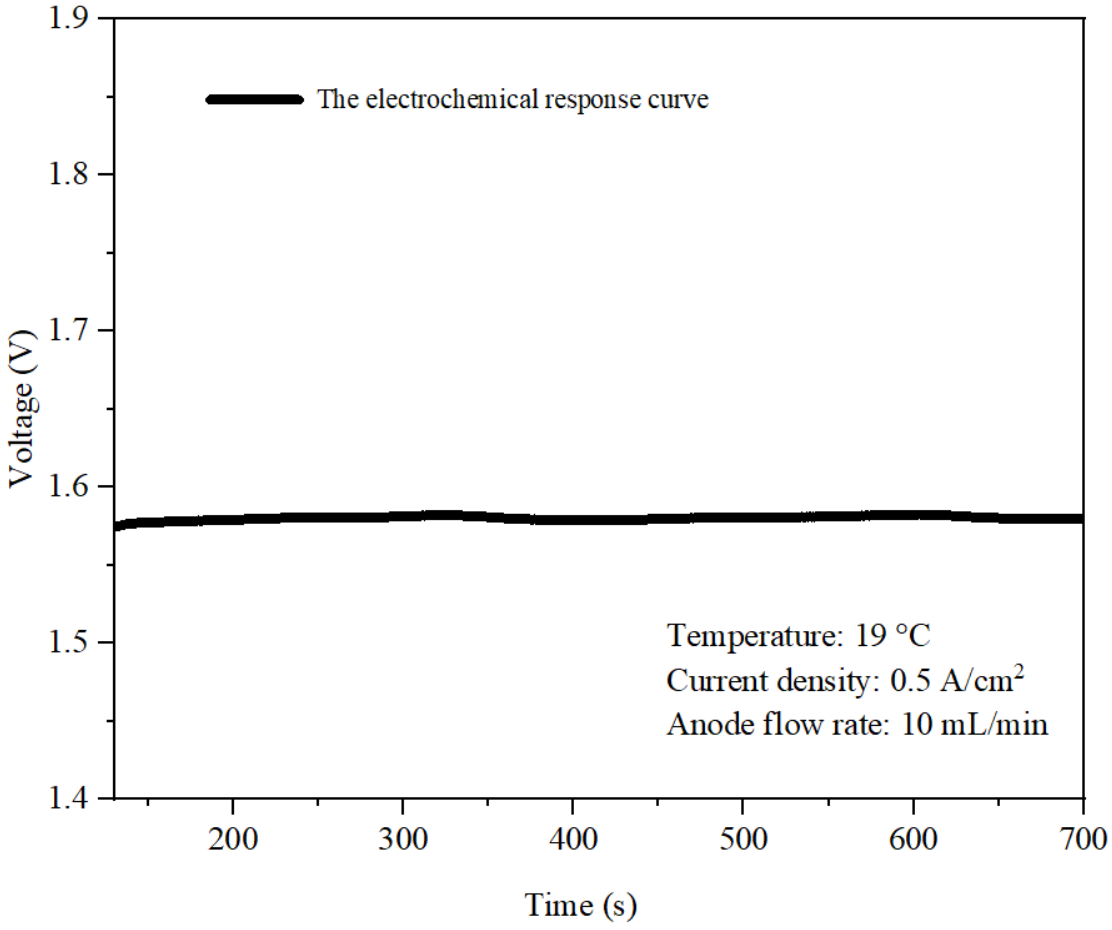

Figure 30. The electrochemical response curve.

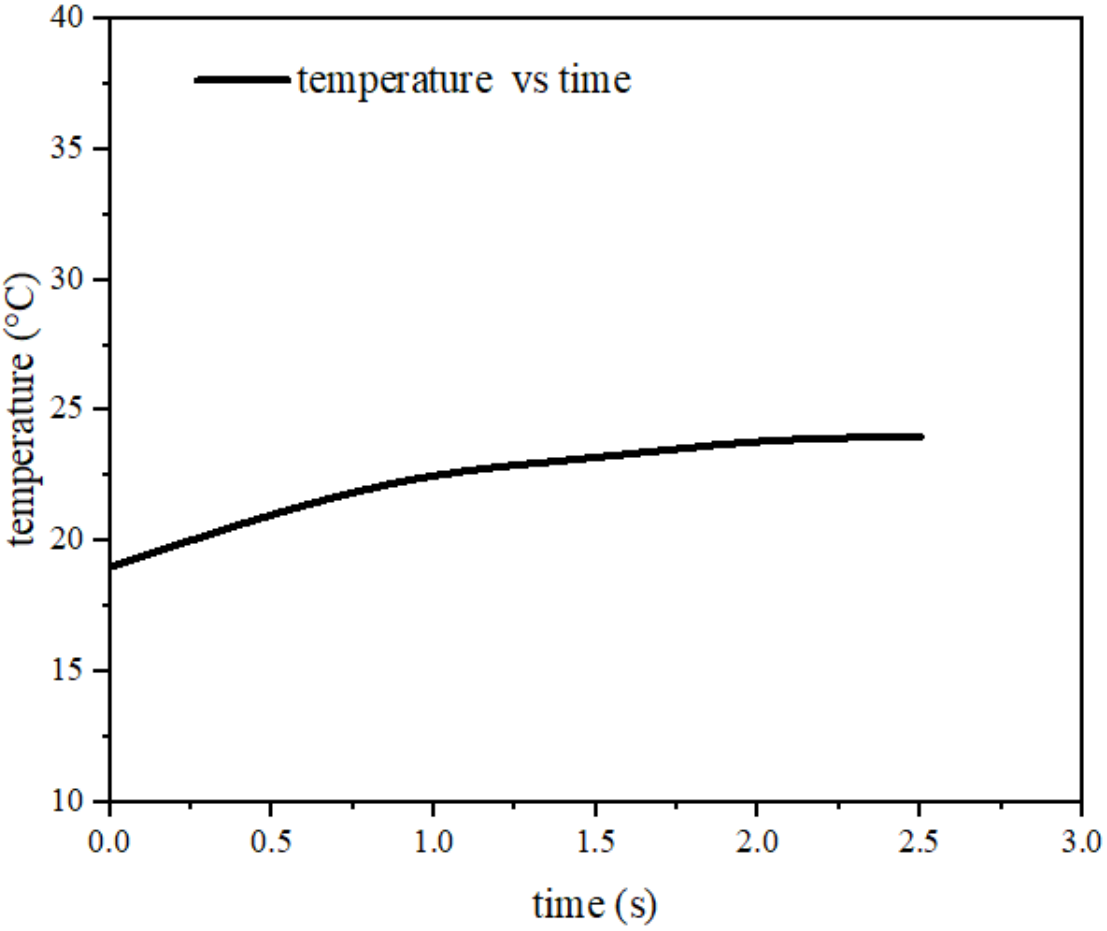

Figure 31. Temperature change with respect to time.

CHAPTER V

IN-SITU INVESTIGATION AND MODELING OF ELECTROCHEMICAL REACTIONS WITH SIMULTANEOUS OXYGEN AND HYDROGEN MICROBUBBLE EVOLUTIONS IN WATER ELECTROLYSIS

A version of this chapter was originally published by Yifan Li:

Yifan Li, Gaoqiang Yang, Shule Yu, Zhenye Kang, Jingke Mo, Bo Han, Derrick A. Talley, Feng-Yuan Zhang. "In-situ investigation and modeling of electrochemical reactions with simultaneous oxygen and hydrogen microbubble evolutions in water electrolysis." Journal of hydrogen energy.

I am fully responsible for the work submitted in these publications.

5.1 Abstract

The development of water electrolyzer is challenging as we approach theoretical limits arising from electrochemical reactions and micro-scale bubble dynamics. In this research, two-phase flow and bubble dynamics are *in-situ* studied in a special designed single-channel electrolyzer. The devices printed by a 3D printer provide a whole vision of the electrochemical reaction within the channel. *In-situ* observations of channel-scale hydrogen and oxygen micro-bubbles dynamics are conducted, the whole process of hydrogen evolution reactions (HERs) and oxygen evolution reactions (OERs) are simultaneously studied. The results indicate that the operating conditions have a great impact on the bubble evolution process, the bubble detachment diameter is inversely proportional to the flow velocity, but is in direct proportion to the current density. In addition, hydrogen bubbles are more and smaller than the oxygen bubbles. All bubbles are found to generate at the edge of the Pt wires. Finally, a mathematic model has been built, and shows a good agreement with experimental data. Those results could help to better

understand the bubble evolution mechanism, in order to further understand the electrochemical reaction.

5.2 Graphical abstract

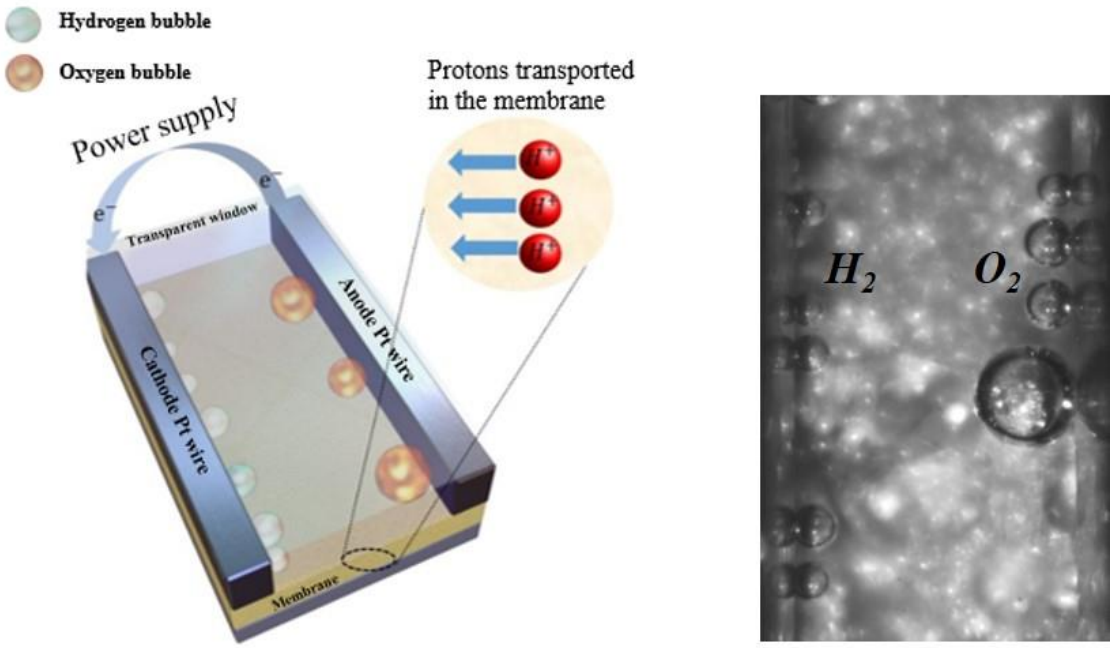

Electrochemical reaction in the channel

5.3 Highlights

- A novel channel is developed to study electrochemical processes in electrolyzer.
- Microscale hydrogen/oxygen evolution reactions are visualized simultaneously.
- Oxygen bubble detachment diameter is larger than that of hydrogen bubble.
- A model shows a good agreement with experimental results.

5.4 Introduction

Hydrogen is a clean gas that has been used for many years to convert energy without any environmental damage, especially in some places that cannot use fossil fuel. The electrolysis of water, one of the most efficient ways to produce oxygen and hydrogen, has been extensively researched to enhance the operating performance [1-3]. Bubble formation in the electrolysis of water has been commonly observed on anode and cathode side, and this process has also attracted a lot of attention around the world [4, 5]. However, the complexity of gas generation process causes many difficulties for fully understanding the general mechanism of the electrolysis of water. Similar to PEM fuel cells (PEMFCs), microscale bubble/droplet evolution on the reaction sites, multiscale transport through porous media, and dynamic two-phase flow greatly impacts their performance [6].

Numerous researchers studied the micro droplet and bubble dynamics for various applications [7-12]. Andrea et al. investigated the gas evolution process from bubbly flow to plug flow. They also found the lower flow velocity favored the coalescence between

CO_2 bubbles, allowing the generation of slug flow in the channel and eventually temporarily blocking the flow channel [13]. Prasad et al. investigated several important features on bubble characteristics with reference to its formation and transport near the electrode surface [14]. Their findings are useful in improving the methods of identifying several processes in which electrolysis-induced bubbles are produced. Li et al. investigated the growth of oxygen bubbles during the process of water electrolysis, they found the bubble growth process can be significantly impacted by different temperatures and different current densities [15]. They also investigated the bubble detachment process under different surface (hydrophilic and hydrophobic surface), and found the impact of wettability on the bubble dynamics is limited when the current density is low [16]. Mo et al. developed a transparent proton exchange membrane electrolyzer cell (PEMEC) and studied the electrochemical reactions and the position of the generation of microbubbles in a PEMEC, and they found that the bubbles are mainly generated at the edge of pores of liquid gas diffusion layers (LGDLs) [17-20]. Masato et al. investigated the transient behavior of both hydrogen and oxygen bubble formation in a water electrolysis cell [21]. Ito et al. investigated the detachment diameter of hydrogen bubbles under different cathode pressures and flow velocities [22]. They observed that the hydrogen bubbles were more easily detached at high flow velocities and low pressures. Ghasemi et al. studied multiphase transport in channels and porous media, and further investigated the micro-scale two-phase flow and built a volume of fluid simulation in investigating the two-phase flow dynamics [23]. Davis et al. used HSV (high speed video) to investigate the behavior of

electrochemically generated oxygen and hydrogen bubbles in a membraneless electrolyzer to research the local void fraction and gas evolution efficiency, they found the gas evolution efficiency was enhanced with pre-saturated hydrogen gas [24]. Berejnov et al. investigated the two-phase flow patterns, and used both experimental and modeling method to research the liquid water transport in porous electrodes, they found the local saturation in the channel decreased along with the flow [25]. Jouhara et al. used a CFD model to investigate the bubble dynamics and two-phase flow phenomena in a pipe, they found the multiphase flow phenomena can be reproduced in different kinds of fluids [26].

Despite the concerted effort within the field of research, there are still significant challenges in deciphering the steps of the bubble evolution process. The bubble evolution speed is ultrafast and in micro scale, especially at high current density and high flow velocity. It is difficult to capture the whole bubble evolution process without high-speed and microscale visualization system (HMVS). In addition, the HER (hydrogen evolution reactions) and OER (oxygen evolution reactions) are occurred at different electrodes. It is impossible to observe the two reactions at the same time in a traditional water electrolyzer. Finally, a comprehensive mathematics model is needed for better understanding the bubble dynamics and electrochemical reactions in a water electrolyzer.

The purpose of this work is to conduct experimental and theoretical analysis of gas bubble dynamics in a single channel electrolyzer, specifically bubble's growth and its detachment process. In this work, by using specific designed single channel electrolyzer and HMVS, the oxygen and hydrogen bubble evolution processes can be simultaneously

investigated with different operating conditions. Oxygen and hydrogen bubbles' generation, growth and detachment behavior were *in-situ* studied with different current densities, and flow velocities. A comparison between the hydrogen and oxygen bubble detachment diameter and time were conducted at different operating conditions and the same reaction site. Notably, a mathematics model was built to further explain the mechanism of bubble detachment. This research will provide a better understanding of the general electrochemical reactions during water electrolysis and identify its most suitable working conditions.

5.5 Experimental details

The single-channel water electrolyzer is tested *in-situ* and shown in Fig. 32 (A). The apparatus comprises a pair of stainless-steel end plates with an observation window opened on one end plate for the bubble visualization. A transparent plate made from plastic is used to block the water and provide visibility of the internal phenomena. A plate with a Y-junction single flow channel was printed using a 3D printer, and was served as the container for both anode (oxygen) and cathode (hydrogen) electrochemical reaction. Two 99.95% purity square shape Pt wires were placed in the middle channel, and were served as the anode electrode and cathode electrode, respectively. Meanwhile, the Pt wires were used to conduct electrons from the outside. More importantly, protons are impossible to transport in the water, so a very thin membrane with low ionic resistivity was placed under anode

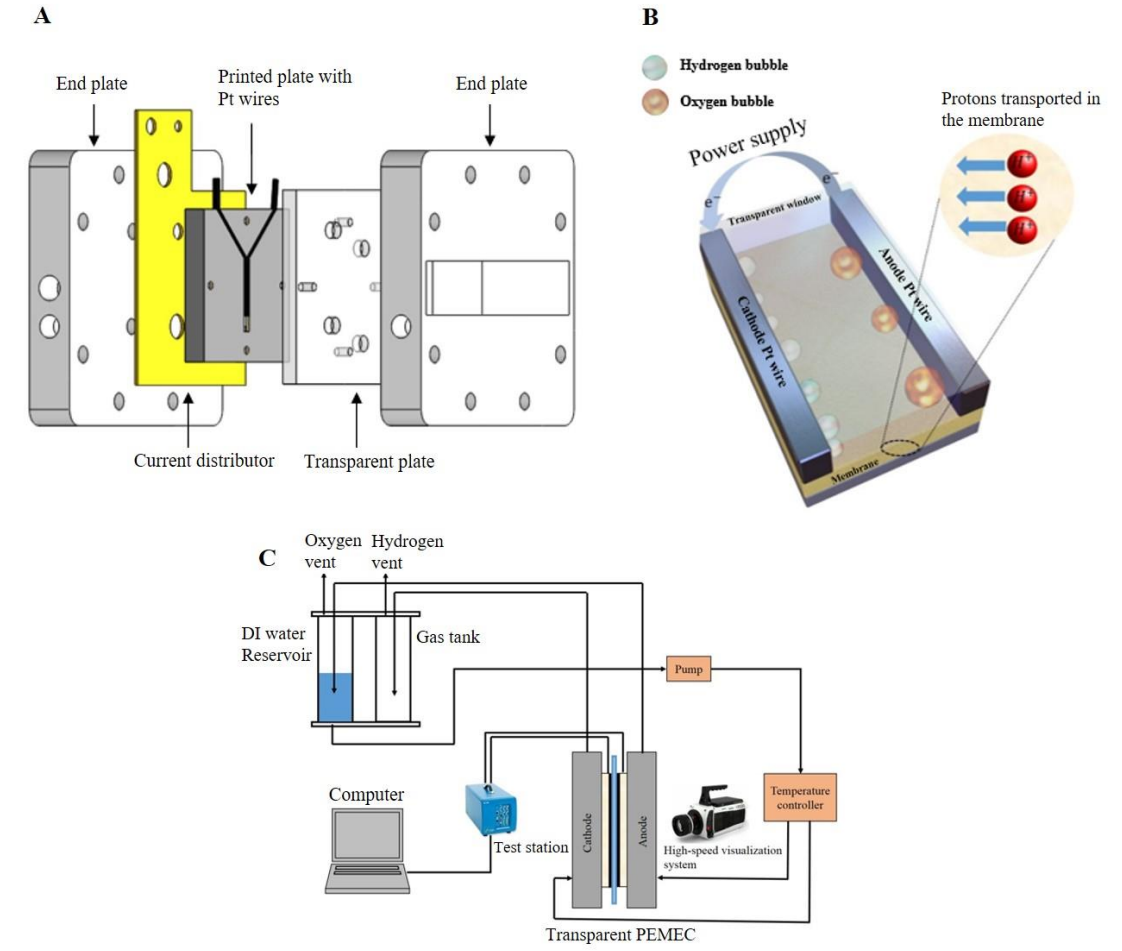

Figure 32. Schematics of the (A) single-channel electrolyzer. (B) electrochemical reaction in the channel (C) designed set-up during electrolysis.

and cathode Pt wires, and was served as the migration pathway for protons. The *in-situ* ultrafast and microscale HER and OER were observed and measured in the printed plate by using a HMVS. The electrolyzer has an active area of about 5 cm^2. The tests were operated under atmospheric pressure at room temperature. The PEMEC was attached to an electrolyzer control system with a current range up to 10 A and a voltage range up to 5 V (Potentiostat SP-300 from Bio-Logic). The schematic of the electrochemical reaction that occurred in the channel is shown in Fig. 32 (B). A phenomenon known as the Segré–Silberberg effect is used to keep the bubbles away from the center line of the channel. The parabolic nature of the laminar velocity profile in the water flow produces a shear-induced inertial lift force that drives the particles towards the channel walls. As molecules migrate closer to the channel walls, the flow around the molecules induces an increase in pressure between the particles and the wall that prevents the particles from moving closer [27]. The general mechanism of the water electrolysis in this plate is similar to a conventional PEMEC. Water flows through the channel, and then will be split into oxygen, protons, and electrons at the interface between the anode side Pt wire. The oxygen is generated at the surface of the Pt wire, and protons are transferred from the anode Pt wire to the cathode Pt wire through the membrane in the middle area and react with the electrons from the outside to form hydrogen bubbles, and hydrogen bubbles are generated on the cathode Pt wire surface. Fig. 32 (C) shows the setup of the experimental test. DI water was supplied from a water reservoir to the electrolyzer by a water pump. An electric heater with temperature controller was used to maintain the temperature at 294.15 *K*. The cell was attached to an

electrolyzer control system (Potentiostat SP-300 from Bio-Logic). A high-speed and microscale visualization system (HMVS) was used to capture the bubble dynamics and two-phase flow phenomena with a recording frame rate of 3000 fps.

5.6 Bubble dynamic model

Some models and empirical relationships have been proposed to investigate the bubble dynamic behavior.

5.6.1 Bubble growth model

The gas in the microchannel can be assumed to be an ideal gas. In the present study, a model for growing bubbles has been developed to analyze the growth of oxygen and hydrogen bubbles on the substrate surface. Then, the following equations can be derived as follows [28].

The bubble radius for one bubble can be expressed as follows:

$$r = [\frac{3iAR_gT}{\pi P_b nF(2 + 3\cos\theta - cos^3\theta)} t]^{\frac{1}{3}} \quad (1)$$

Where *iA* is the current (1 and 5 mA), F is the Faraday constant (96485 C/mol), R_g is the gas constant of 8.314 J/mol K, *T* denotes the operating temperature (294.15 *K)*, P_b is the pressure of the bubble (1 atm), and θ is the contact angle (about 31°).

The growth rate, ideally, can be described as follows [15]:

$$\dot{r} = \frac{dr}{dt} = \frac{1}{3}[\frac{3iAR_gT}{\pi P_b nF(2+3\cos\theta-cos^3\theta)}]^{\frac{1}{3}}(t)^{-\frac{2}{3}} \quad (2)$$

And the change rate of bubble velocity is the following:

$$\ddot{r} = \frac{d^2r}{dt^2} = -\frac{2}{9}\left[\frac{3iAR_gT}{\pi P_b nF(2+3\cos\theta-\cos^3\theta)}\right]^{\frac{1}{3}}(t)^{-\frac{5}{3}} \quad (3)$$

5.6.2 Bubble detachment model

This model is applied to an air-liquid system to estimate the bubble detachment diameter for various conditions in microscale. The effects of the reference variables on the bubble size are analyzed. A force balance is established and presented below for gas bubble detachment, and all forces have been calculated and expressed as the following general form (forces in black, as shown in Fig. 33):

The base radius can be calculated as follows:

$$r_c = r\sin\theta \quad (4)$$

The distance to the base can be calculated as follows:

$$r_b = r\cos\theta \quad (5)$$

The bubble growth force in the x-direction is calculated as follows [29, 30]:

$$F_{grow} = -\pi r_c^2 \rho_l \left(r\ddot{r} + \frac{3}{2}\dot{r}^2\right) \quad (6)$$

$F_{grow,x}$ is very small and can be neglected.

$\ddot{r}$ is the change rate of bubble velocity.

The surface tension force in the x-direction can be calculated as follows [29]:

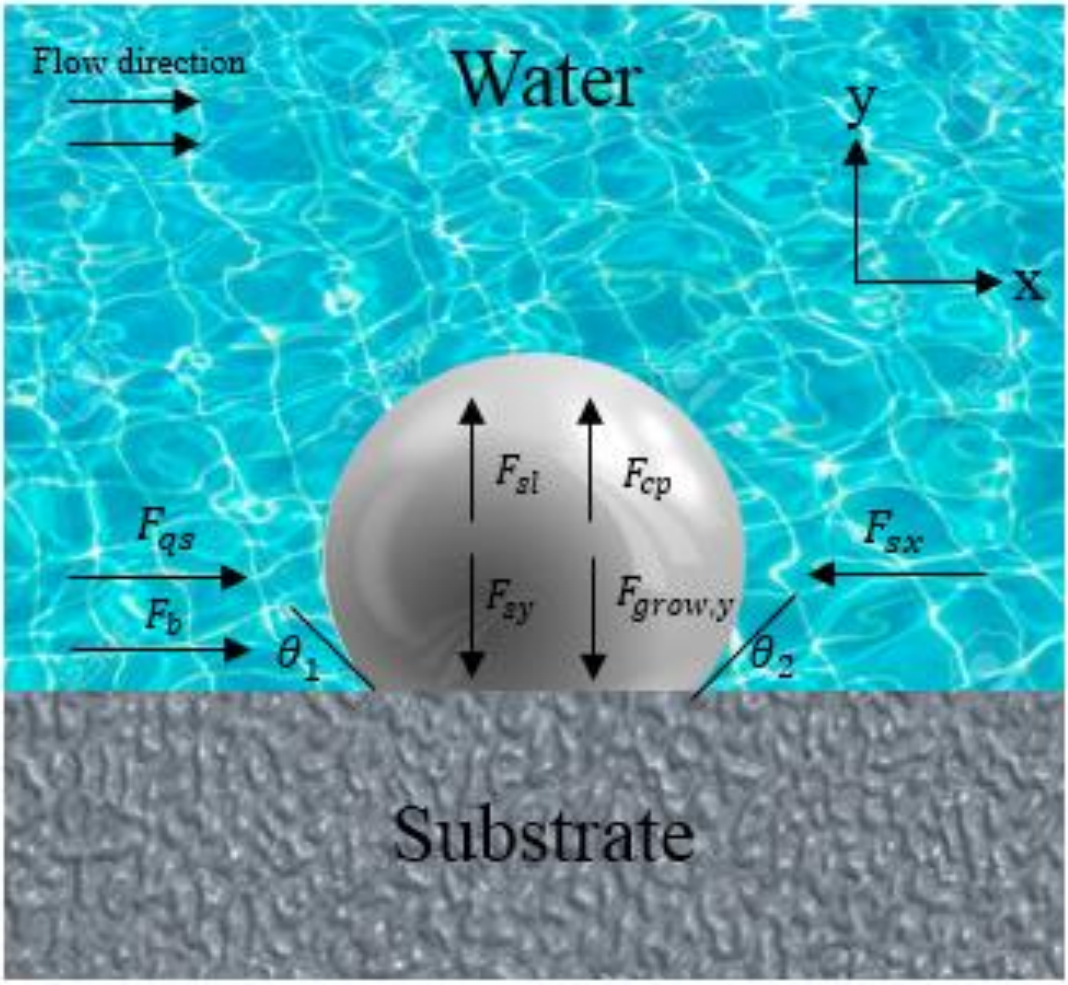

Figure 33. Forces acting on a growing bubble attached to the surface

$$F_{sx} = -2kr_c\sigma\frac{\pi(\theta_1-\theta_2)}{\pi^2-(\theta_1-\theta_2)^2}(\sin\theta_1+\sin\theta_2) \quad (7)$$

Where σ is the surface tension coefficient, 0.0719 N/m for both hydrogen and oxygen bubble [31-33], θ_1 is the advancing contact angle (43°), and θ_2 is the receding contact angle (39°), they are measured based on the videos. *k* is the correction factor and can be calculated by matching the modeling results with the experimental results and has a value of 3.2 for oxygen, and 3.0 for hydrogen.

The buoyancy force can be calculated as follows:

$$F_{buoyancy} = Vg(\rho_l - \rho_g) \quad (8)$$

Where V is bubble volume. ρ_g is the gas density (0.0824 kg/m^3 for hydrogen, 1.309 kg/m^3 for oxygen), ρ_l is the water density and has a value of 997 kg/m^3.

The quasi-steady drag force is as follows [34]:

$$F_{qs} = 6\pi\mu_l u_x r\{\frac{2}{3}+\left[\left(\frac{12}{Re_b}\right)^{0.65}+0.796^{0.65}\right]^{-\frac{1}{0.65}}\} \quad (9)$$

Where μ_l is the viscosity of water and has a value of 0.000976 kg/ms.

The bubble Reynolds number can be defined as follows:

$$Re_b = \frac{2u_x r\rho_l}{\mu_l} \quad (10)$$

The total force acting in the x-direction can be calculated as follows:

$$\sum F_x = F_{sx} + F_{qs} + F_{body} + F_b \quad (11)$$

$$F_{grow,y} = F_{grow} = -\pi r_c^2\rho_l(r\ddot{r}+\frac{3}{2}\dot{r}^2) \quad (12)$$

The surface tension force can be calculated as follows [35]:

$$F_{sy} = -2kr_c\sigma\frac{\pi}{\theta_1-\theta_2}(\cos\theta_2 - \cos\theta_1) \quad (13)$$

The shear lift force can be expressed as follows [36]:

$$F_{sl} = \frac{1}{2}\rho_l u_x^2 \pi r^2 C_l \quad (14)$$

Where C_l can be calculated as follows [37]:

$$C_l = \frac{1+16Re_b^{-1}}{2+58Re_b^{-1}} \quad (15)$$

The contact pressure can be expressed as follows [38]:

$$F_{cp} = 2\pi r_c^2 \frac{\sigma}{r_b} \quad (16)$$

The total force acting in the y-direction can be calculated as follows:

$$\sum F_y = F_{grow,y} + F_{sy} + F_{sl} + F_{cp} \quad (17)$$

Understanding the microfluidics in the channel is crucial for a further understanding of the two-phase flow mechanism in a PEMEC. As shown in the development of the model, to obtain the detachment diameter of bubbles, equations (11) and (17) should be properly solved under two different conditions. When $\sum Fx > 0$ and $\sum Fy < 0$, the bubbles depart from the initial nucleation site and slide along the LGDL surface. When $\sum Fx < 0$ and $\sum Fy > 0$, the bubble lifts off the LGDL surface. In the present model, a detachment diameter of oxygen bubbles can be obtained by solving $\sum Fx > 0$ or $\sum F$y > 0.

5.7 Results and discussions

5.7.1 Bubble dynamics in channel scale

The visualization results are recorded in the channel of width 0.5 mm, length 10 mm, and depth 0.5 mm, and the frame rate is 3000 fps. The channel is full of DI water with a flow direction from the bottom to the top.

5.7.1.1 Current density effect

Fig. 34 shows images of channel-scale bubble dynamics in the microchannel at the same flow velocity of 3.3 cm/s and at current densities of 20 mA/cm^2 and 100 mA/cm^2, respectively. The bubbles on the right edge are oxygen bubbles, and the bubbles on the left are hydrogen bubbles. The side view demonstrates that oxygen gas bubbles are nucleated less frequently than hydrogen bubbles, and the size of the hydrogen bubbles are usually smaller than the size of the oxygen bubbles. This difference is attributed to stoichiometry as the volume of oxygen gas is half that of hydrogen and oxygen bubbles cling more strongly to the electrode. In addition, there is an electrostatic repulsion force between the negative cathode and the hydrogen bubbles that are also negative in water, leading the hydrogen bubbles to more easily detach at a smaller size [39]. During the experiments, it is observed that the dynamic behaviors of bubbles, including emergence, growth, and coalescence, are similar at different working conditions. The results show that the reaction site and bubble diameter increases with increasing current density. Moreover, there are only four bubbles at 20 mA/cm^2, and the number of bubbles almost double when the current

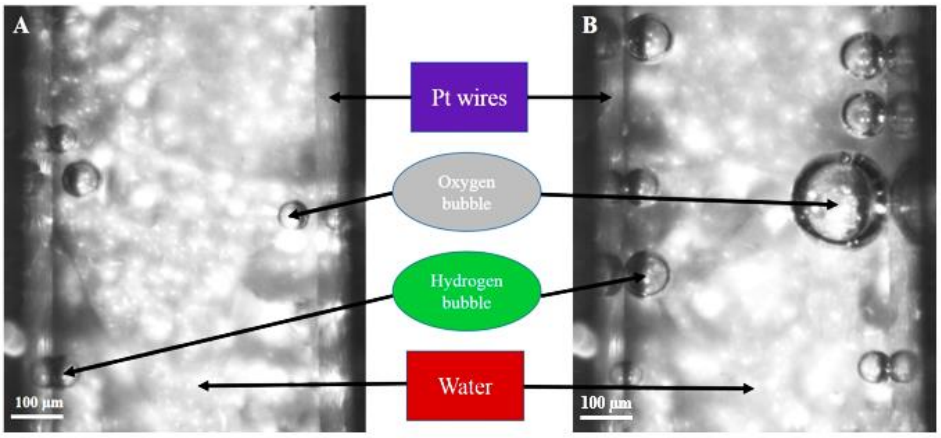

Figure 34. The bubble evolution phenomena at channel scale under room temperature and a flow velocity of 3.3 cm/s and different current densities. (A) 20 mA/cm^2, (B) 100 mA/cm^2.

density increases from 20 mA/cm^2 to 100 mA/cm^2. And the detachment size of the bubbles at 100 mA/cm^2 is almost 1.5 times larger than the detachment size of the bubbles at 20 mA/cm^2. The increase in bubble detachment size can be explained by the increasing bubble generation rate and reaction sites with the current density. The electrochemical reaction is relatively slow at low current density. As the current density gradually increases, more bubbles nucleate and grow on the Pt wire surface. This phenomenon has been observed in our previous publications [15,17].

Also, the bubble coalescence occurs more intensely at higher current density, and the gas bubble size distribution is very wide. The evolved bubbles move toward the

neighboring large bubble. The large bubble intensively grows by repeating the coalescence with other bubbles.

Bubble dynamics, under the influence of different flow velocities, have also been captured and are shown in Fig. 35. Previous research has confirmed that the flow velocity has no impact on the bubble growth rate [15]. However, the flow velocity can significantly affect the bubble detachment rate. At low flow velocity (0.7 cm/s), bubbles usually detach at a larger size as compared with the detachment size at a high flow velocity (13.3 cm/s).

As a result, bubbles tend to merge and form a large gas slug because the bubble coalescence occurs more intensely in the water at a high current density and is less likely

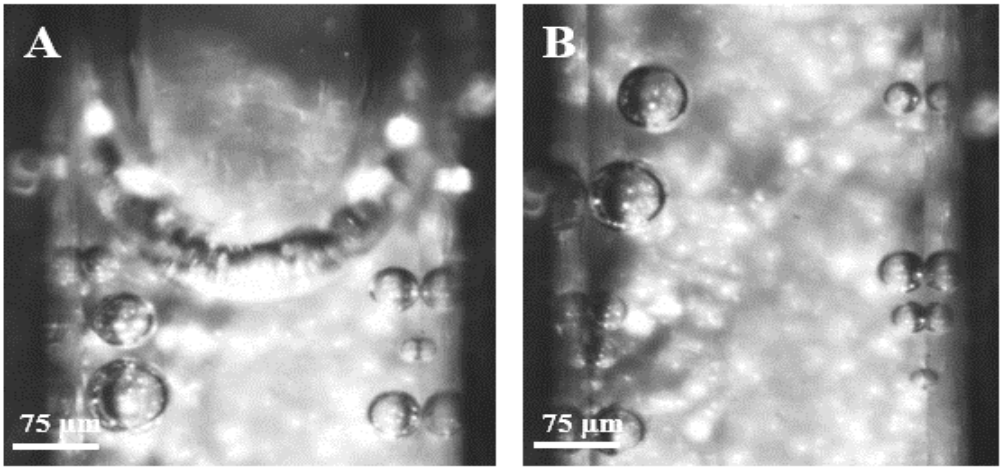

Figure 35. The different bubble evolution phenomena at channel scale under room temperature and a current density of 100 mA/cm^2 and different flow velocities. (A) 0.7 cm/s, (B) 13.3 cm/s.

to detach at a low flow velocity. As the flow velocity increased, the individual oxygen and hydrogen bubbles emerging into the channels became smaller and the coalescent gas slugs could only form at a low flow velocity. When the flow velocity reached 13.3 cm/s, a completely different bubble dynamics result is observed. The coalescence of the gas bubbles is not observed and all the bubbles are distributed discretely in the channels; these results can be explained by the fact that higher flow velocity caused higher shear stress and static pressure difference on the interface of the bubbles, making it difficult for the smaller bubbles to coalesce. More importantly, the large gas slugs disappeared from the flow field because the sweeping rate of the gas bubbles increased with the flow velocity. It is also notable that the flow velocity has almost no impact on the reaction area, because the different flow velocity does not change triple phase boundaries (TPBs), meaning the pathways for reactants and products, the catalysts, and the conductors for protons and electrons.

5.7.2 Two-phase transport in bubble scale

The visualization results are recorded in a small square shape area (200 μm × 200 μm), and the frame rate is 3000 fps. The bubble dynamics and surface wettability vary with reaction sites. Therefore, the oxygen and hydrogen bubbles we chose to compare under different flow velocities and current densities are almost at the same location in the channel.

5.7.2.1 Current density effect

First, a set of time evolution images is shown in Fig. 36 to show the evolution behavior of oxygen (Fig. 36A1 to A4) and hydrogen (Fig. 36B1 to b4) bubbles at 20 mA/cm^2 and 3.3 cm/s. Theoretically, the bubble evolution have several stages, including nucleation, growth, and detachment [40, 41]. The Fig. A1 and B1, at the initial time (t = 0 s), shows that there is no bubble generation on the surface and that the previous bubble just detached from the surface. Then (Fig. A2 and B2), oxygen and hydrogen bubbles emerged on the interface between the channel edge (Pt) and the bottom surface (Nafion), and adhered to the surface formed by surface tension force. As time progressed (Fig. A3 and B3), oxygen and hydrogen bubbles became larger. Finally, the bubble increased to its biggest size and could be clearly observed along the edge. The mechanism of bubble growth can be explained by the ideal gas law and the faraday's law [15]. After the bubble grew to a critical diameter, namely the departure diameter, it departed from the surface (Fig. A4 and B4). After its departure, the supersaturation gradually increased enough for the activation of the nucleation site to trigger a new bubble formation. Subsequently, the whole bubble evolution cycle was repeated [42, 43]. The bubble departure diameter is an important parameter for the interfacial mass transfer on the gas-evolving surface. The long-lived, large-sized bubbles blocked the flow channel and limited the incoming flow movement. Similar phenomena could be observed at different places in the channel with the same working condition. The phenomena can be understood by considering the balance of the forces exerted on one gas bubble. The previously generated bubbles in the channel were dominated by the surface tension force. The surface tension force and the bubble growth

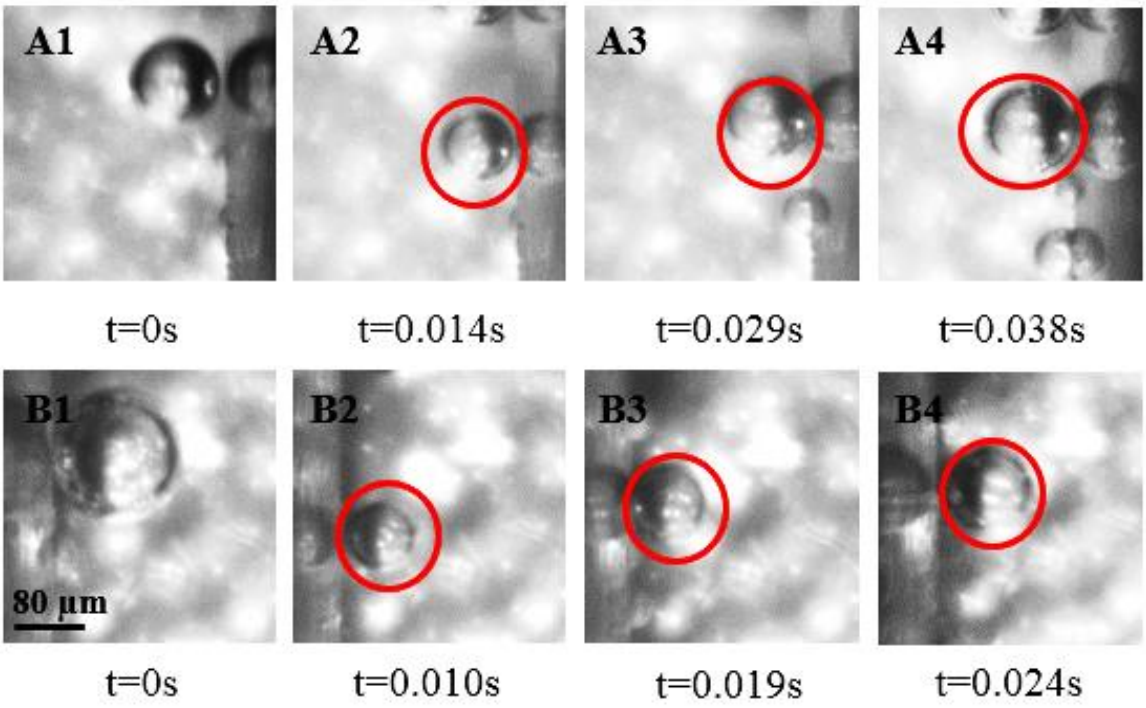

Figure 36. Sequence of photographs showing the oxygen bubble (A1 to A4) and hydrogen bubble (B1 to B4) detachment process at bubble scale under 20 mA/cm^2, and 3.3 cm/s.

force are due to the wettability of bottom and the Pt wire surface, as well as the bubble growth. As the size of the bubble gradually increases, the flow-induced force and the drag force resulting from the incoming flow become dominated, and bubbles begin to detach from the surface. According to the cathode and anode electrochemical equations, the ratio of hydrogen to oxygen is 2:1. There are more bubble nucleation sites on the cathode side than the anode, and the local current density on the cathode side is smaller than the anode [44]. The detachment diameter of the hydrogen bubbles on the cathode side is always smaller than the detachment diameter of the oxygen bubble on the anode side. Furthermore, oxygen and hydrogen bubble dynamics have also been addressed at higher current densities (100 mA/cm^2, 3.3 cm/s). As shown in Fig. 37, similar to Fig. 36, bubbles are first generated slowly on the surface. The water near the cathode becomes supersaturated with hydrogen and the increasing concentration of hydrogen at the electrode nucleates bubbles at the electrode surface at several nucleation sites. The bubble then growth and eventually detaches from the surface of the electrode as the detaching forces supersede the surface tension force. As shown in Figs. A3 and A4 in Fig. 37, the sizes of some bubbles still grow after they have detached from the surface, suggesting that the bubbles might keep growing even after detaching from the cathode surface as long as the surrounding liquid remains supersaturated [45]. The results also indicate that both the detachment diameters of oxygen and hydrogen bubbles and detachment times slightly increased as the current density increased from 20 mA/cm^2 to 100 mA/cm^2.

A problem with the flow velocity is that the flow speed cannot be very high because the

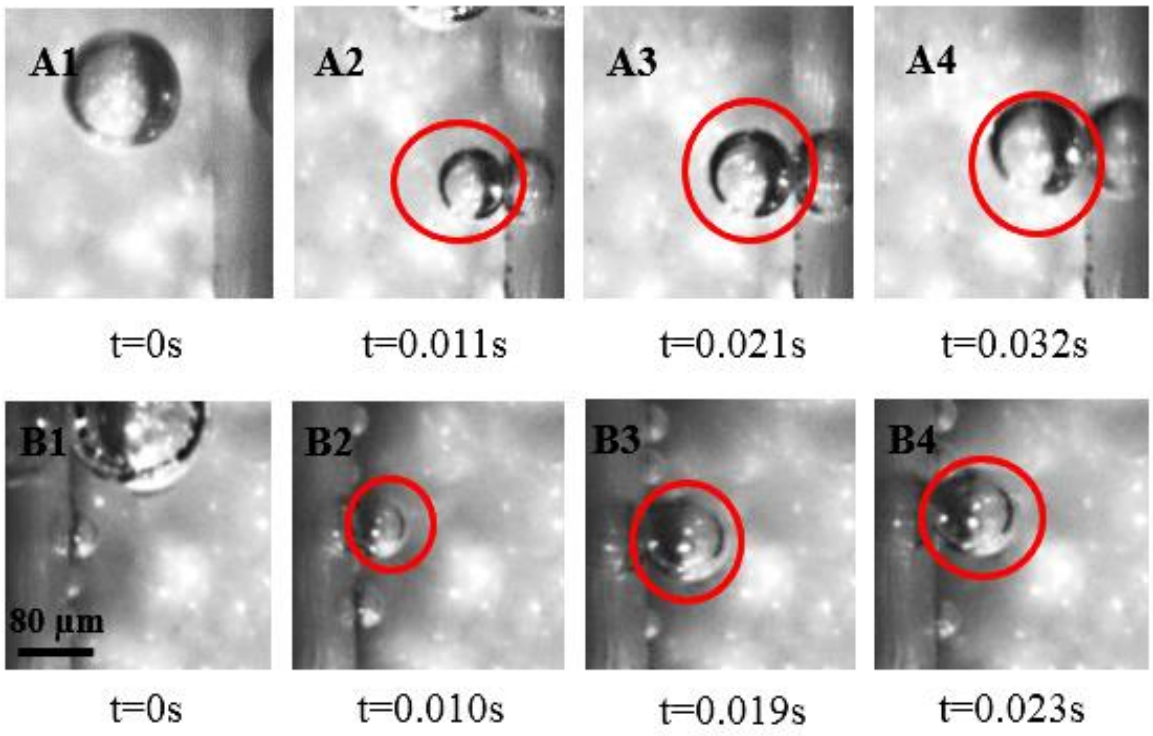

Figure 37. Sequence of photographs showing the oxygen bubble (A1 to A4) and hydrogen bubble (B1 to B4) detachment process at bubble scale under 100 mA/cm^2, 3.3 cm/s.

bubbles may need less time to detach from the surface as the flow velocity gradually increases, making it difficult to observe the whole bubble evolution process. Under this condition, a maximum flow velocity of 13.3 cm/s has been selected to efficiently observe the general bubble evolution process under the influence of different flow velocities. As shown in Fig. 38, both the oxygen and hydrogen bubble evolution processes at current density of 100 mA/cm^2 and a flow velocity of 13.3 cm/s have been observed and investigated. The results indicate that as the flow velocity increases, the gas slugs gradually disappear and the bubble size becomes smaller, eventually virtually eliminating blocking. The bubble detachment diameter is only around 40 μm for both oxygen and hydrogen and the detachment times are about 0.013 s and 0.012 s for oxygen and hydrogen, respectively. The reason for these results could be that the large flow velocity could lead to a large induced force, making the bubbles become more easy to detach.

A low flow velocity (0.7 cm/s) has been selected to compare the bubble growth and detachment results in Fig. 38. As shown in Fig. 39, at a low flow velocity, the detachment time (0.038 s for oxygen, 0.024 s for hydrogen) and detachment diameters (80 μm for oxygen, 60 μm for hydrogen) are very large compared to the results shown in previous test. The detachment diameter is about 40 μm for both oxygen and hydrogen and the detachment time is about 0.013 s and 0.012 s for oxygen and hydrogen, respectively. Equations (4) and (9) are used to understand the detachment frequency driven by the force balance modeling and the flow induced force, and the increase of drag force might need a longer time to overcome the surface tension force due to the small flow velocity. These equations suggest

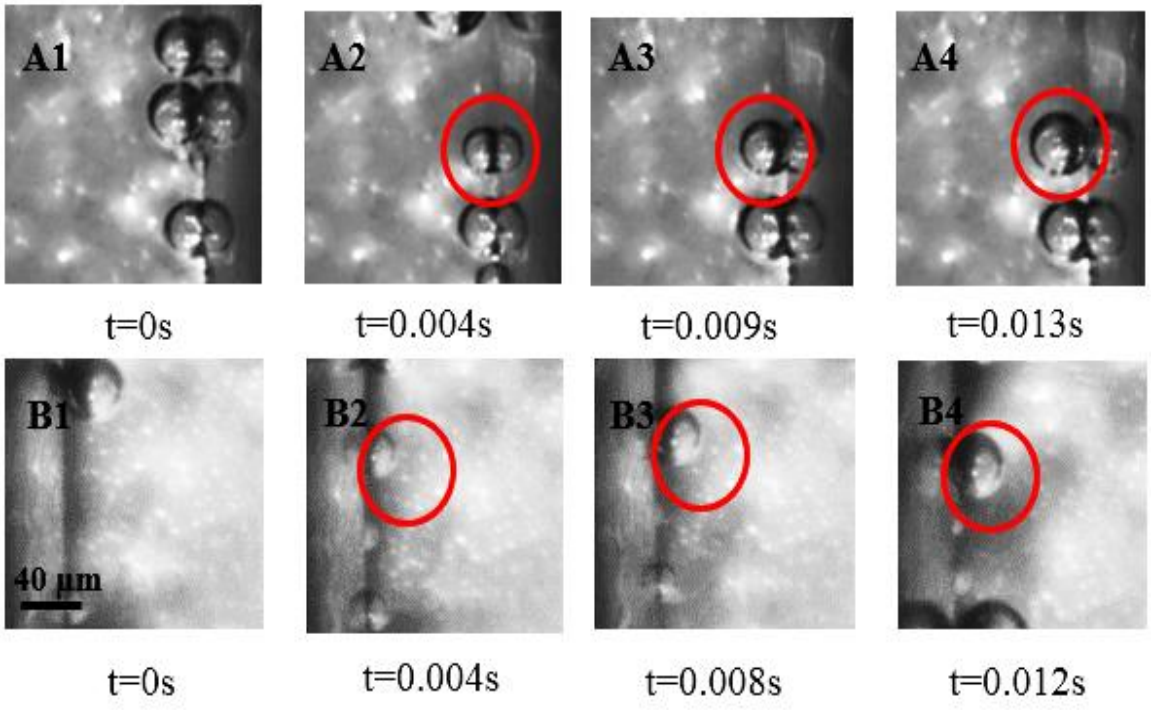

Figure 38. Sequence of photographs showing the oxygen bubble (A1 to A4) and hydrogen bubble (B1 to B4) detachment process at bubble scale under 100 mA/cm^2, 13.3 cm/s.

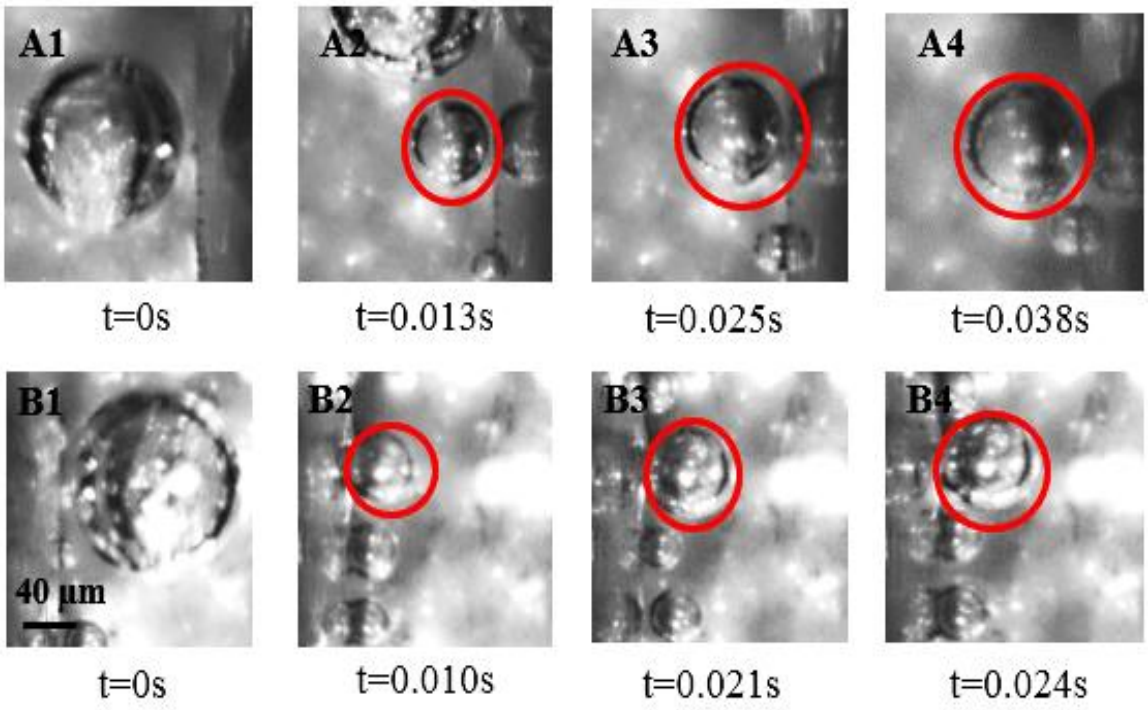

Figure 39. Sequence of photographs showing the oxygen bubble (A1 to A4) and hydrogen bubble (B1 to B4) detachment process at bubble scale under 100 mA/cm^2, 0.7 cm/s.

that the detachment time is inversely proportional to the flow velocity, namely that higher flow velocity decreases the detachment time.

Fig. 40 presents a comparison between the experimental results and modeling results about hydrogen and oxygen bubble detachment diameters at different flow velocities. When a bubble gradually grows on the surface of Pt wire, it will be impacted by multiple forces, including surface tension force, drag force, buoyancy force, body force, etc. The results show that flow velocity has a considerable effect on bubble detachment diameter. At a low flow velocity of 0.7 cm/s, the bubble diameter is large as a result of the direct influence of the small bubble induce force, the bubbles need a longer time to detach. As the flow velocity increases, the drag force and shear lift force increases. A larger total force on the x-axis and y-axis acts on a growing bubble and thus the detachment diameter decreases. More importantly, the bubble detachment process at a lower flow velocity is dominated by the buoyancy force due to the large detachment diameter, and the buoyancy force gradually decreases as the flow velocity increases. Also, the detachment diameter of hydrogen bubbles is generally smaller than the diameter of oxygen bubbles due to the smaller density, and the body force of hydrogen bubbles that induces a smaller negative total force, preventing the bubble to detach from the surface. Before using a mathematical model to forecast the bubble detachment trend, the model is authenticated using our previous visualization assessment data. Fig. 40 presents the evaluation of model data with the assessment data derived from bubble detachment experiments under the same operational parameters. The result obtained from the figures show agreement between the

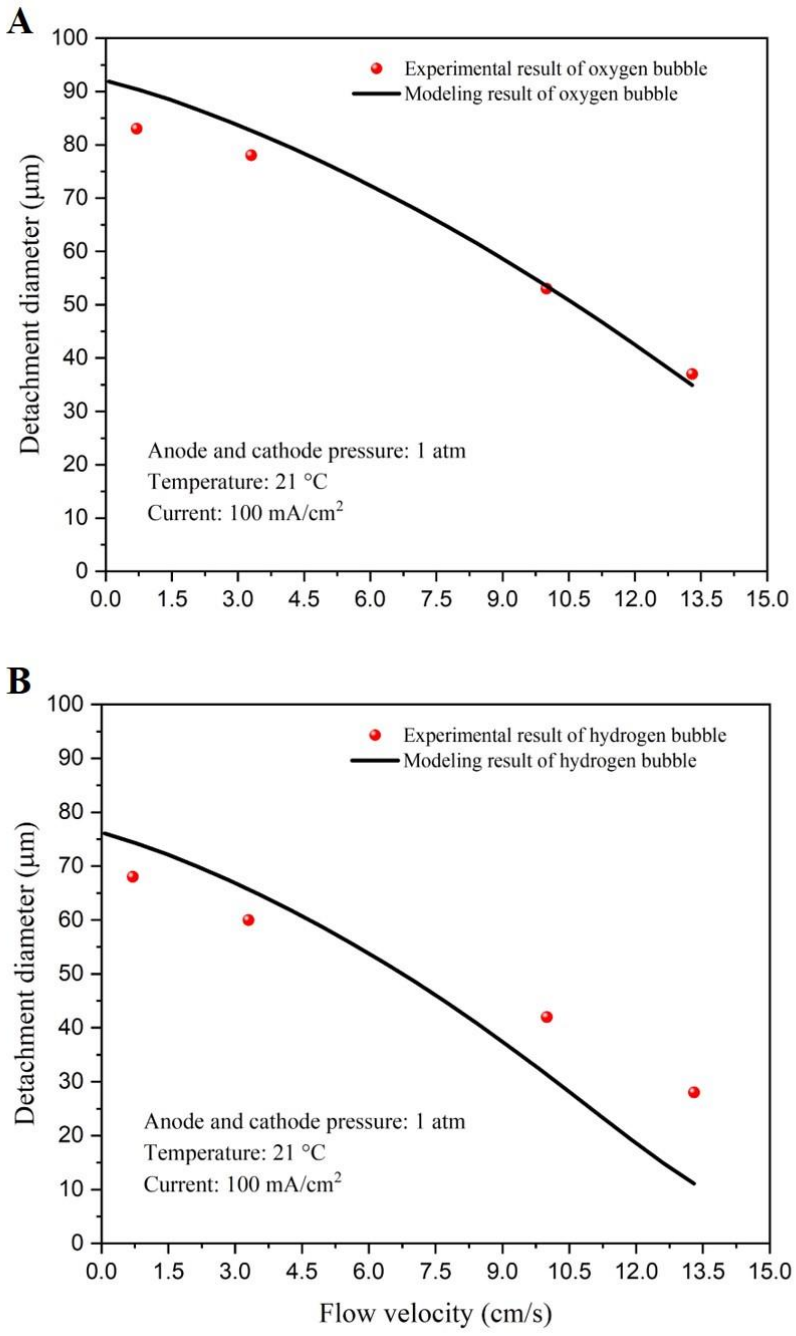

Figure 40. Comparison between modeling and experimental results under 100 mA/cm^2 respective to different flow velocities (A) oxygen (B) hydrogen.

simulation and experiment.

5.8 Conclusion

In this research, a comprehensively *in-situ* study was conducted to delineate the mechanisms of microbubble dynamics in a single-channel water electrolyzer with the help of the state-of-the-art characterization system. A transparent single-channel electrolyzer was developed to visualize oxygen and hydrogen bubble behavior in the microchannel. For the first time, the oxygen and hydrogen bubble behaviors were simultaneously presented and investigated in electrolyzer. The two-phase flow phenomena have been visualized and investigated at different working conditions. In addition, both current density and flow velocity have shown clear effects on the reaction site and bubble growth rate. Bubble detachment diameter was increased with an increase of the current density, and decreased with an increase of the flow velocity. More importantly, a theoretical two-dimension model for bubble dynamics has been built to investigate the bubble detachment diameter under different operating conditions. The predictions of this model agreed with the experimental results. The results could help to better understand the bubble evolution mechanism, to evaluate the electrochemical reaction involved during water electrolysis.

References

1. Takahashi, K., et al., Titanium material or titanium alloy material having surface electrical conductivity, and fuel cell separator and fuel cell using the same. 2018, Google Patents.
2. Villagra, A. and P. Millet, An analysis of PEM water electrolysis cells operating at elevated current densities. International Journal of Hydrogen Energy, 2019. 44(20): p. 9708-9717.
3. Carmo, M., et al., PEM water electrolysis: Innovative approaches towards catalyst separation, recovery and recycling. International Journal of Hydrogen Energy, 2019. 44(7): p. 3450-3455.
4. Liu, Y., et al., Effects of magnetic field on water electrolysis using foam electrodes. International Journal of Hydrogen Energy, 2019. 44(3): p. 1352-1358.
5. Koj, M., et al., Laser structured nickel-iron electrodes for oxygen evolution in alkaline water electrolysis. International Journal of Hydrogen Energy, 2019. 44(25): p. 12671-12684.
6. Omrani, R. and B. Shabani, Gas diffusion layer modifications and treatments for improving the performance of proton exchange membrane fuel cells and electrolysers: A review. International Journal of Hydrogen Energy, 2017. 42(47): p. 28515-28536.

7. Deng, G., et al., Enhancing mass transport in direct methanol fuel cell by optimizing the microstructure of anode microporous layer. AIChE Journal, 2018. 64(9): p. 3519-3528.
8. Perera, R.T., C.E. Arcadia, and J.K. Rosenstein, Probing the nucleation, growth, and evolution of hydrogen nanobubbles at single catalytic sites. Electrochimica Acta, 2018. 283: p. 1773-1778.
9. Hadikhani, P., et al., Inertial manipulation of bubbles in rectangular microfluidic channels. Lab on a Chip, 2018. 18(7): p. 1035-1046.
10. Kang, Z., et al., Novel thin/tunable gas diffusion electrodes with ultra-low catalyst loading for hydrogen evolution reactions in proton exchange membrane electrolyzer cells. Nano Energy, 2018. 47: p. 434-441.
11. Panchenko, O., et al., In-situ two-phase flow investigation of different porous transport layer for a polymer electrolyte membrane (PEM) electrolyzer with neutron spectroscopy. Journal of Power Sources, 2018. 390: p. 108-115.
12. Lange, K.J., P.-C. Sui, and N. Djilali, Pore scale simulation of transport and electrochemical reactions in reconstructed PEMFC catalyst layers. Journal of The Electrochemical Society, 2010. 157(10): p. B1434-B1442.
13. Calabriso, A., et al., Assessment of CO2 bubble generation influence on direct methanol fuel cell performance. Energy Procedia, 2015. 75: p. 1996-2002.

14. Chandran, P., S. Bakshi, and D. Chatterjee, Study on the characteristics of hydrogen bubble formation and its transport during electrolysis of water. Chemical Engineering Science, 2015. 138: p. 99-109.
15. Li, Y., et al., In-situ investigation of bubble dynamics and two-phase flow in proton exchange membrane electrolyzer cells. International Journal of Hydrogen Energy, 2018.
16. Li, Y., et al., Wettability effects of thin titanium liquid/gas diffusion layers in proton exchange membrane electrolyzer cells. Electrochimica Acta, 2019. 298: p. 704-708.
17. Mo, J., et al., In situ investigation on ultrafast oxygen evolution reactions of water splitting in proton exchange membrane electrolyzer cells. Journal of Materials Chemistry A, 2017. 5(35): p. 18469-18475.
18. Mo, J., et al., Mask-patterned wet etching of thin titanium liquid/gas diffusion layers for a PEMEC. Ecs Transactions, 2015. 66(24): p. 3-10.
19. Mo, J., et al., Discovery of true electrochemical reactions for ultrahigh catalyst mass activity in water splitting. Science advances, 2016. 2(11): p. e1600690.
20. Mo, J., et al. Visualization on rapid and micro-scale dynamics of oxygen bubble evolution in PEMECs. in 2017 IEEE 12th International Conference on Nano/Micro Engineered and Molecular Systems (NEMS). 2017. IEEE.
21. Sakurai, M., et al., Fundamental study of water electrolysis for life support system in space. Electrochimica Acta, 2013. 100: p. 350-357.

22. Ito, K., et al., Analysis and visualization of water flow impact on hydrogen production efficiency in solid polymer water electrolyzer under high-pressure condition. International Journal of Hydrogen Energy, 2015. 40(18): p. 5995-6003.

23. Ghasemi, A. and X. Li, Microfluidic two-phase interactions under variable liquid to cross-flow gas momentum flux ratios. Microfluidics and Nanofluidics, 2018. 22(11): p. 121.

24. Davis, J., et al., High Speed Video Investigation of Bubble Dynamics and Current Density Distributions in Membraneless Electrolyzers. Journal of The Electrochemical Society, 2019. 166(4): p. F312-F321.

25. Berejnov, V., et al., Fractal flow patterns in hydrophobic microfluidic pore networks: experimental modeling of two-phase flow in porous electrodes. Journal of The Electrochemical Society, 2010. 157(5): p. B760-B767.

26. Jouhara, H., B. Fadhl, and L.C. Wrobel, Three-dimensional CFD simulation of geyser boiling in a two-phase closed thermosyphon. International Journal of Hydrogen Energy, 2016. 41(37): p. 16463-16476.

27. Hashemi, S.M.H., M.A. Modestino, and D. Psaltis, A membrane-less electrolyzer for hydrogen production across the pH scale. Energy & Environmental Science, 2015. 8(7): p. 2003-2009.

28. Mo, J., Fundamental Studies of Electrochemical Reactions and Microfluidics in Proton Exchange Membrane Electrolyzer Cells. 2016.

29. Chen, D., L.-m. Pan, and S. Ren, Prediction of bubble detachment diameter in flow boiling based on force analysis. Nuclear Engineering and Design, 2012. 243: p. 263-271.

30. Yin, L. and L. Jia, Confined characteristics of bubble during boiling in microchannel. Experimental Thermal and Fluid Science, 2016. 74: p. 247-256.

31. Tucker, A. and C. Ward, Critical state of bubbles in liquid‐gas solutions. Journal of Applied Physics, 1975. 46(11): p. 4801-4808.

32. Massoudi, R. and A. King Jr, Effect of pressure on the surface tension of water. Adsorption of low molecular weight gases on water at 25. deg. The Journal of Physical Chemistry, 1974. 78(22): p. 2262-2266.

33. Jho, C., et al., Effect of pressure on the surface tension of water: Adsorption of hydrocarbon gases and carbon dioxide on water at temperatures between 0 and 50 C. Journal of Colloid and Interface Science, 1978. 65(1): p. 141-154.

34. Guan, P., et al., Bubble departure size in flow boiling. Heat and Mass Transfer, 2015. 51(7): p. 921-930.

35. Colombo, M. and M. Fairweather, Prediction of bubble departure in forced convection boiling: A mechanistic model. International Journal of Heat and Mass Transfer, 2015. 85: p. 135-146.

36. Mei, R. and J. Klausner, Shear lift force on spherical bubbles. International Journal of Heat and Fluid Flow, 1994. 15(1): p. 62-65.

37. Wang, Q. and W. Yao, Computation and validation of the interphase force models for bubbly flow. International Journal of Heat and Mass Transfer, 2016. 98: p. 799-813.

38. Guan, P., et al., Effect of bubble contact diameter on bubble departure size in flow boiling. Experimental Heat Transfer, 2016. 29(1): p. 37-52.

39. Bikerman, J.J., Surface chemistry: Theory and applications. 2013: Elsevier.

40. Lyu, P., et al., Coalescence Induced Self-Propelled Detachment of Surface Bubbles. Bulletin of the American Physical Society, 2018.

41. Van Der Linde, P., et al., Electrolysis-driven and pressure-controlled diffusive growth of successive bubbles on microstructured surfaces. Langmuir, 2017. 33(45): p. 12873-12886.

42. Yang, X., et al., Dynamics of single hydrogen bubbles at a platinum microelectrode. Langmuir, 2015. 31(29): p. 8184-8193.

43. Chen, Q., et al., Electrochemical nucleation of stable N2 nanobubbles at Pt nanoelectrodes. Journal of the American Chemical Society, 2015. 137(37): p. 12064-12069.

44. Kumar, S.S. and V. Himabindu, Hydrogen Production by PEM Water Electrolysis–A Review. Materials Science for Energy Technologies, 2019.

45. Kikuchi, K., et al., Concentration of hydrogen nanobubbles in electrolyzed water. Journal of colloid and interface science, 2006. 298(2): p. 914-919.

CHAPTER VI

IN-SITU INVESTIGATION OF THE COMPLEXITY IN MICRO-SCALE GAS BUBBLES' EVOLUTION AND TWO-PHASE FLOW PATTERNS

This chapter will be further edited and submitted for publication

I am fully responsible for the work submitted in this chapter, contributions from co-authors will be added prior to submission for publication.

6.1 Abstract

This paper reports an *in-situ* study of the oxygen bubble behavior on the anode side of a proton exchange membrane electrolyzer cells (PEMECs) with Ti felt LGDL. The finding revealed that a small current density and large flow rate, small discrete bubbles appeared in the flow field. At moderate current density and flow rate, a number of gas slugs formed, in addition to small discrete bubbles. At large current density and small flow rate, more bubbles were generated in the channel, and flow field was dominated by slug and annular flow. More importantly, a single bubble detachment process was captured and analyzed, and results showed that different current densities had a significant impact on bubble detachment diameter and frequency. Bubble detachment frequency and detachment diameter greatly increased alongside an increase in current density. Finally, bubble detachment diameter at different locations and under different current densities and flow rates were investigated. Bubble detachment diameter showed a close relationship with pore size. Additionally, bubble detachment diameter was directly proportionate to pore size. These results can help to better understand the two-phase flow and bubble detachment mechanism, and provide a foundation for electrochemical reaction studies in future.

6.2 Highlights

- Two-phase flow and bubble dynamics are *in-situ* visualized.
- Bubbles are invaded from the bottom to the top of the Ti felt.
- Slug flow tends to form at high current density and low flow rate.
- Current denisty has a great impact on the detachment frequency.

6.3 Introduction

Water electrolysis is one of the most attractive methods for saving energy and has almost no impact on the environment. Proton exchange membrane electrolyzer cells (PEMECs) have gained significant attention in the past decade. Gas generation by PEM electrolysis has many advantages: it has high efficiency, high purity, high production pressure, yields no greenhouse gas emissions, and integrates well with renewable energy resources [1-3]. This process makes it possible to produce hydrogen and oxygen in a highly efficient manner, and with a purity of up to 99.999%. PEMECs typically require only minimal maintenance and do not contain corrosive liquids other than water. However, PEMECs still require additional investigation and improvement before they can be implemented.

Bubble dynamics and two-phase flow phenomena should be investigated to develop effective mass transport. Ineffective removal of bubbles in the liquid/gas diffusion layer (LGDL) may lead to pore blockage and catalyst layer coverage, phenomena that will hinder the transport of liquid water from the flow fields to the catalyst layer. This, in turn, will

inhibit electrochemical reactions. Oxygen bubbles that accumulate in the flow channels can also impede liquid water transport and lead to higher mass transport losses. Several factors need to be considered to accurately identify the impact of different working conditions on bubble behavior, such as operating current density and liquid flow rates. To thoroughly investigate the impact of each factor on multiphase flow behavior, in situ visualization studies must be performed at the microscale level.

The working principle of a PEMEC is similar to that of a PEM fuel cell; however, in the case of the former, half of the reactions take place at opposite electrodes. The reactant water and produced H_2 and O_2 gases flow in the opposite direction to those in a PEM fuel cell. During the process of water electrolysis, water is supplied to the anode where it is dissociated into oxygen in the form of gas bubbles, protons, and electrons. The protons travel across the catalyst coated membrane to the porous cathode electrode, where they recombine with the electrons to produce hydrogen gas, which is then transported through the liquid gas diffusion layer (LGDL) and flow field toward the outlet of the cell. During this process, the anode is prone to water blockage by gas. Since water is the reactant for an electrolysis cell, it must be delivered to the active reaction sites in the anode. By-product oxygen gas may impede water delivery to the electrode if the gas is trapped in the pores of the electrode, or in the microchannel [4].

Researchers have investigated bubble dynamics in fuel cells and electrolyzers. Yang et al. investigated CO_2 gas bubble behavior inside the anode of a direct methanol fuel cell (DMFC), and found that current density, flow rate, and temperature greatly affected bubble

dynamics and cell performance [5]. Mo et al. investigated the bubble-generation mechanism in a PEMEC and found that bubbles only generated at the interface between the catalyst layer and liquid gas diffusion layer, which means using a triple phase boundary, is crucial to the electrochemical reaction [6]. Li et al. researched the impact of wettability on the bubble dynamics and performance in a PEMEC with Ti thin film LGDL and found that wettability had a limited impact on activation and transport over-potential, but a large impact on bubble dynamics at a current density ranging 0 to 2 A/cm^2 [7]. Wang et al. developed a mathematical model to investigate the bubble dynamics and multiphase flows in a fuel cell, and established that multiphase flows emerged near the channel outlet in a co-flow configuration [8, 9]. Selamet et al. researched the two-phase flow and gas bubble evolution behavior inside a PEMEC using neutrons and a high resolution camera. They found that gravity and buoyancy force can greatly affect water distribution across the cell and that active areas near the anode inlet contained more water than other areas [10]. Dedigama et al. investigated the two-phase flow phenomena inside a single channel PEMEC, and concluded that bubble diameter increased both alongside a decrease in flow rate and with an increase in potential [11]. Ito et al. studied the impact of water flow on the gas generation of a solid polymer water electrolyzer, and found that more bubbles were generated in the channel alongside an increase in water flow rate, and bubbles were more easily detached at a high flow rate [12]. Yuan et al. focused on the bubble growth and detachment process in a direct methanol fuel cell, and concluded that surface tension and buoyancy force were the main factors in the bubble growth and detachment process, and

that working current density and solution concentration can significantly affect the bubble detachment diameter [13]. Lu et al., working on the bubble dynamics in a methanol fuel cell, found that bubbles nucleated at certain locations and formed large and discrete gas slugs in the channel and that bubble detachment from the surface was significantly retarded by strong surface tension [14].

Research has been conducted into bubble dynamics and two-phase flow phenomena in other applications [15-24]. During the current study, two-phase flow phenomena and bubble dynamics within a microchannel was studied using transparent PEMECs, as well as a microscale and high-speed visualization system. Oxygen bubbles' detachment and two-phase flow phenomena in the microchannel were captured with different operating current densities and flow rates. Slug flow was found to form in the microchannels at high current density and low flow rate. More importantly, the number of bubbles and detachment frequency were increased with an increase of the current density. More bubbles were found to generate at the edge of the channels than in the middle. Current density and flow rate showed some impact on bubble detachment diameter. The bubble detachment diameter increased alongside an increase in current density, and decreased with an increase in flow rate. This research is expected to provide a better understanding of bubble detachment and two-phase flow mechanisms in PEMECs, which in turn can provide insights for improving cell performance and efficiency.

6.4 Experimental details

The experiment focused on the oxygen evolution reaction (OER) with the help of a high-speed and microscale visualization system. Fig. 41A shows the structure of the specific transparent cell used: two end plates were made from stainless steel with an observation window on the cathode-side end plate. The transparent plate was made of plastic. The current distributor on the anode side was made of a gold-coated Ti plate. The anode LGDL was Ti felt with a thickness of 350 um. A commercial catalyst-coated membrane (CCM) was made from Nafion 115 (EZ-CCM; FuelCellsEtc), with a thickness of 125 um. The catalyst employed was 3.0 mg/cm^2 $IrRuO_x$ on the anode side and 3.0 mg/cm^2 platinum black (Pt black) on the cathode side, and the working area of the CCM was 5 cm^2. The cathode LGDL was carbon paper. The gasket on the cathode had a thickness of 125 μm, and on the anode, a thickness of 280 μm. The cathode current distributor was made of copper. The cell was assembled using eight evenly distributed bolts with 40 in/lb of torque. Fig. 41B shows the setup of the experimental test rig. Deionized water (DI water) was supplied from a water reservoir to the PEMEC by a water pump. An electric heater with temperature controller was used to preheat both the DI water flowing through the cell and the cell itself. The cell was oriented vertically during the experiment. The tests were operated under atmospheric pressure and at 80 °C. The cell was attached to an electrolyzer control system with a current density range up to 5 A/cm^2 and a voltage range up to 5V (Potentiostat SP-300, developed by Bio-Logic). A high-speed and microscale visualization system (HMVS) was introduced to capture the anode side two-phase flow phenomena, at

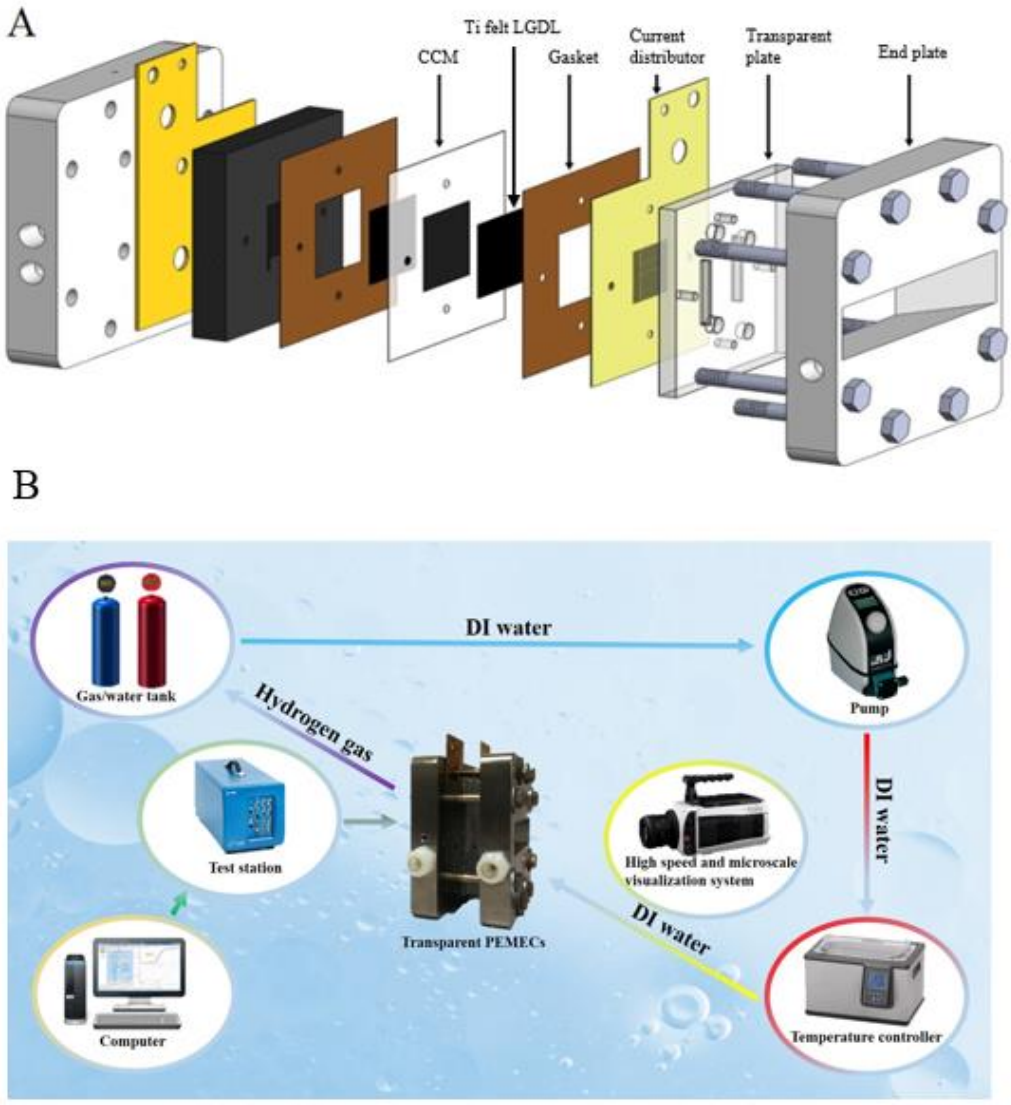

Figure 41. Schematic of the (A) transparent PEMECs, and (B) experimental setup for the visualization and electrochemical study.

a recording frame rate of 7500 fps. Research focused on two-phase flow and bubble dynamics under different operating conditions. Results obtained from the images aim to provide a comprehensive understanding of the impact of different operating conditions on two-phase flow phenomena in PEMECs with Ti felt LGDL.

6.5 Results

To investigate the LGDL morphology in terms of its ability to facilitate oxygen removal, knowledge of the distribution of the generated and accumulated bubbles is necessary. This can be achieved by drawing correlations between LGDL microstructure parameters and bubble behavior. Fig. 42A shows the multifunction of LGDL in PEMECs, where the LGDL is located between the flow channel and the catalyst layer. Its function is to transport electrons, reactant (water), and product (oxygen) to and from the catalyst layer with minimal loss [25]. Fig. 42B presents the 2D microfluidic pore network. In this figure, the air bubble is represented by the color white, the solid structure is represented by the color black, and the liquid is represented by the color blue. During the operation, bubbles were generated under the Ti felt at the interface between the Ti felt and CCM. When the pressure of a growing bubble reacheed the capillary pressure of the largest surrounding throat, it will propagated via a direct pathway from the catalyst layer to the flow channel. The bubble then detached from the surface and moved with the incoming water flow.

The image of the gas invasion in Fig. 42 illustrates how bubble transport in LGDL is dominated by both surface tension (a force between fluid molecules) and principle force (a

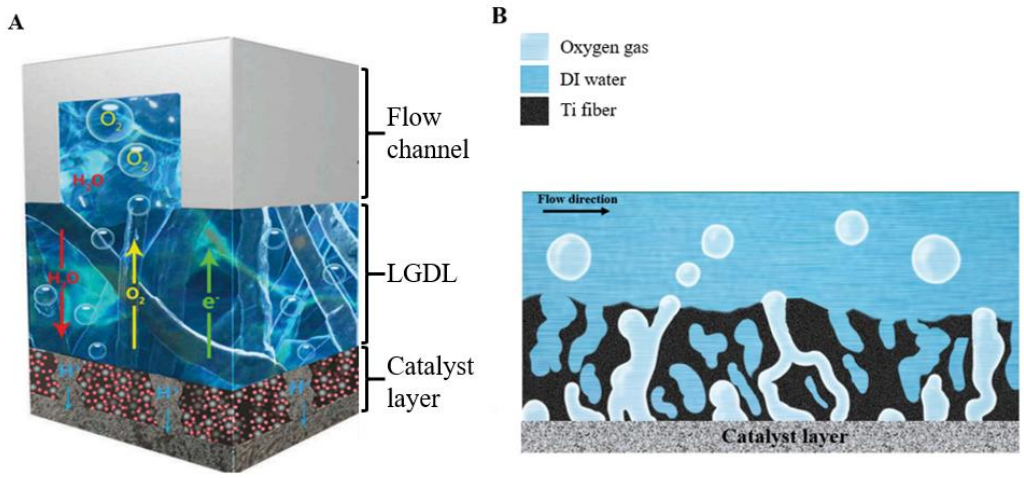

Figure 42. Schematic of the (A) LGDL multifunction in PEMECs, and (B) bubble transported in Ti felt LGDL.

force arising from the capillary effect) [22, 26].

The relationship between current density and voltage is a critical measure for the performance of PEMECs, where lower voltage for a given current density indicates better performance. Fig. 43 shows the performance of the PEMECs recorded by the visualization system. The operating temperature was 80 °C, and flow rate was 20 ml/min. As shown in this figure, the voltage gradually increased from 0 to 1.97 V, alongside an increase in current density from 0 to 2 A/cm^2. Electrochemical impedance spectroscopy (EIS) results were also obtained *in situ* with a current density of 0.2 A/cm^2. As Fig. 44 shows, the high frequency resistance (HFR) was 0.223 Ohm*cm^2. These values showed good agreement with previously published findings [27].

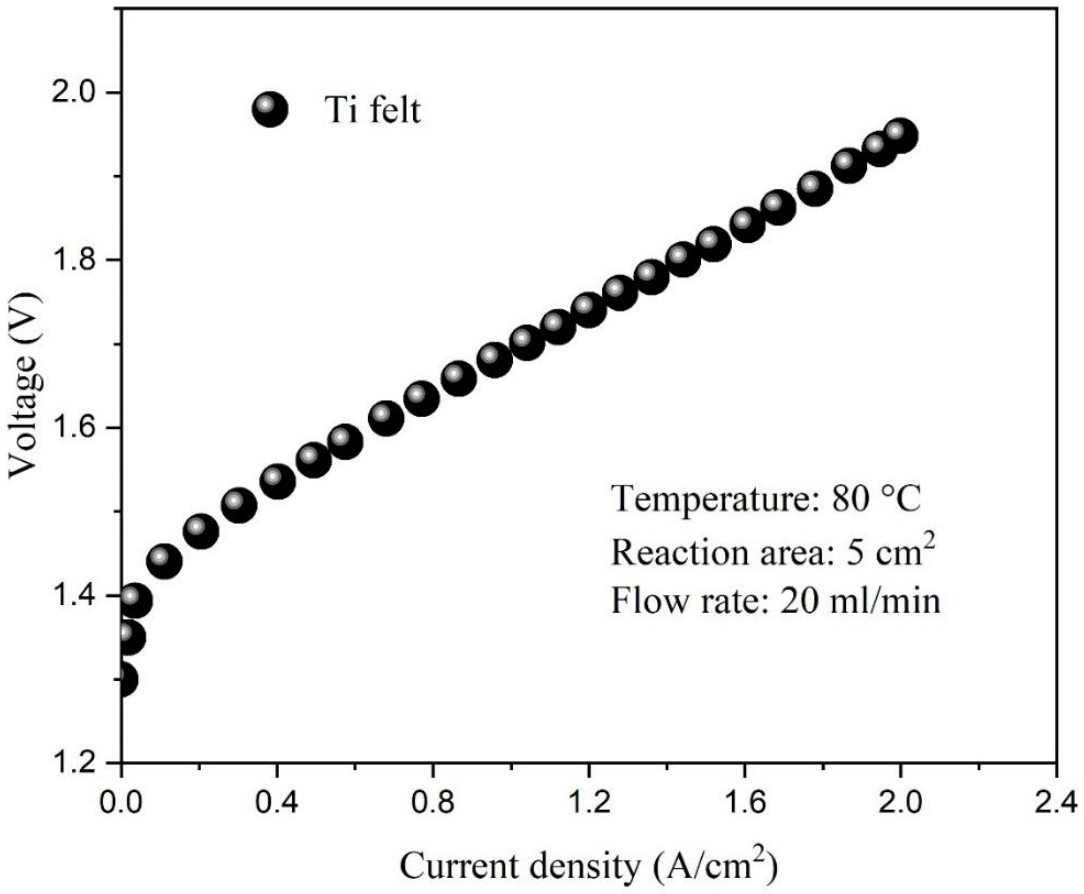

Figure 43. The polarization curve of the PEMEC with Ti felt LGDL.

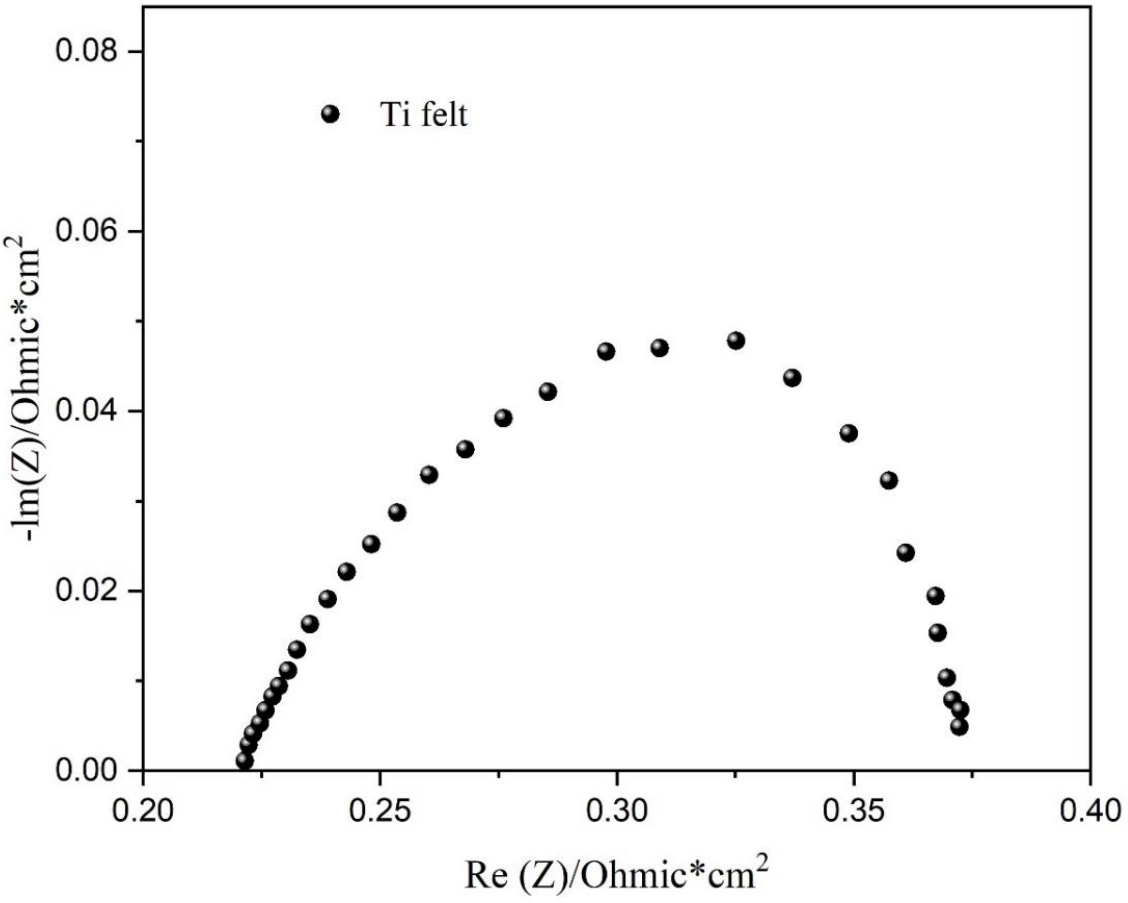

Figure 44. EIS results of the PEMECs with Ti felt LGDL.

Fig. 45 presents images of the two-phase flow phenomena under different conditions: (A1) to (C1) show a flow rate of 10 ml/min, current densities of 0.04 A/cm^2, 0.2 A/cm^2, and 1 A/cm^2. (A2) to (C2) show current densities of 0.2 A/cm^2 and flow rates of 2 ml/min, 10 ml/min, and 20 ml/min. The most common phenomena, according to the visualization results, were bubbles and slug flow. Void fraction in gas liquid flow can be used to define the proportion of gas and liquid rates in the microchannel. Generally, when calculating void fraction, researchers use the time-average value taken over a long period. Void fraction can be expressed as $\propto_g = A_g/(A_g + A_l)$, where A_g is the cross-section area of the gas phase and A_l is the cross-section area of the liquid phase. Current density appeared to have a significant influence on slug flow formation. At low current density, the gas generation rate was low, Q_l was dominant over Q_g, and only bubbly flow could be captured in the microchannel. As Fig. 45 shows, more bubbles were generated in pores with an increase of current density. Smaller bubbles were more likely to merge to form a single large bubble, and the slug flow were more easily to form (see C1). Additionally, two-phase flow can change under different flow rates. The slug flow phenomena can also be captured at a very low flow rate (see A2), due to the slow movement of gas bubbles: bubbles will then gradually accumulate and form a slug flow. In general, the change in shape, size, and flow patterns of gas bubbles that occur alongside an increase in current density for any single channel can be described thus: at very low current density (0.04 A/cm^2), numerous small, spherically shaped gas bubbles emerge from various locations on the Ti felt surface and the channel edge. The gas bubbles become detached when the dynamic pressure of the

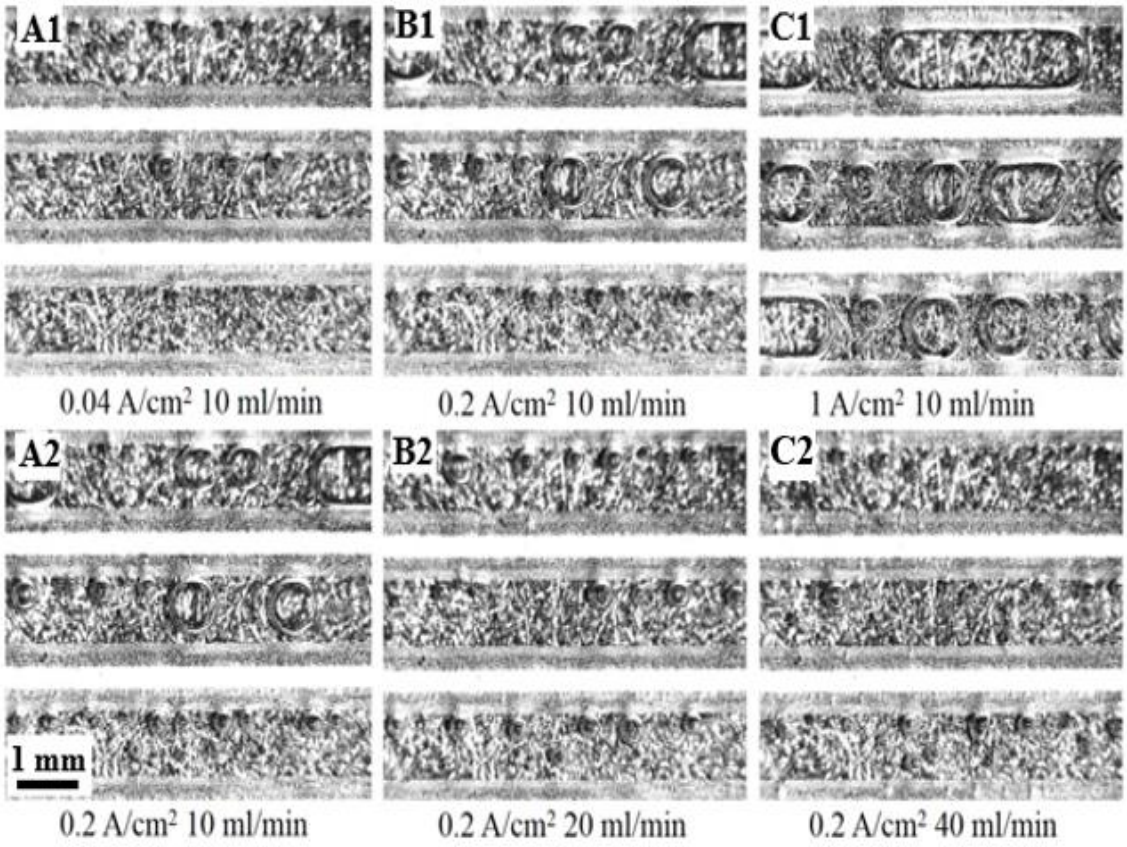

Figure 45. Comparison between the bubble evolution phenomena in the channel-scale, (A1) to (C1) illustrate a flow rate of 10 ml/min, and current densities of 0.04, 0.2, and 1 A/cm^2. (A2) to (C2) illustrate a current density of 0.2 A/cm^2, and flow rates of 10, 20 and 40 ml/min.

flowing water exceeds the surface adhesion. As the current density increases, more gas is produced. As the bubbles depart and coalesce with newly formed bubbles further along the channel, transition to the slug flow pattern begins, and frequent bubble coalescence leads to several bubble slugs occupying sections of the microchannel. In two-phase flow (Fig. A2 to C2), flow and bubble dynamics changed significantly alongside an increasing anode water flow rate. The slug flow was able to form more easily at a low flow rate. At the relatively low flow rate of 2ml/min, bubbles needed more time to detach from the surface and flow to the outlet. This can be attributed to the small drag force and large surface tension force; bubbles had sufficient time to merge with one another at very low flow rates. Bubble flow then became dominant alongside an increase in flow rate. Bubbles tended to stay at the edges of channels (particularly the top edge) due to the higher surface tension there, and the fact that the compression force on the edge was more uniform than in the middle, and not graduated. Therefore, since ohmic losses became smaller for active areas near the edge, more bubbles were able to generate at the edge. Buoyancy force may also have led to bubbles moving to the top edge, because the cell was oriented vertically in the experiment.

Fig. 46A to E show a sequence of small-scale oxygen evolution reactions at 0.2 A/cm^2, 10 ml/min, and 80°C. The pore/bubble is shown in the red circle. The gas bubbles nucleated at certain locations under the Ti felt LGDL, and were then held on the catalyst-coated membrane by strong surface tension, until they grew into a larger bubble that was able to detach. Once the bubbles grew to a sufficient size, they detached and moved along the

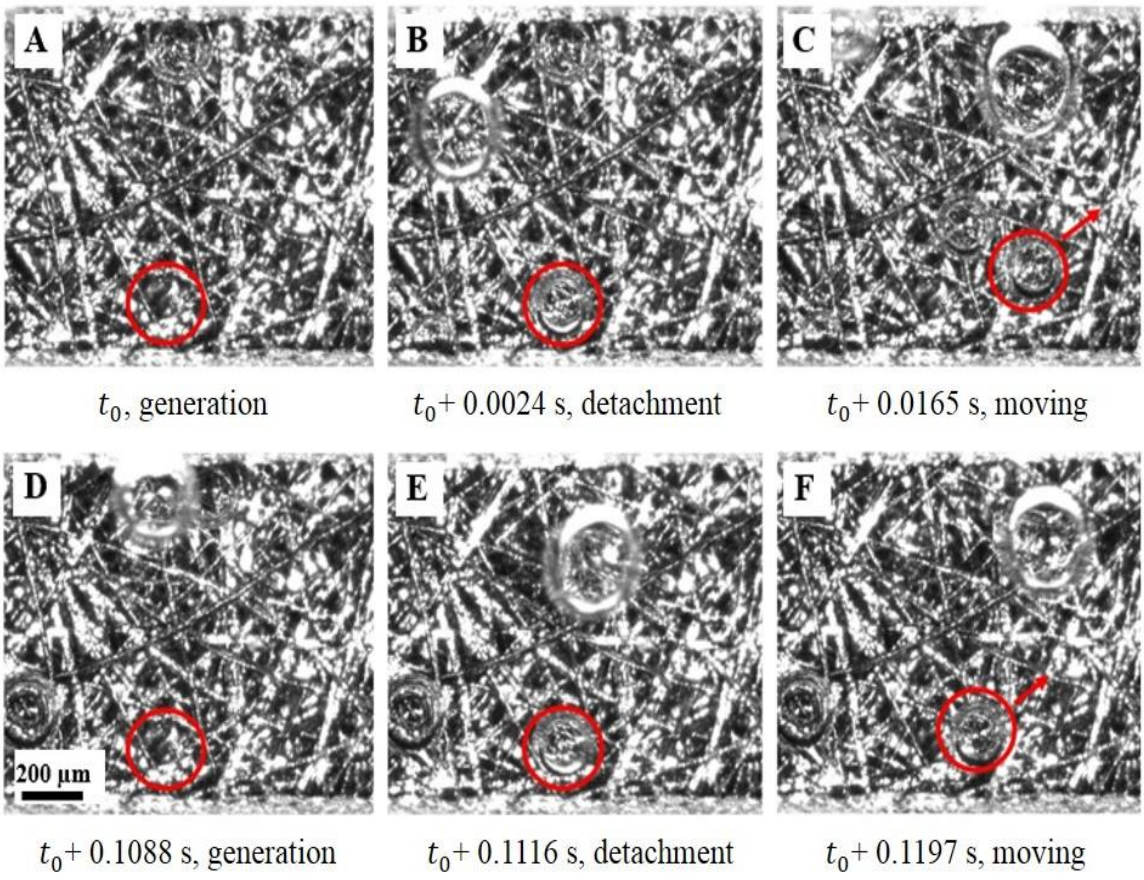

Figure 46. Sequence of photographs showing the small-scale visualization of a single bubble's evolution at 0.2 A/cm^2 and 10 ml/min.

microchannel in the Ti felt. The bubble detachment process is governed by the momentum of liquid flow, the force of buoyancy on the bubble, flow drag force, and surface tension force. Initially (Fig. 46A), there was no bubble in the red circle. Eventually, the bubble began generating and was eventually transported to the top of the Ti felt, and began detaching from the Ti felt at 0.0024 s (Fig. 46B). Finally, the bubble flowed with the incoming DI water to the channel outlet. The direction of the bubble's movement is shown by the red arrow. The drag force and the buoyancy force played a dominant role in the bubble's movement direction. In Fig. 46E, the second bubble has been transported out of the pore and is ready to detach from the surface. The same bubble's movement direction is shown in Fig. 46F. Visual experiment results show that bubbles' growth, detachment, and movement behaviors occurred as regular periodic events.

Fig. 47 demonstrates the impact of the different flow rates on a single bubble's evolution. As shown in this figure, the bubble moved to the surface of the Ti felt at 0.0018 s (Fig. 47B), a shorter time compared to the bubble diameter in Fig. 46B. At 0.1085 s, the second bubble began to generate (Fig. 47D), and was subsequently transported out of the Ti felt at 0.1106 s (Fig. 47E).

The results obtained from the Fig. 47 were carefully checked and compared with those in Fig. 46. The different flow rates indicate a certain impact on detachment time; therefore, an increase in flow rate may to some extent have increased bubble detachment frequency. However, it had almost no impact on bubble detachment diameter, which was roughly 170 μm for each of the two different flow rates. This can be attributed to the surface tension

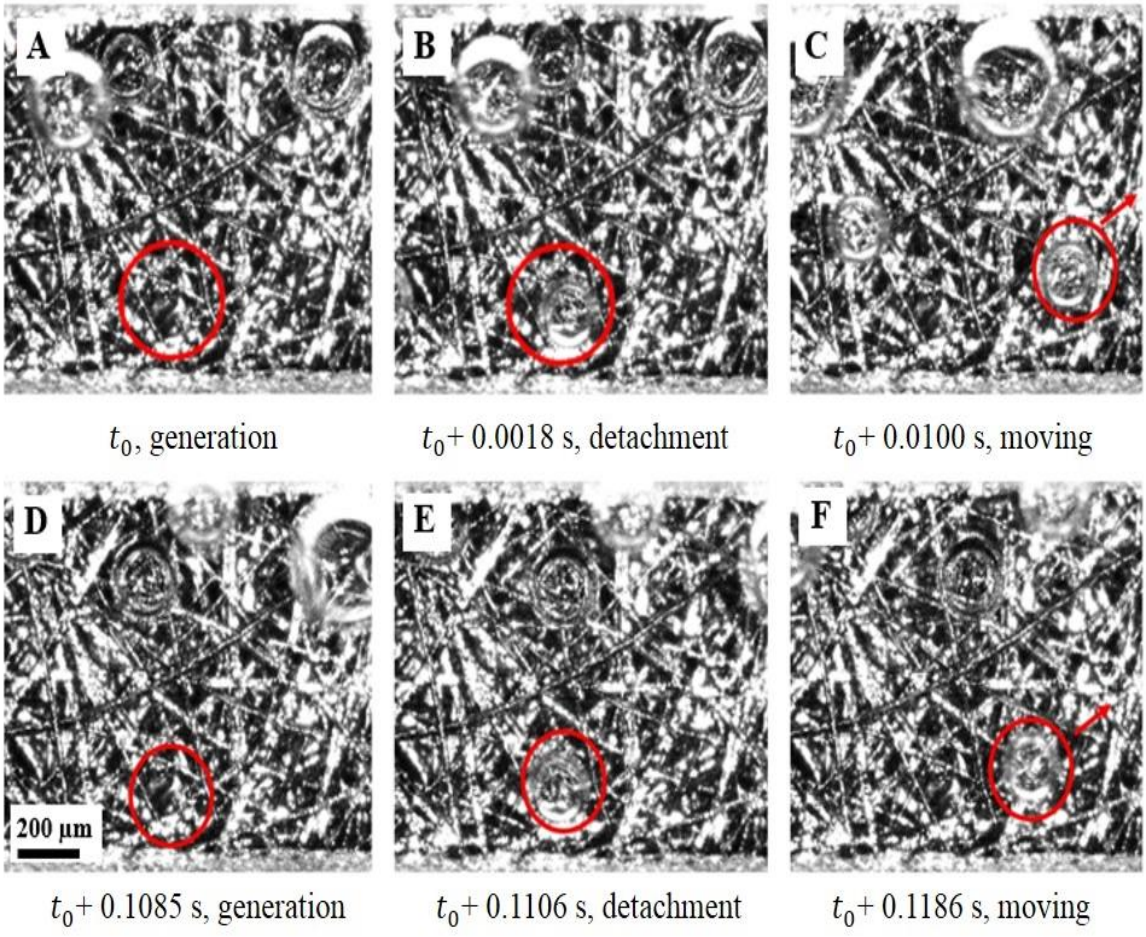

Figure 47. Sequence of photographs showing the small-scale visualization of a single bubble's evolution at 0.2 A/cm^2 and 20 ml/min.

playing a dominant role during the bubble's invasion behavior, which can significantly limit bubble detachment diameter. More importantly, bubble generation and transportation all occurred in the Ti felt. During this process, the flow rate had almost no impact on the entirety of the bubble's behavior inside the Ti felt. The complicated structure of the Ti felt protected the bubble from the impact of different flow rates.

Fig. 48 shows the impact of different current densities on a single bubble's evolution, showing similar bubble evolution and movement behavior in this case. Since the current density increased to 1 A/cm^2, the bubble only needed 0.0015 s to fully transport out of the Ti felt, a much shorter time than in previous results. This was due to the fast bubble-generation rates underneath the Ti felt at a high current density. At a low current density of 0.2 A/cm^2, the electrochemical reaction was relatively slow, and only a few bubbles were able to form. When the current density increased, the electrochemical reaction in the catalyst layer accelerated. The number of bubble nucleation sites and the bubble growth rate both increased as a result. Consequently, bubble detachment frequency also greatly increased alongside an increase in current density.

According to Poiseuille's law, flow decreases with an increase in channel length. A special channel area was selected due to the instability of the flow rate monitored by the flow meter. The instability of the flow rate occurs more frequently especially at small flow rate. As shown in Fig. 49, the research area was located near the inlet of the flow channel, in order to obtain a stable flow rate. Twelve bubble detachment locations were found to be evenly distributed on the entire surface of the LGDL.

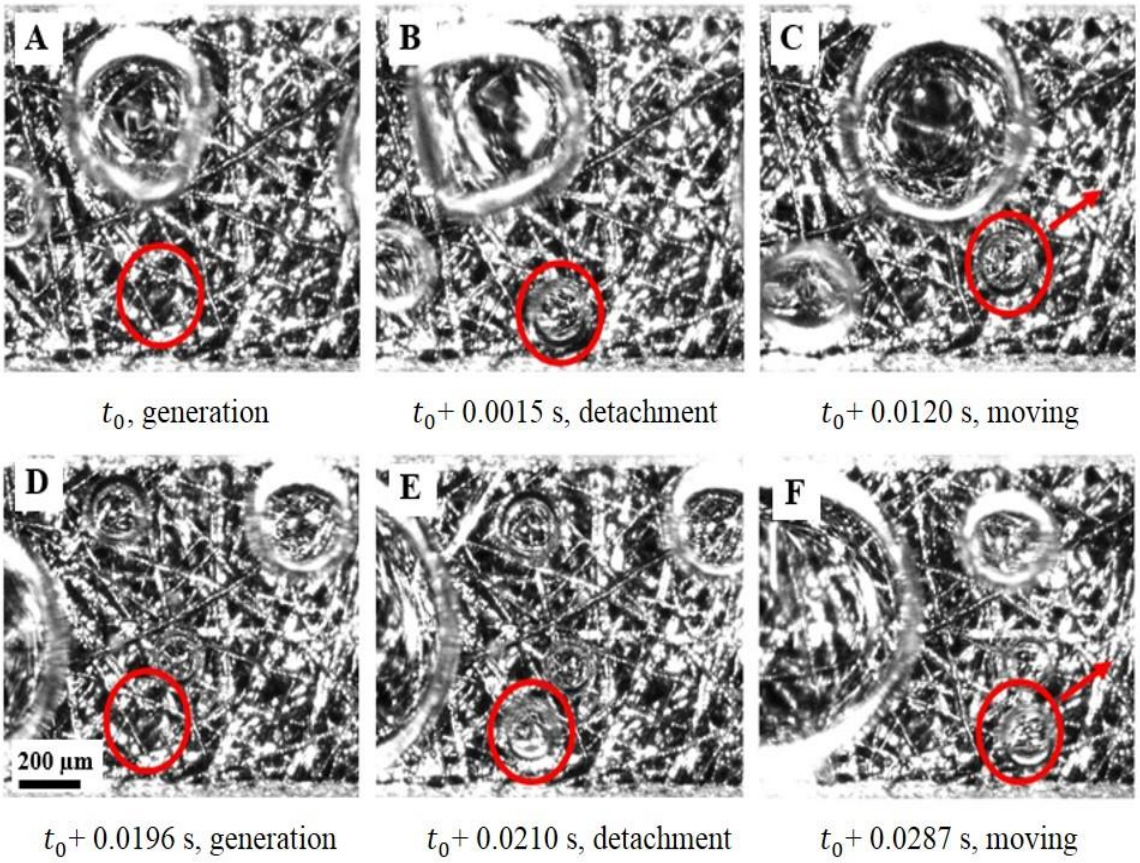

Figure 48. Sequence of photographs showing the small-scale visualization of a single bubble's evolution at 1 A/cm^2 and 10 ml/min.

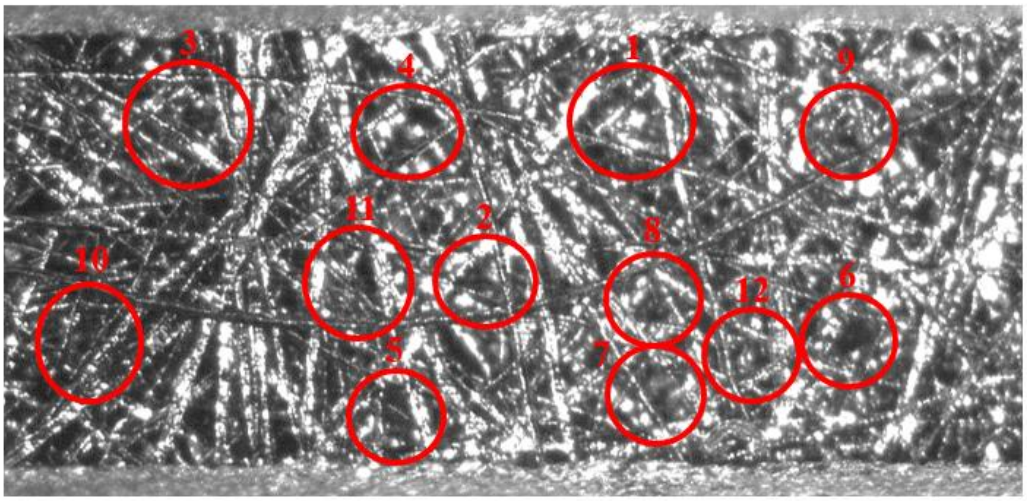

Figure 49. Photograph shows 12 bubble locations.

Fig. 50 shows the bubble detachment diameter at 0.2 A/cm^2 and different flow rates. The bubble was visualized for each flow rate and different locations with different pore size. The pore size was roughly 0.0058 mm^2 for locations eight and nine; 0.0181 mm^2 for locations five, six, and seven; 0.0230 mm^2 for locations one, three, and four. The smallest bubble detachment diameter at 2 mL/min was roughly 178 µm at locations eight and nine; around 210 µm at locations five, six, and seven; around 240 µm at locations one, three, and four. The results indicate that bubble detachment diameter was in good agreement with pore size. Bubbles prefer to detach at a large diameter in a large pore. The flow rate depends on capillary pressure and the surface tension force. A large pore size yields small pressure and small surface tension force to the gas bubble, making it easier to accumulate and

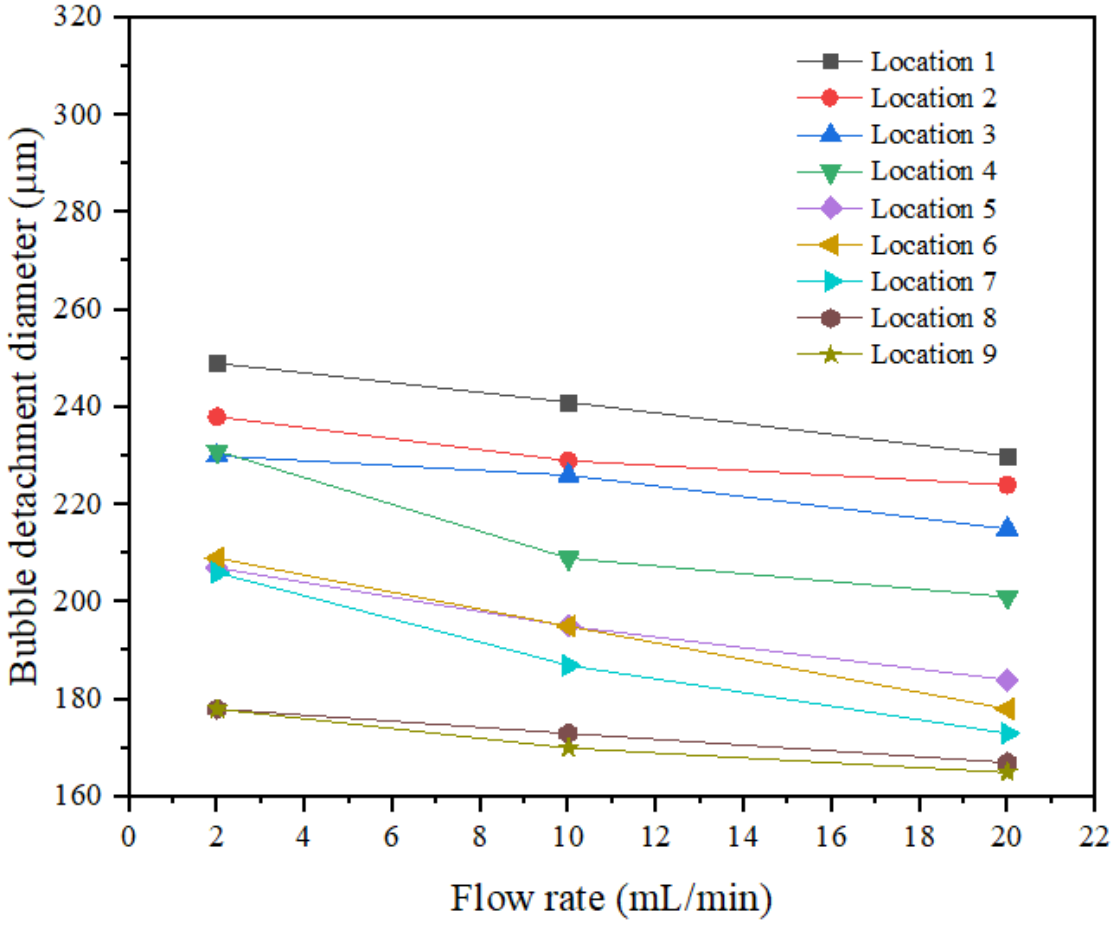

Figure 50. Comparison of the bubble detachment diameter at 0.2 A/cm^2 and different flow rates.

transport from active sites to the top surface. More importantly, the bubble detachment diameter decreased alongside an increase in water flow rate, from 2 to 20 mL/min. The reason for this can be attributed to large flow drag force at large flow rate. A larger drag force makes it easier for the bubble to detach at a smaller bubble diameter. Finally, pore size plays a dominant role in bubble detachment diameter; however, different pore shape has little impact on the bubble detachment diameter. The bubble detachment diameter was very similar for locations five, six, and seven (pore size: 0.0177 mm^2), and for locations eight and nine (pore size: 0.0058 mm^2).

Fig. 51 shows bubble detachment diameter at 10 mL/min and different current densities. The smallest bubble detachment diameter at 0.04 A/cm^2 was roughly 165 µm, at locations eight and nine. The largest bubble detachment diameter was roughly 216 µm, at location two. The results show good agreement with results shown in Fig. 50. The bubble detachment diameter increased alongside pore size. More interestingly, bubble detachment diameter increased with an increase in current density, from 0.04 to 1 A/cm^2. Bubble growth rate increased alongside an increase in current density. More gas will be generated at a large current density.

Fig. 52 shows a schematic of bubble detachment size and their moving direction following detachment from the surface. Buoyancy force is in y direction, and flow drag force is in x direction. Bubble detachment size was in a good agreement with pore size. Bubble detachment size became smaller alongside a small pore size (pore size one, three, and four > six and seven > eight and nine). More importantly, bubble detachment size

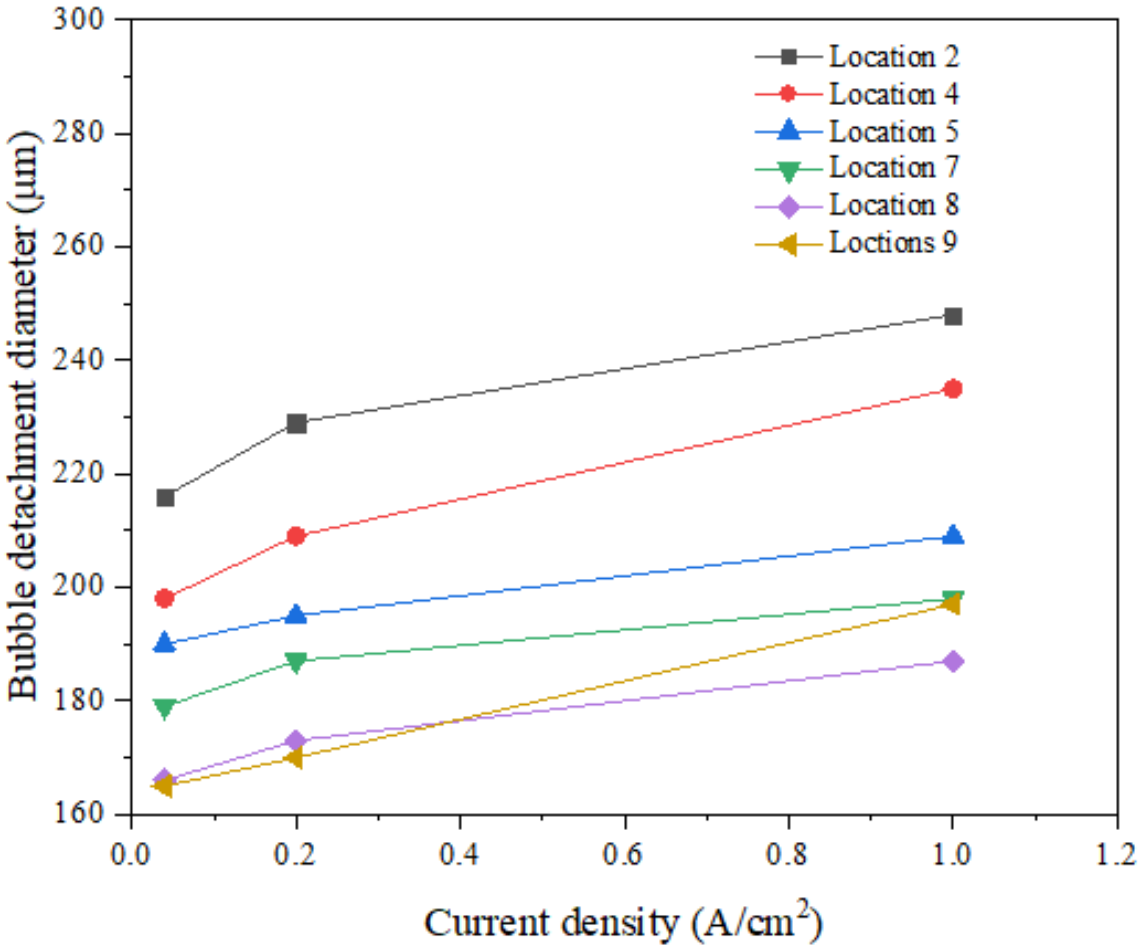

Figure 51. Comparison of the bubble detachment diameter at 10 mL/min and different current densities.

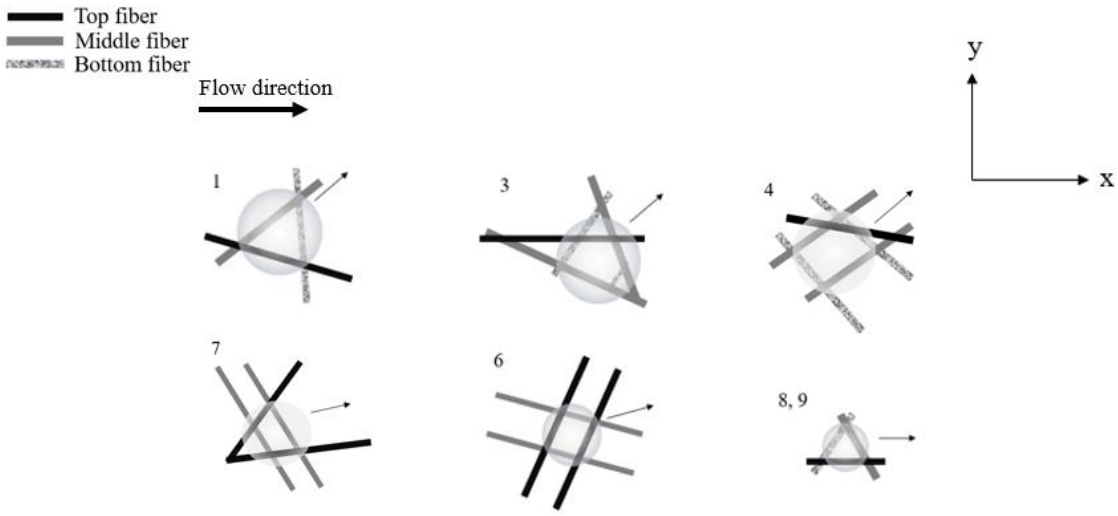

Figure 52. Schematic of bubble detachment size and moving direction in different pores.

showed a significant impact on bubble moving direction after detachment from the surface. For pores one, three, and four, moving direction was toward the top right of the channel (37°). For pores seven and eight, bubble size became smaller, and the moving direction became closer to the center (12°). For pores eight and nine, bubble size was very small, and moving direction was to the east (the same direction as incoming flow). The reason for this can be attributed to a larger bubble buoyancy force alongside an increase in bubble detachment size. The flow drag force played a dominant role when bubble size was small. The role of buoyancy force became significant as bubble size became larger.

6.6 Summary

In this study, rapid and microscale oxygen bubble dynamics and two-phase flow at the anode side of PEMECs were visualized in situ, in a transparent PEMEC, coupled with a high-speed and microscale visualization system. In channel scales, more bubbles were generated at high current density, and slug flow formed more easily at both high current density and low flow rate. In small scales, oxygen gas bubbles were generated under the Ti felt LGDL, and transported inside the Ti felt, until they finally detached from pores. Bubbles then flowed with the incoming water flow to the outlet. Operating current density was able to greatly increase the number of reaction sites, whereas flow rate had no impact on reaction sites. More importantly, both current density and flow rate showed a degree of impact on the bubble's detachment time and detachment diameter. A large current density led to a short detachment time and a slight increase in bubble detachment diameter; a large flow rate led to a short detachment time and a slight decrease in bubble detachment diameter. Finally, bubble moving direction after detaching from the surface was analyzed. Bubble moving direction appeared to be closely related to bubble detachment diameter and flow rate. This research underscores new directions for further study of bubble dynamics and two-phase flow in PEMECs with Ti felt LGDL, thereby allowing for the creation of new and advanced designs and research methods.

References

1. Mo, J., et al. Visualization on rapid and micro-scale dynamics of oxygen bubble evolution in PEMECs. in 2017 IEEE 12th International Conference on Nano/Micro Engineered and Molecular Systems (NEMS). 2017. IEEE.
2. Davis, J., et al., High Speed Video Investigation of Bubble Dynamics and Current Density Distributions in Membraneless Electrolyzers. Journal of The Electrochemical Society, 2019. 166(4): p. F312-F321.
3. Carmo, M., et al., PEM water electrolysis: Innovative approaches towards catalyst separation, recovery and recycling. International Journal of Hydrogen Energy, 2019. 44(7): p. 3450-3455.
4. Kang, Z., et al., Novel Thin/Tunable Gas Diffusion Electrodes with Ultra-Low Catalyst Loading for Hydrogen Evolution Reactions in Proton Exchange Membrane Electrolyzer Cells. Nano Energy, 2018.
5. Yang, H., T. Zhao, and Q. Ye, In situ visualization study of CO2 gas bubble behavior in DMFC anode flow fields. Journal of Power Sources, 2005. 139(1-2): p. 79-90.
6. Mo, J., et al., Discovery of true electrochemical reactions for ultrahigh catalyst mass activity in water splitting. Science advances, 2016. 2(11): p. e1600690.
7. Li, Y., et al., Wettability effects of thin titanium liquid/gas diffusion layers in proton exchange membrane electrolyzer cells. Electrochimica Acta, 2019. 298: p. 704-708.

8. Wang, Q. and W. Yao, Computation and validation of the interphase force models for bubbly flow. International Journal of Heat and Mass Transfer, 2016. 98: p. 799-813.
9. Wang, Y., Modeling of two-phase transport in the diffusion media of polymer electrolyte fuel cells. Journal of Power Sources, 2008. 185(1): p. 261-271.
10. Selamet, O.F., et al., In Situ Two-Phase Flow Investigation of Proton Exchange Membrane (PEM) Electrolyzer by Simultaneous Optical and Neutron Imaging. ECS Transactions, 2011. 41(1): p. 349-362.
11. Majasan, J.O., et al., Two-phase flow behaviour and performance of polymer electrolyte membrane electrolysers: Electrochemical and optical characterisation. International Journal of Hydrogen Energy, 2018.
12. Ito, K., et al., Analysis and visualization of water flow impact on hydrogen production efficiency in solid polymer water electrolyzer under high-pressure condition. International Journal of Hydrogen Energy, 2015. 40(18): p. 5995-6003.
13. Yuan, Z., et al., The whole process, bubble dynamic analysis in two-phase transport of the passive miniature direct methanol fuel cells. Journal of Power Sources, 2019. 416: p. 9-20.
14. Lu, G. and C. Wang, Electrochemical and flow characterization of a direct methanol fuel cell. Journal of Power Sources, 2004. 134(1): p. 33-40.

15. Chandran, P., S. Bakshi, and D. Chatterjee, Study on the characteristics of hydrogen bubble formation and its transport during electrolysis of water. Chemical Engineering Science, 2015. 138: p. 99-109.
16. Fernandez, D., et al., Bubble formation at a gas-evolving microelectrode. Langmuir, 2014. 30(43): p. 13065-13074.
17. Calabriso, A., et al., Assessment of CO2 bubble generation influence on direct methanol fuel cell performance. Energy Procedia, 2015. 75: p. 1996-2002.
18. Li, Y., et al., In-situ investigation of bubble dynamics and two-phase flow in proton exchange membrane electrolyzer cells. International Journal of Hydrogen Energy, 2018.
19. Matsushima, H., et al., Single bubble growth during water electrolysis under microgravity. Electrochemistry Communications, 2009. 11(8): p. 1721-1723.
20. van Limbeek, M.A. and J.R. Seddon, Surface nanobubbles as a function of gas type. Langmuir, 2011. 27(14): p. 8694-8699.
21. Mandin, P., et al., Two-phase electrolysis process: From the bubble to the electrochemical cell properties. Chemical Engineering and Processing: Process Intensification, 2008. 47(11): p. 1926-1932.
22. Arbabi, F., et al., Three-dimensional computational fluid dynamics modelling of oxygen bubble transport in polymer electrolyte membrane electrolyzer porous transport layers. Journal of The Electrochemical Society, 2016. 163(11): p. F3062-F3069.

23. Arbabi, F., et al., Feasibility study of using microfluidic platforms for visualizing bubble flows in electrolyzer gas diffusion layers. Journal of Power Sources, 2014. 258: p. 142-149.

24. Mo, J., S. Steen, and F.-Y. Zhang. High-speed and micro-scale measurements of flow and reaction dynamics for sustainable energy storage. in 13th International Energy Conversion Engineering Conference. 2015.

25. Steen III, S.M., et al., Investigation of titanium liquid/gas diffusion layers in proton exchange membrane electrolyzer cells. International journal of green energy, 2017. 14(2): p. 162-170.

26. Larimi, S.H., et al., The effect of inlet velocity of water on the two-phase flow regime in the porous transport layer of polymer electrolyte membrane electrolyzer. Heat and Mass Transfer, 2018: p. 1-8.

27. Kang, Z., et al., Investigation of thin/well-tunable liquid/gas diffusion layers exhibiting superior multifunctional performance in low-temperature electrolytic water splitting. Energy & Environmental Science, 2017. 10(1): p. 166-175.

28. Zhai, L.-S., et al., Experimental flow pattern map, slippage and time–frequency representation of oil–water two-phase flow in horizontal small diameter pipes. International Journal of Multiphase Flow, 2015. 76: p. 168-186.

CHAPTER VII

CONCLUSIONS AND FUTURE RESEARCH

In this thesis, both experimental and modeling methods were used to study the bubble dynamics and two-phase flow behaviors in PEMECs. A comprehensive literature review about the multiphase flow and electrochemical reaction in electrolyzer was presented in this thesis. A description of the numerical methods and the general requirements for the electrochemical reaction was provided. The findings and results of each chapter can be summarized as follow:

In chapter 2, the rapid and micro-scale oxygen bubble dynamics and two-phase flow at the anode side of PEMECs are visualized in-situ in a specific designed transparent PEMEC coupled with a high-speed and micro-scale visualization system. The similar performance between the transparent and conventional cells provides strong support for the assertion that actual two-phase flow phenomena can be observed in the transparent cell. At channel scales, several two-phase flow phenomena in microchannels, including bubbly, slug and annular flow, have been observed. At pore scales, oxygen gas bubbles are emerged at the rim of the LGDL pores and rapidly grow until detaching from the reaction sites. And then, they coalesce with other micro bubbles or flow with liquid water in the microchannel. It is found that the PEMEC temperature and current density enhance bubble growth rates and increase the number of reaction sites, while its flow rate has limited effects. In addition, a mathematical model has been developed to investigate the bubble growth behavior under different operating conditions, and the modeling results are in good agreement with the

experimental data. This research opens a new pathway for further study of the general working mechanism and two-phase flow in PEMECs, thereby allows the creation of new advanced designs and research methods.

In chapter 3 the hydrophilic titanium TT-LGDLs are treated by a silane monolayer to change their wettability for the first time. The micro-scale and ultra-fast oxygen bubble dynamics are in-situ visualized in a novel designed transparent PEMEC with a HMVS. The results show that the oxygen bubble detachment diameter and frequency of the hydrophobic TT-LGDLs are much larger than ones with the hydrophilic TT-LGDLs, and the bubble size in the channel scale with the hydrophobic TT-LGDLs is much larger than the one with the hydrophilic TT-LGDLs as well. The PEMEC performance with the hydrophobic and hydrophilic TT-LGDLs are very close. The advantages of the TT-LGDLs, such as planar surface, straight-through pores, and small thickness result in very limited difference of the transport losses between the hydrophobic and hydrophilic TT-LGDLs. The increase of the transport loss due to these reasons is very small compared with the total loss in the PEMEC, especially under 2.0 A/cm2. We expect that the performance of the hydrophobic TT-LGDLs will be degraded under much higher current densities, due to the large bubble detachment which may cause additional two-phase transport losses in a PEMEC.

In chapter 4, a specific PEMEC was developed to visualize hydrogen gas bubble generation, and temperature variance in the cathode channels. It was observed that the temperature field in the entire channel was not uniform; some pores had a relatively higher

temperature than the others. The temperature gradually increased until it reached the equilibrium state. During this process, the areas with the highest temperature in the channels were consistent with the highest hydrogen bubble generation rate areas, which means that heat release occurred due to an active electrochemical reaction. A series of pore scale temperature distribution change phenomena have also been visualized; the results show that the temperature change phenomena vary in different pores. The reason can be attributed to the electrochemical reaction occurred in different pores. More importantly, the temperature increase areas are consistent with the bubble generation areas, and this phenomenon has been found to be replicable in other pores. Finally, investigations on the LGDL surface shown that the temperature on the LGDL also increased rapidly with respect to time. The reason can be attributed to the ohmic loss and heat transferred from the CCM. These findings could help better understand the correlation between the cathode side electrochemical reaction and heat generation, in order to provide a basis for future research, both in terms of modeling and experiment.

In chapter 5, a comprehensively in-situ study was conducted to delineate the mechanisms of microbubble dynamics in a single-channel water electrolyzer with the help of the state-of-the-art characterization system. A transparent single-channel electrolyzer was developed to visualize oxygen and hydrogen bubble behavior in the microchannel. For the first time, the oxygen and hydrogen bubble behaviors were simultaneously presented and investigated in electrolyzer. The two-phase flow phenomena have been visualized and investigated at different working conditions. In addition, both current density and flow

velocity have shown clear effects on the reaction site and bubble growth rate. Bubble detachment diameter was increased with an increase of the current density, and decreased with an increase of the flow velocity. More importantly, a theoretical two-dimension model for bubble dynamics has been built to investigate the bubble detachment diameter under different operating conditions. The predictions of this model agreed with the experimental results. The results could help to better understand the bubble evolution mechanism, to evaluate the electrochemical reaction involved during water electrolysis.

In chapter 6, rapid and microscale oxygen bubble dynamics and two-phase flow at the anode side of PEMECs were visualized in situ, in a transparent PEMEC, coupled with a high-speed and microscale visualization system. In channel scales, more bubbles were generated at high current density, and slug flow formed more easily at both high current density and low flow rate. In small scales, oxygen gas bubbles were generated under the Ti felt LGDL, and transported inside the Ti felt, until they finally detached from pores. Bubbles then flowed with the incoming water flow to the outlet. Operating current density was able to greatly increase the number of reaction sites, whereas flow rate had no impact on reaction sites. More importantly, both current density and flow rate showed a degree of impact on the bubble's detachment time and detachment diameter. A large current density led to a short detachment time and a slight increase in bubble detachment diameter; a large flow rate led to a short detachment time and a slight decrease in bubble detachment diameter. Finally, bubble moving direction after detaching from the surface was analyzed. Bubble moving direction appeared to be closely related to bubble detachment diameter and

flow rate. This research underscores new directions for further study of bubble dynamics and two-phase flow in PEMECs with Ti felt LGDL, thereby allowing for the creation of new and advanced designs and research methods.In the future, more research on the bubble dynamics at different working conditions can be done to find the best working condition for enhancing operating performance. According to the previous visualization results, bubbles are also generated under the channel, and the bubble number under the channel can't be neglected. It will be benefit if a method can be introduced to visualize and investigate the bubbles evolution phenomena under the channel. During the operation, the water droplet will gradually be accumulated on the cathode side catalyst layer. A correlation between the electrochemical reaction and the water droplet accumulation can be built to better understand the electrochemical reaction occurred on the cathode side of PEMECs. Finally, a comparison between the performance and the two-phase flow phenomena in PEMECs with different LGDL can be conducted for understanding the bubble dynamics in different pore structures. In this way, more advanced PEMECs structure can be developed to greatly reduce the activation, mass transport and ohmic losses, so as to decide the best working condition for both hydrogen evolution reaction and oxygen evolution reaction with minimal loss.

VITA

Yifan Li was born in Shanxi, Xi'an, China. He studied in Shanghai Ocean University from 2009 to 2013 for the B.S. degree in major of Thermal and Power Engineering. Then he went to graduate school at the Northeastern University in Boston, MA, US. He received his M.S. in Mechanical Engineering in 2016. He began to study at the University of Tennessee, Knoxville (UTK) in Mechanical Engineering for Ph.D. degree from 2017.